

STRUCTURAL DESIGN AND EVALUATION OF AN ADAPTIVE CAMBER  
WING

A THESIS SUBMITTED TO  
THE GRADUATE SCHOOL OF NATURAL AND APPLIED SCIENCES  
OF  
MIDDLE EAST TECHNICAL UNIVERSITY

BY

EVREN SAKARYA

IN PARTIAL FULFILLMENT OF THE REQUIREMENTS  
FOR  
THE DEGREE OF MASTER OF SCIENCE  
IN  
AEROSPACE ENGINEERING

FEBRUARY 2010

Approval of the thesis:

**STRUCTURAL DESIGN AND EVALUATION OF AN ADAPTIVE  
CAMBER WING**

submitted by **EVREN SAKARYA** in partial fulfillment of the requirements for  
the degree of **Master of Science in Aerospace Engineering Department,**  
**Middle East Technical University** by,

Prof. Dr. Canan Özgen \_\_\_\_\_  
Dean, Graduate School of **Natural and Applied Sciences**

Prof. Dr. Ozan Tekinalp \_\_\_\_\_  
Head of Department, **Aerospace Engineering**

Assist. Prof. Dr. Güçlü Seber \_\_\_\_\_  
Supervisor, **Aerospace Engineering Dept., METU**

**Examining Committee Members:**

Prof. Dr. Yavuz Yaman \_\_\_\_\_  
Aerospace Engineering Dept., METU

Assist. Prof. Dr. Güçlü Seber \_\_\_\_\_  
Aerospace Engineering Dept., METU

Assist. Prof. Dr. Melin Şahin \_\_\_\_\_  
Aerospace Engineering Dept., METU

Prof. Dr. Serkan Özgen \_\_\_\_\_  
Aerospace Engineering Dept., METU

Assist. Prof. Dr. Ender Ciğeroğlu \_\_\_\_\_  
Mechanical Engineering Dept., METU

**Date:** 01.02.2010

**I hereby declare that all information in this document has been obtained and presented in accordance with academic rules and ethical conduct. I also declare that, as required by these rules and conduct, I have fully cited and referenced all material and results that are not original to this work.**

Name, Last name : Evren Sakarya

Signature :

## **ABSTRACT**

### **STRUCTURAL DESIGN AND EVALUATION OF AN ADAPTIVE CAMBER WING**

Sakarya, Evren

M.S., Department of Aerospace Engineering

Supervisor: Assist. Prof. Dr. Güçlü Seber

February 2010, 105 pages

This study presents a camber morphing concept as an alternative to existing plain flap or aileron type hinged control surfaces used in wings. Structural aspects of the concept are investigated with static nonlinear finite element analyses by using MSC Nastran. In order to assess the aerodynamic characteristics; CFD based 2D solutions are obtained using ANSYS Fluent. The camber morphing concept is applied to the full scale hingeless control surface and implemented in the adaptive camber wing. Hingeless control surfaces and adaptive camber wing are manufactured and changes made in manufacture stages are incorporated into finite element models. Finite element analyses of the wing are conducted with static and dynamic loading and comparison with experimental dynamic analyses are performed.

Keywords: morphing wing, adaptive camber, mission adaptive wing, nonlinear structural analysis.

## ÖZ

### UYARLANABİLİR KAMBURA SAHİP BİR KANADIN YAPISAL TASARIMI VE DEĞERLENDİRİLMESİ

Sakarya, Evren

Yüksek Lisans, Havacılık ve Uzay Mühendisliği Bölümü

Tez Yöneticisi: Y. Doç. Dr. Güçlü Seber

Şubat 2010, 105 sayfa

Bu çalışmada, uçaklarda kullanılan flap ve kanatçık gibi menteşeli kontrol yüzeylerine alternatif olabilecek kambur değiştirme konsepti sunulmaktadır. Yapısal özellikler statik doğrusal olmayan sonlu elemanlar analizler ile MSC Nastran kullanılarak aracılığıyla çözümlenmiştir. Aerodinamik özelliklerin tanımlanabilmesi için, 2-Boyutlu hesaplamalı akışkanlar mekaniği çözümleri ANSYS Fluent kullanılarak yapılmıştır. Kambur değiştirme konsepti, menteşesiz kontrol yüzeyini oluşturmak için kullanılmış ve uyarlanabilir kambura sahip kanada uygulanmıştır. Menteşesiz kontrol yüzeyleri ve uyarlanabilir kambura sahip kanat üretilmiş ve üretim safhasında gerçekleşen değişiklikler sonlu elemanlar modellerine aktarılmıştır. Kanat için statik ve dinamik sonlu eleman analizleri yapılmış ve deneysel dinamik analizler ile karşılaştırılmıştır.

Anahtar Kelimeler: şekil değiştirebilen kanat, uyarlanabilir kambur, göreve uyumlu kanat, doğrusal olmayan yapısal analiz.

*To my loved ones.*

## ACKNOWLEDGEMENTS

I would like to express my sincere gratitude to my supervisor Assist. Prof. Dr. Güçlü Seber for guiding me, sharing his knowledge and experience throughout the study. Without his enthusiasm I would not be able to complete this thesis.

I would also like to thank Prof. Dr. Yavuz Yaman for his leadership, guidance and criticism through the thesis study and project work. I want to emphasize my special thanks to Assist. Prof. Dr. Melin Şahin and Prof. Dr. Serkan Özgen for their continuous support and helpful discussions.

I want to thank my colleagues Levent Ünlüsoy and Erdoğan Tolga İnsuyu for their assistance and collaboration in the study.

Last, but not least, I would like to express my deepest thanks to my parents and my love Arzu Kayır for their endless support.

This thesis work is supported by Turkish Scientific and Technological Research Council through the project ‘TÜBİTAK/107M103, Aeroservoelastic Analysis of the Effects of Camber and Twist on Tactical Unmanned Aerial Vehicle Mission-Adaptive Wings’.

## TABLE OF CONTENTS

ABSTRACT .....	iv
ÖZ .....	v
ACKNOWLEDGEMENTS .....	vii
TABLE OF CONTENTS .....	viii
LIST OF TABLES .....	x
LIST OF FIGURES.....	xi
LIST OF SYMBOLS .....	xvii
CHAPTERS	
1 INTRODUCTION.....	1
1.1 Background to the Study .....	1
1.2 Scope and Limitations of the Study.....	1
1.3 Content of the Study .....	2
2 LITERATURE SURVEY .....	3
2.1 Introduction .....	3
2.2 Mission Adaptive Wing.....	3
2.3 Morphing Wing .....	4
3 DEVELOPMENT OF THE HINGELESS CONTROL SURFACE CONCEPT. 6	
3.1 Introduction .....	6
3.2 Adaptive Camber Wing.....	7
3.3 Structural Modeling and Solution Methodology.....	8

3.4	Structural Modeling of Camber Morphing: Initial Model.....	14
3.5	Structural Modeling of Camber Morphing: Detailed Model.....	20
3.6	Aerodynamic Modeling and CFD Based Solution Methodology .....	29
3.7	Assessment of the Concept.....	32
3.7.1	Actuation Force Placement .....	33
3.7.2	Track & Cutout Rib Length .....	34
3.7.3	Support Web Placement.....	40
3.7.4	Aerodynamics of the Representative Section.....	48
3.8	Coupled Analysis.....	51
3.9	Conclusions .....	58
4	STRUCTURAL DESIGN & ANALYSIS OF THE ADAPTIVE CAMBER WING.....	60
4.1	Introduction .....	60
4.2	Theoretical Modeling of the Full Scale Hingeless Control Surface.....	60
4.3	Manufacture of the Full Scale Hingeless Control Surface .....	72
4.4	Analysis of the Adaptive Camber Wing.....	78
4.5	Modal Analysis of Adaptive Camber Wing .....	85
4.5.1	Finite Element Method Results.....	85
4.5.2	Experimental Results .....	90
4.6	Conclusions .....	98
5	CONCLUSION .....	99
5.1	General Conclusions.....	99
5.2	Recommendations for Future Work .....	100
	REFERENCES.....	102

## LIST OF TABLES

### TABLES

Table 3.1: Wing Geometric Parameters .....	8
Table 3.2: Element Types and Numbers for Detailed Model .....	26
Table 3.3: Materials and Thicknesses Related With Structural Members .....	27
Table 3.4: Physical and Mechanical Properties of Aluminum 2024-T3 .....	28
Table 3.5: Physical and Mechanical Properties of 7781 E-Glass Fabric with Araldite LY5052 Resin .....	28
Table 3.6: Aerodynamic Mesh Properties.....	29
Table 3.7: Standard Sea Level Atmospheric Properties.....	32
Table 3.8: Single Support Web Case ( $s = 15 \text{ cm}$ ).....	42
Table 3.9: Double Support Web Case ( $s_1 = 14 \text{ cm}$ and $s_2 = 17 \text{ cm}$ ) .....	46
Table 4.1: Element Types and Numbers for Hingeless Control Surface Finite Element Model.....	61
Table 4.2: Element Types and Numbers Used in the Adaptive Camber Wing Finite Element Model.....	79
Table 4.3: Element Types and Numbers Used in Adaptive Camber Wing Modal Analysis Model .....	87
Table 4.4: Natural Modes and Associated Frequencies (Finite Element Analysis) .....	90
Table 4.5: Comparison of Experimental Mode Shape Frequencies for Global Modes of the Adaptive Camber Wing.....	97
Table 4.6: Comparison of Experimental Mode Shape Frequencies with Finite Element Analysis for Global Modes of the Adaptive Camber Wing.....	97

## LIST OF FIGURES

### FIGURES

Figure 3.1: Adaptive Camber Wing (with the Hingeless Control Surfaces).....	7
Figure 3.2: Primary and Secondary Structures and Spar Locations.....	9
Figure 3.3: Zoomed View of the Semi-open Trailing Edge.....	10
Figure 3.4: Shell Contact Definition [34].....	11
Figure 3.5: Follower Force Example [34].....	12
Figure 3.6: MSC <sup>®</sup> Nastran Implicit Nonlinear Solution Flow Diagram [34] .....	14
Figure 3.7: Initial Concept Development Model .....	15
Figure 3.8: Closed Section Displacement Result [m] .....	16
Figure 3.9: Closed Section Stress Result [Pa].....	17
Figure 3.10: Initial Concept Model with Support Elements .....	18
Figure 3.11: Initial Concept Model Example Displacement [m].....	19
Figure 3.12: Initial Model Example Displacements.....	20
Figure 3.13: Hingeless Control Surface Prototype.....	21
Figure 3.14: Hingeless Control Surface Prototype Camber Increase.....	22
Figure 3.15: Hingeless Control Surface Prototype Camber Decrease .....	22
Figure 3.16: Hingeless Control Surface Representative Section .....	23
Figure 3.17: Guide-Slide Assembly .....	24
Figure 3.18: Detailed Model Finite Element Mesh.....	25
Figure 3.19: Hingeless Control Surface Detailed Model .....	26
Figure 3.20: Solution Domain for Aerodynamic Analysis .....	30
Figure 3.21: C-Grid Aerodynamic Mesh .....	30
Figure 3.22: Close-up View of Aerodynamic Mesh Around Normal Section.....	31
Figure 3.23: Close-up View of Aerodynamic Mesh Around Morphed Section ...	31
Figure 3.24: Actuation Force Application Point .....	33

Figure 3.25: Trailing Edge Deflection $\Delta_{TE}$ vs. Force Application Point as measured wrt Lower Skin for Different Track Sizes .....	34
Figure 3.26: Trailing Edge Deflection of Different Track Size Models for Constant Force Applied in Positive Chordwise Direction .....	35
Figure 3.27: Trailing Edge Deflection of Different Track Size Models for Constant Force Applied in Negative Chordwise Direction.....	36
Figure 3.28: Cauchy Stress Distribution for 6cm Track Size with 10N Actuation Force [Pa] .....	37
Figure 3.29: Cauchy Stress Distribution for 10cm Track Size with 10N Actuation Force [Pa] .....	37
Figure 3.30: Actuation Force (F) vs. Trailing Edge Deflection ( $\Delta_{TE}$ ) for Track Sizes of 6 to 14 cm .....	38
Figure 3.31: Hingeless Control Surface Displacement for Positive Camber with 10N Actuation Force [m] .....	39
Figure 3.32: Hingeless Control Surface Displacement for Negative Camber with 10N Actuation Force [m] .....	39
Figure 3.33: Effects of Nonlinearity on Actuation Force.....	40
Figure 3.34: Support Web Location and Slanting Angle Definitions.....	41
Figure 3.35: Percentage Reduction in Trailing Edge Deflection for Different Support Web Slanting Angles.....	43
Figure 3.36: $\theta = 14.72^\circ$ Single Support Web Displacement with 10N Actuation Force in Positive Chordwise Direction [m] (Maximum Displacement = 1.96 cm) .....	44
Figure 3.37: $\theta = -8.2^\circ$ Single Support Web Displacement with 10N Actuation Force in Positive Chordwise Direction [m] (Maximum Displacement = 2.40 cm) .....	44
Figure 3.38: $\theta = 14.72^\circ$ Single Support Web Displacement with 10N Actuation Force in Negative Chordwise Direction [m] (Maximum Displacement = 2.61 cm) .....	45

Figure 3.39: $\theta = -8.2^\circ$ Single Support Web Displacement with 10N Actuation Force in Negative Chordwise Direction [m] (Maximum Displacement = 2.41 cm) .....	45
Figure 3.40: Cauchy Stress Distribution of Model with Single Support Web (10N Positive Chordwise Actuation) [Pa].....	47
Figure 3.41: Cauchy Stress Distribution of Model with Two Support Webs (10N Positive Chordwise Actuation) [Pa].....	47
Figure 3.42: Displacement of Model with Two Support Webs (10N Positive Chordwise Actuation) [m].....	48
Figure 3.43: Lift Coefficient ( $C_l$ ) vs. Trailing Edge Deflection ( $\Delta_{TE}$ ) .....	49
Figure 3.44: Pitching Moment Coefficient ( $C_m$ ) vs. Trailing Edge Deflection ( $\Delta_{TE}$ ) .....	50
Figure 3.45: Lift vs. Drag Coefficients .....	50
Figure 3.46: Static Pressure Distribution for $\Delta_{TE} = -2.41$ cm .....	51
Figure 3.47: Static Pressure Distribution for $\Delta_{TE} = -0.977$ cm .....	52
Figure 3.48: Static Pressure Distribution for $\Delta_{TE} = 0$ (Unmorphed Section)....	52
Figure 3.49: Static Pressure Distribution for $\Delta_{TE} = 0.81$ cm .....	53
Figure 3.50: Static Pressure Distribution for $\Delta_{TE} = 2.4$ cm .....	53
Figure 3.51: Cauchy Stress Distribution for $\Delta_{TE} = -2.41$ cm [Pa] .....	55
Figure 3.52: Cauchy Stress Distribution for $\Delta_{TE} = 0$ [Pa].....	55
Figure 3.53: Cauchy Stress Distribution for $\Delta_{TE} = 2.4$ cm [Pa].....	56
Figure 3.54: Superposed Views of the Hingeless Control Surface for Different Trailing Edge Deflections .....	56
Figure 3.55: Variation of the Actuation Force with Trailing Edge Deflection ( $\Delta_{TE}$ ) .....	57
Figure 3.56: Variation of the Aerodynamic Moment ( $H$ ) with Trailing Edge Deflection ( $\Delta_{TE}$ ).....	58
Figure 4.1: Finite Element Model of Hingeless Control Surface.....	62

Figure 4.2: Finite Element Model of Hingeless Control Surface (Upper Skin & Rear Spar Removed) .....	62
Figure 4.3: Displacement of the Hingeless Control Surface with 20N Constant Actuation in Positive Chordwise Direction [m].....	64
Figure 4.4: Displacement of the Hingeless Control Surface with 50N Constant Actuation in Positive Chordwise Direction [m].....	64
Figure 4.5: Cauchy Stress Distribution for 50N Constant Actuation in Positive Chordwise Direction .....	65
Figure 4.6: Cauchy Stress Distribution for 50N Constant Actuation in Negative Chordwise Direction .....	66
Figure 4.7: Displacement of the Hingeless Control Surface with 50N & 20N Positive Chordwise Actuation [m].....	67
Figure 4.8: Displacement of the Hingeless Control Surface with 50N & 20N Positive Chordwise Actuation [m] (From Trailing Edge).....	67
Figure 4.9: Displacement of the Hingeless Control Surface with 50N Positive Chordwise & 50N Negative Chordwise Actuation [m].....	68
Figure 4.10: Cauchy Stress Distribution of the Hingeless Control Surface with 50N Positive Chordwise & 50N Negative Chordwise Actuation [Pa].....	69
Figure 4.11: Finite Element Model of the Hingeless Control Surface with Control Spar (Upper Skin & Rear Spar Removed) .....	70
Figure 4.12: Displacement of the Hingeless Control Surface with 50N Positive Chordwise Actuation [m] (Model with Control Spar) .....	71
Figure 4.13: Displacement of the Hingeless Control Surface with 50N Negative Chordwise Actuation [m] (Model with Control Spar) .....	71
Figure 4.14: Cauchy Stress Distribution of the Hingeless Control Surface with 50N Positive Chordwise Actuation [Pa] (Model with Control Spar).....	72
Figure 4.15: Track of the Guide-Slide Assembly .....	73
Figure 4.16: Cutout Rib of the Guide-Slide Assembly .....	73
Figure 4.17: Guide-Slide Assembly Attached to Lower Skin, Push Rod Connected to Cutout Rib .....	74

Figure 4.18: Servo Connection .....	75
Figure 4.19: Hingeless Control Surface with Constant Positive Chordwise Actuation.....	76
Figure 4.20: Hingeless Control Surface with Constant Negative Chordwise Actuation.....	76
Figure 4.21: Hingeless Control Surface with Twisting Actuation.....	77
Figure 4.22: Hingeless Control Surface with Twisting Actuation (From Trailing Edge).....	77
Figure 4.23: Finite Element Model of the Hingeless Control Surface (Upper Skin Removed) .....	78
Figure 4.24: Finite Element Model of the Adaptive Camber Wing.....	79
Figure 4.25: Displacement of the Adaptive Camber Wing, Only Outer Hingeless Control Surface Actuated in Positive Chordwise Direction [m].....	80
Figure 4.26: Displacement of the Adaptive Camber Wing, Only Outer Hingeless Control Surface Actuated in Negative Chordwise Direction [m] .....	81
Figure 4.27: Cauchy Stress Distribution of the Adaptive Camber Wing, Only Outer Hingeless Control Surface Actuated in Positive Chordwise Direction [Pa].....	81
Figure 4.28: Displacement of the Adaptive Camber Wing, All Hingeless Control Surfaces Actuated in Positive Chordwise Direction [m] .....	82
Figure 4.29: Displacement of the Adaptive Camber Wing, Inner Hingeless Control Surface Actuated in Negative Chordwise Direction, Outer Hingeless Control Surface Actuated in Positive Chordwise Direction [m].....	83
Figure 4.30: Displacement of the Outer Hingeless Control Surface Actuated with Twisting Actuation of 20N & 50N [m].....	84
Figure 4.31: Cauchy Stress Distribution of the Outer Hingeless Control Surface Actuated with Twisting Actuation of 20N & 50N [Pa] .....	84
Figure 4.32: Geometry of the Adaptive Camber Wing.....	86
Figure 4.33: Detailed Finite Element Model of the Adaptive Camber Wing .....	86

Figure 4.34: Mode Shape of the Adaptive Camber Wing at 13.52 Hz (First Out-of-plane Bending Natural Frequency, Hingeless Control Surfaces and Tip Fairing Shown) .....	88
Figure 4.35: Mode Shape of the Adaptive Camber Wing at 13.52 Hz (First Out-of-plane Bending Natural Frequency).....	88
Figure 4.36: Mode Shape of the Adaptive Camber Wing at 46.30 Hz (First Torsional Natural Frequency) .....	89
Figure 4.37: Mode Shape of the Adaptive Camber Wing at 87.69 Hz (Second Out-of-plane Bending Natural Frequency).....	89
Figure 4.38: Analysis Equipment Used in the Experimental Modal Analysis.....	91
Figure 4.39: Adaptive Camber Wing Attached to Fixture, Modal Shaker and Accelerometers Attached to the Wing .....	91
Figure 4.40: Experimental Grid of the Wing Torque-Box.....	91
Figure 4.41: Frequency Response Function Between Accelerometer in Node 54 and White Noise Excitation from Node 5 .....	92
Figure 4.42: Frequency Response Function Between Accelerometer in Node 54 and Sine Sweep Excitation from Node 5 .....	93
Figure 4.43: Frequency Response Functions of Roving Hammer Measurements	94
Figure 4.44: Average Frequency Response Function (Roving Hammer).....	94
Figure 4.45: Experimental Mode Shape of the Adaptive Camber Wing at 13.00 Hz (First Out-of-plane Bending Natural Frequency).....	95
Figure 4.46: Experimental Mode Shape of the Adaptive Camber Wing at 49.00 Hz (First Torsional Natural Frequency).....	95
Figure 4.47: Experimental Mode Shape of the Adaptive Camber Wing at 88.75 Hz (Second Out-of-plane Bending Natural Frequency) .....	96

## LIST OF SYMBOLS

- $d$  length of the track / cutout rib.
- $c$  length of the hingeless control surface.
- $w$  width of the representative hingeless control surface.
- $s$  chordwise distance that is measured from the trailing edge.
- TE wing (or representative section) trailing edge.
- $\Delta_{TE}$  deflection at the trailing edge measured normal to the chord line (defined positive down).
- AC aerodynamic center.
- $c_l$  airfoil lift coefficient.
- $c_m$  airfoil pitching moment (w.r.t. aerodynamic center) coefficient.
- $c_d$  airfoil drag coefficient.
- $H$  aerodynamic moment calculated for the hingeless control surface about a spanwise axis running along the rear spar.
- $F$  magnitude of the actuation force.
- $\Delta_{H=0}$  trailing edge deflection of the morphed section that corresponds to zero aerodynamic moment case.

Pu upper skin pressure.

Pl lower skin pressure.

$\theta$  support web slanting angle.

Other parameters are clearly defined whenever applicable.

## **CHAPTER 1**

### **INTRODUCTION**

#### **1.1 Background to the Study**

This thesis study is based on structural design and evaluation of the adaptive camber wing. The adaptive camber wing has two control surfaces having unconventional designs. The design of the unconventional control surfaces and their implementation on the adaptive camber wing is the focus of the study. These unconventional designs are named hingeless control surfaces. They are based on the use of the flexibility of the structure rather than having a fixed rotation about a hinge axis.

#### **1.2 Scope and Limitations of the Study**

The thesis is devoted to the development of the hingeless control surfaces of a wing particularly built for an unmanned aerial vehicle within the scope of ongoing research and development project ‘Aeroservoelastic Analysis of the Effects of Camber and Twist on Tactical Unmanned Aerial Vehicle Mission-Adaptive Wings’ supported by Turkish Scientific and Technological Research Council. The torque-box design of the adaptive camber wing and structural analyses were done by Levent Ünlüsoy [1] and aerodynamic and aeroelastic analyses of the wing were done by Erdoğan Tolga İnsuyu [2]. Thus, the wing and hingeless control surface geometries are used as it is in the thesis.

Manufacturing of the hingeless control surfaces and adaptive camber wing is done by Turkish Aerospace Industries (TAI). Selection of materials was based on the available materials in the inventory.

### **1.3 Content of the Study**

Chapter 2 gives a literature survey about mission adaptive wings. The requirement for mission adaptiveness is detailed with historical work done in the field. The recent studies for morphing wing structures are presented.

Chapter 3 is devoted to the development of the camber morphing concept. Finite element models of representative sections are created for structural analyses. Aerodynamic analyses are used to determine the aerodynamic coefficients and pressure loading for the representative section. Coupled analyses are done to size the inner components of the camber morphing concept.

Chapter 4 describes the implementation of the camber morphing concept to create hingeless control surfaces. Structural analyses of the hingeless control surface are presented and prototype manufacturing is explained. Finally, the wing with hingeless control surfaces is structurally analyzed. Dynamic analyses compared with experimental data are presented.

## **CHAPTER 2**

### **LITERATURE SURVEY**

#### **2.1 Introduction**

This chapter presents a literature survey on the mission adaptive wings. The survey first details the motivation for the use of mission adaptive wings and history of the main studies conducted in this area. Then the latest studies involving morphing wings are presented.

#### **2.2 Mission Adaptive Wing**

Fixed wing aircraft geometry is designed for specific flight conditions and they perform best at that design point; however the design criteria, i.e. Mach number, altitude, weight, change during flight resulting in compromised performance. Traditional control surfaces, i.e. flaps, ailerons are used to overcome this phenomenon and they are very effective at the design condition where they provide maximum benefit. However, they have minimal or no effect at the off-design conditions [3]. Moreover, traditional control surfaces have moving parts that require regular maintenance which may be costly. Also, some parts of the control surfaces such as hinges and arms along with the gaps between the control surface and other parts of the wing disturb the flow around the wing and may result in added drag and loss of lift. These factors lead to reduced performance and thus decreased fuel efficiency and higher cost of operation.

Research in mission adaptive wings aims to overcome the inefficient behavior for the off-design conditions [4]. About two decades ago, the ‘Mission Adaptive Wing’ program [5] targeted these issues, but the lack of the required technology at that time resulted in an increase in weight and the complexity of the mechanisms that has limited the success of this program. This program was continued as the ‘Active Flexible Wing’ [6, 7] and the ‘Active Aeroelastic Wing’ [8, 9] programs which lead to studies on the structural design and aeroelastic analysis of flexible wings with multiple traditional leading edge and trailing edge control surfaces [10, 11].

### **2.3 Morphing Wing**

A class of mission adaptive wings is referred to as the morphing wings, because they are able to change their geometry actively to adopt to changing flight conditions for maximized performance. Although many researchers impose strict requirements on what must constitute morphing, in most recent applications the use of unconventional structural designs and materials appears to be the most common point. To improve the definition and benefits of morphing, an assessment process such as the presented by Cesnik. et. al. [16] may be adopted. A more recent and formal definition by the NATO Research and Technology Organization, Applied Vehicle Technology Technical Team declares morphing as a ‘real-time adaptation to enable multi-point optimized performance’ [17]. In morphing wing designs, unconventional structural features are used to alter the wing geometry during flight [13, 14] and to eliminate gaps and surface discontinuities in the control surfaces [19] for improved aerodynamics [18].

As a part of ‘Morphing Aircraft Structures’ program initiated by Defense Advanced Research Projects Agency (DARPA) in 2002, Nextgen Aeronautics and Lockheed Martin developed their own morphing multi-role hunter-killer aircraft

concepts [12-15]. Nextgen's Concept is a planar wing with rotating mechanisms and flexible skins, which can accommodate significant changes in span, wetted area and sweep angle [12, 13]. Lockheed Martin's concept uses folding wings that tuck to the fuselage during high speed conditions [14, 15]. Both concepts were tested in wind tunnel in 2005 and successfully displayed their morphing capabilities. In 2007, Nextgen designed a low speed remotely piloted air vehicle and demonstrated morphing capabilities in a successful flight test.

By applying spanwise and chordwise camber variations on the wing [20], aerodynamic loads can be redistributed adaptively during flight to balance the weight changes, minimize the induced drag and reduce wing root bending moments [23]. The potential increase in lift to drag ratio varies between 3% to 10% for a typical transport type aircraft during cruise [24].

In most applications of adaptive camber wings, conventional structures are replaced or modified to increase flexibility in a controlled manner [3, 4, 19-22, 25]. For instance, the 'belt-rib' [25] approach uses a novel design with multiple spokes that permit camber variations to replace traditional ribs. The concept developed by Ricci et. al. uses linear slides in the trailing edge of the wing to achieve rotating rib concept [21, 22]. Similar concept is employed by Seber et. al. where skins slide relative to each other to create adaptive camber [26]. Twist of the structure can also be controlled to create warping [31]. The compliant trailing edge flap developed by Flexys Inc. [27] uses electricity to re-contour the upper and lower skins. Other studies involve using composite or elastomer type materials specifically designed for morphing [28-30].

## **CHAPTER 3**

### **DEVELOPMENT OF THE HINGELESS CONTROL SURFACE CONCEPT**

#### **3.1 Introduction**

This chapter presents the development of the camber morphing concept and its implementation to create a hingeless control surface. Firstly, the general properties of the wing to which the hingeless control surfaces will be implemented are presented. Then, the iterations on the conceptual design of the hingeless control surface will be shown with emphasis on the structural considerations. During these iterations, the structural finite element models are created using MSC<sup>®</sup> Patran and solutions are obtained using MSC<sup>®</sup> Nastran. The conceptual design is checked for allowable stress limits of the materials used as camber changes are applied. Inner parts of the control surface are sized and placed according to the stress calculations and application points of the actuation forces are finally determined.

Structural analyses are followed by aerodynamic analysis, which are used to estimate the pressure loads acting on the hingeless control surface. These loads are applied on the structural finite element model of the HCS and coupled aerodynamic and structural analyses are performed. Actuation force requirements for the coupled case are revised and other required geometrical changes are done to maintain the desired camber morphing within allowable stress limits.

Finally, the conceptual camber morphing design is tested with coupled structural and aerodynamic analysis.

### 3.2 Adaptive Camber Wing

The rectangular wing to which the hingeless control surfaces are to be implemented on is shown in Figure 3.1. The geometric dimensions of this wing are presented in Table 3.1. In Figure 3.1 the hingeless control surfaces are shown in green. The outboard control surface acts as an aileron and it is actuated during roll maneuvers. The inboard hingeless control surface acts as a plain flap that provides an increased lift force during take-off and landing. Magenta colored spar extensions are used for fixing the wing for structural analysis and experimental purposes.

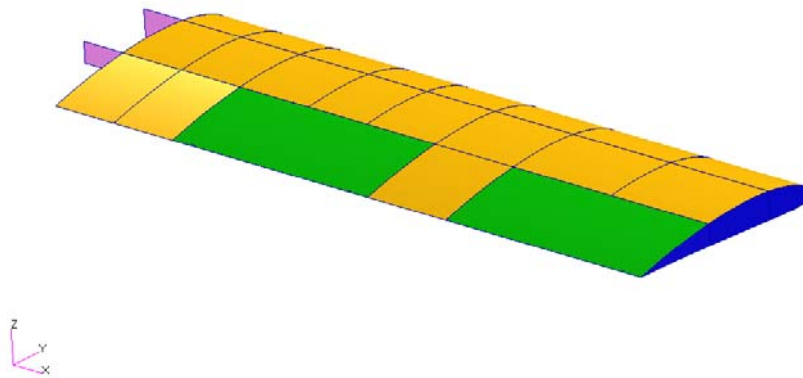


Figure 3.1: Adaptive Camber Wing (with the Hingeless Control Surfaces)

Table 3.1: Wing Geometric Parameters

<b>Geometry</b>	<b>Dimension [cm]</b>
Half Wing Span	150
Chord Length	50
Front Spar from LE	12.5
Rear Spar from LE	30
Control Surface Chord	20
Control Surface Span	50

The wing has a rectangular planform which is chosen so that the control surface trailing edges are parallel to wing leading edge. This lowers the amount of complexity for modeling of hingeless control surface concepts. The wing also has no geometric twist and no dihedral angle; this is to ensure a simpler geometry for aerodynamic force calculations. The cross section of the wing is a NACA 4412 profile [32, 33], which is same through whole span including the parts with hingeless control surfaces.

### **3.3 Structural Modeling and Solution Methodology**

In order to understand and assess the concept of the hingeless control surface better, initial structural modeling is done as a representative section from the wing containing control surface section. This allows the use of 2D aerodynamics to estimate the forces on the section and also allows the usage of higher mesh density for better structural solutions. Also since the emphasis is on the design of the control surface section the primary structure of the wing is assumed to be rigid in analysis. Figure 3.2 shows the primary and secondary structure definitions for

the section. Since the control surface starts after rear spar, secondary structure contains control surface only, while primary structure contains the main load carrying members of the wing.

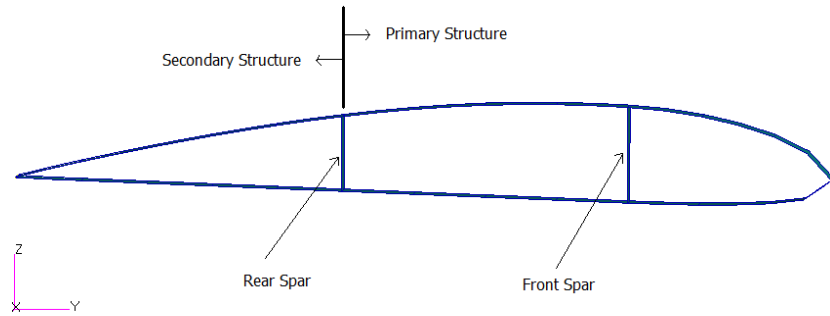


Figure 3.2: Primary and Secondary Structures and Spar Locations

Finite element model of the hingeless control surface includes 4-node quadrilateral shell elements (QUAD4) and multi point constraint (MPC) definitions to help allocate forcing. Also MPCs are used to define connections of structural parts such as support webs and skins where rotations are permitted.

By employing conforming mesh seeds at edges, it is ensured that isometric meshes created for connecting parts have coincident nodes along their edges. This conformity is essential for creating rigid connections of structural parts. Each part is meshed separately then node equivalencing is done to eliminate duplicate nodes and make connections between edges in contact.

The most important feature of structural model is that it employs a semi-open trailing edge section. In the equivalencing of the nodes, the edges of the skins on the trailing edge are slightly separated for upper and lower skins. A zoomed view of the trailing edge is presented in Figure 3.3; since there are separate nodes along upper and lower skins, there is a gap between them.

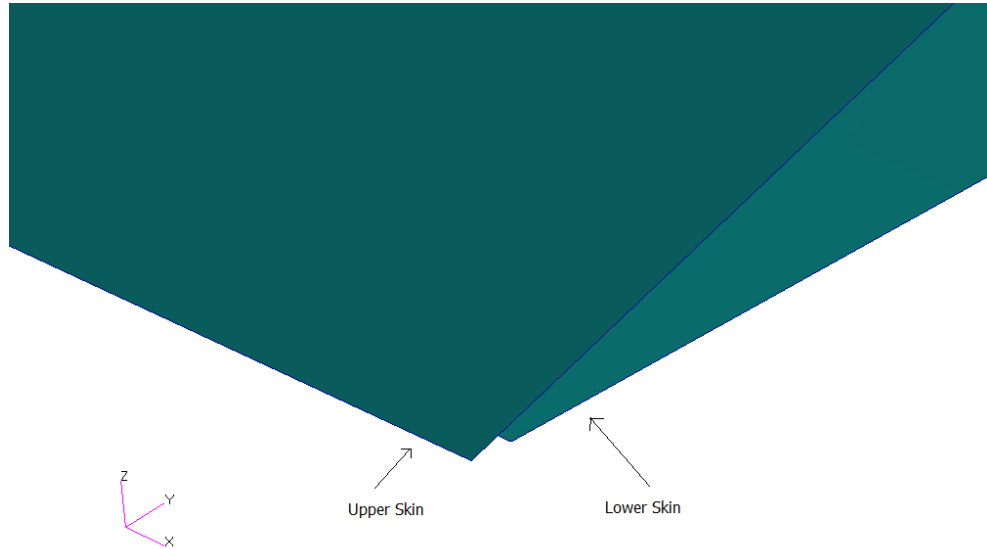


Figure 3.3: Zoomed View of the Semi-open Trailing Edge

To represent the behavior of the hingeless control surface in the structural model correctly, in addition to the gap at the trailing edge, contact surfaces are also defined. These surfaces represent 2D deformable bodies, and the corresponding finite elements are included in the contact definition of the model.

In the contact definition, surfaces that are already in contact or may be in contact with each other are indicated and this information is provided in a table using MSC<sup>®</sup> Patran GUI. During the solution each node associated to the finite elements in the contact definition is checked to see if it's near a contact segment. When it is near a contact segment the contact tolerance, which is shown in Figure 3.4, is compared to the element thicknesses. If the distance between nodes is within the contact tolerance, the bodies experience contact and they do not penetrate each other. In other words contact phenomena create changing boundary conditions for the solution at each equilibrium step, which is a nonlinear behavior.

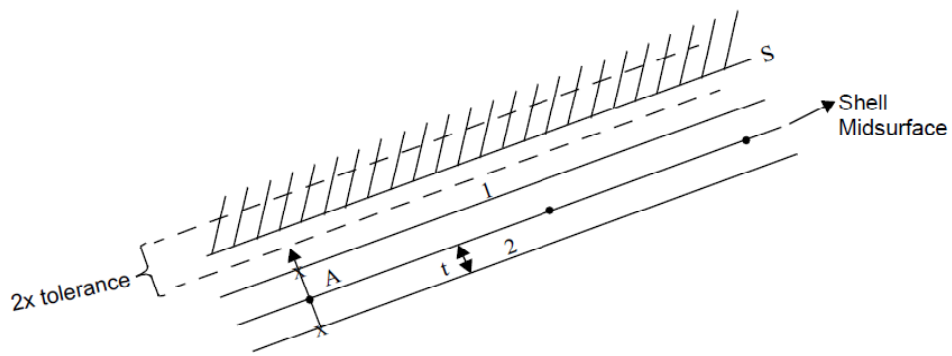


Figure 3.4: Shell Contact Definition [34]

Another important aspect of the structural modeling is the use of follower forces for the actuation of the hingeless control surface. As the control surface morphs into the desired shape, the actuation force follows the movement. This behavior represents the use of flexible push rods that are to be used in the hingeless control surface. A follower force example is shown in Figure 3.5, where the force is always kept at the same relative position and orientation with respect to its initial application point as the body deforms.

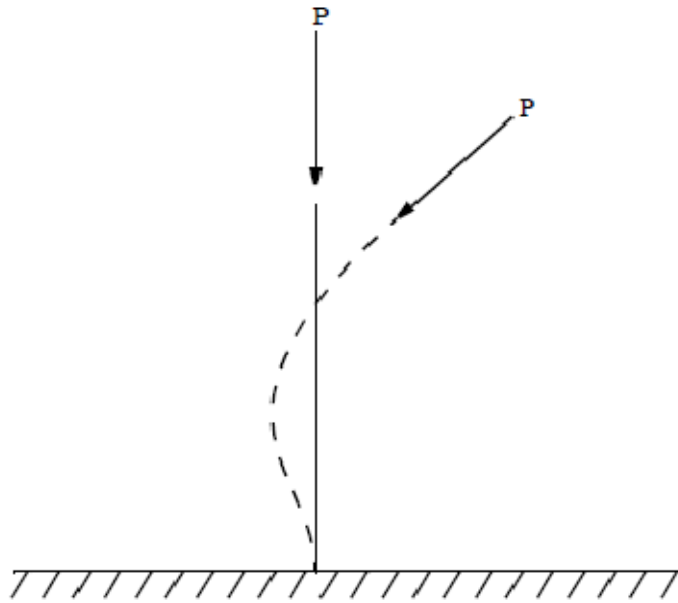


Figure 3.5: Follower Force Example [34]

There is also the possibility that the deformations on the hingeless control surface may lead to geometric nonlinearity in the solution, since upper and lower surfaces bend significantly during camber changes. In order to model the possible nonlinear geometry changes, contact surfaces and follower forces; structural solutions are performed using MSC<sup>®</sup> Nastran Implicit nonlinear solver [34]. However, since Cauchy stresses obtained from the solutions are much smaller than the material yield stress, linear elastic material behavior is assumed.

The solution equation for a nonlinear system is expressed as

$$[K^T]\{\Delta u\} = \{P\} - \{R\} = \{r\} \quad (\text{Equation 1})$$

where  $[K^T]$  is the tangent stiffness matrix,  $\{\Delta u\}$  is the incremental displacement vector,  $\{P\}$  and  $\{R\}$  are the external and elastic force vectors, respectively, and  $\{r\}$

is the residual. By employing tangent stiffness matrix for the solution, nonlinear system is linearized around the iteration point. Then the linearized system is converted to a minimization problem to minimize the potential energy. Loads are applied incrementally and at each load step Newton-Raphson iterations are performed to achieve convergence and equilibrium. During iterations global stiffness matrix is recalculated and other nonlinear aspects like follower force directions are updated. Figure 3.6 shows the flow diagram of the Solution 600 procedure. Inner loop iterates on converging forces in each load increment and outer loop increases loading each time until full forcing is reached.

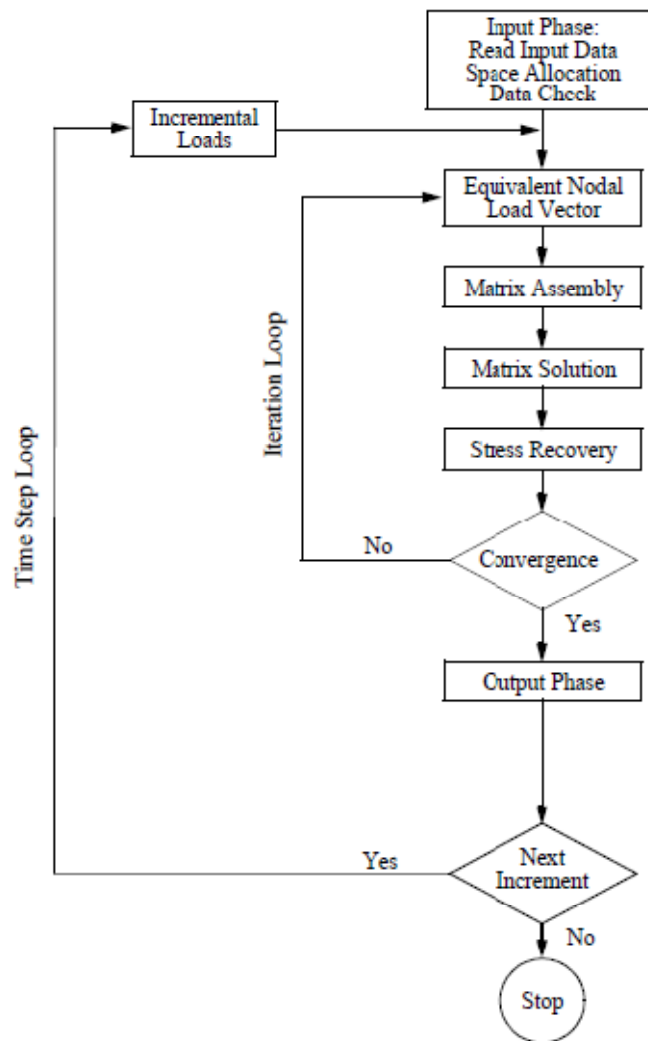


Figure 3.6: MSC® Nastran Implicit Nonlinear Solution Flow Diagram [34]

### 3.4 Structural Modeling of Camber Morphing: Initial Model

The modeling of hingeless control surface is an iterative design process; structural model and the actuation system of the control surface are changed several times throughout the process. In this part of the dissertation, only the key change stages in the design will be presented.

Figure 3.7 shows the initial structural model, which is a coarsely meshed representative section of the wing with the control surface shown in yellow. Some preliminary design attributes are determined using this initial coarse mesh model then a fine meshed model is used for further analysis.

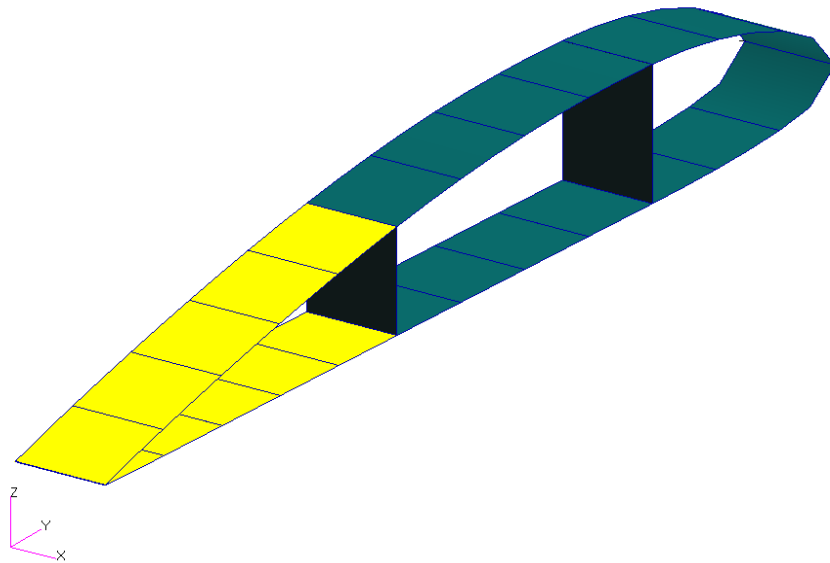


Figure 3.7: Initial Concept Development Model

As a first step, a conventional closed trailing edge model is analyzed. For this analysis trailing edge nodes are equivalenced and model is actuated from the trailing edge. Figure 3.8 shows a typical displacement behavior of the model under a vertical down trailing edge deflection. The most important thing to note about the deformation of this model is the disturbance of the airfoil shape. A wavy shape is observed after morphing which is an undesirable since it results in loss of lift close to trailing edge.

Patran 2007 r1b 08-Sep-08 13:41:33

Fringe: Default, A1:Static Subcase, Displacements, Translational, Magnitude, (NON-LAYERED)

Deform: Default, A1:Static Subcase, Displacements, Translational,

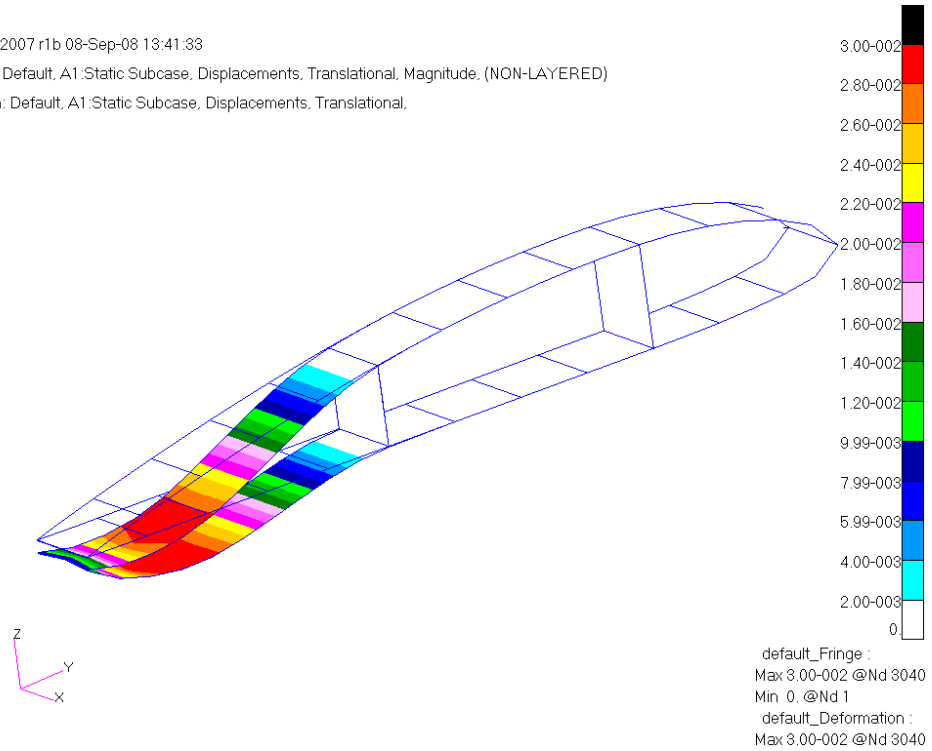


Figure 3.8: Closed Section Displacement Result [m]

This unwanted behavior also results in very high stress values, as shown in Figure 3.9. Thus to relieve the stress in the section, trailing edge is modeled semi-open for further analysis and stiffeners which will be referred as support rods, are used to guide the motion.

Patran 2007 r1b 08-Sep-08 13:42:34

Fringe: Default, A1:Static Subcase, Stress Tensor, , von Mises, At Z2

Deform: Default, A1:Static Subcase, Displacements, Translational.

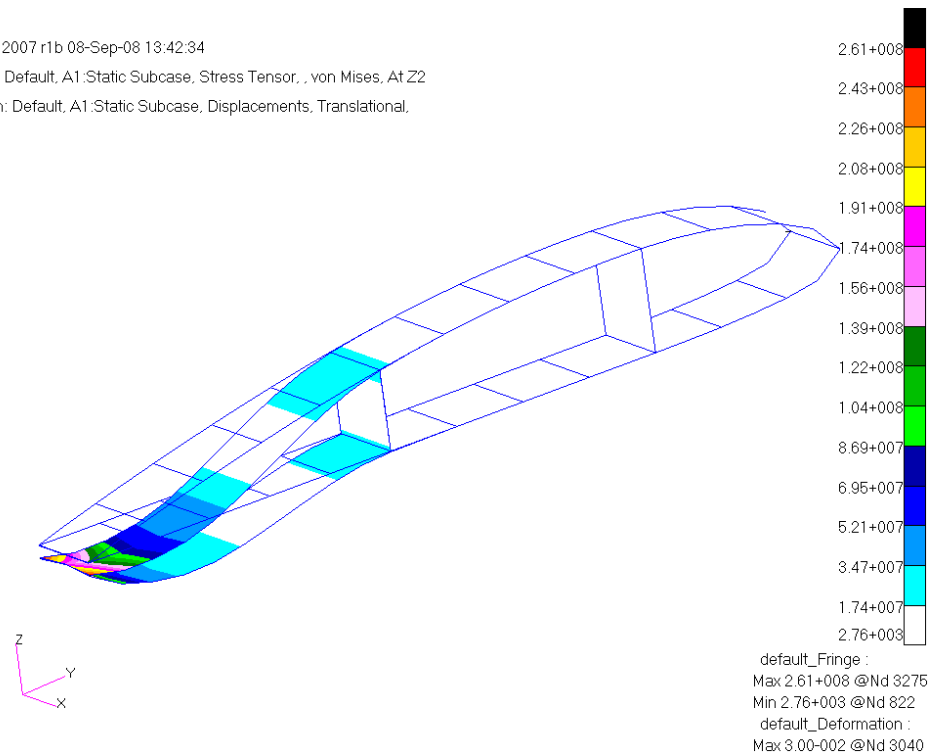


Figure 3.9: Closed Section Stress Result [Pa]

In order to control the motion of the control surface and to model the contact between skin panels a wedge-like structure is placed at the trailing edge. This wedge which is shown in Figure 3.10 is attached to the upper skin rigidly and it can be in contact with lower skin. Support rods and wedge structure help maintain a more desirable aerodynamic shape during morphing. These support rods are modeled as RBE2 type multi point constraints, which link translations of dependent and independent nodes they are connected to.

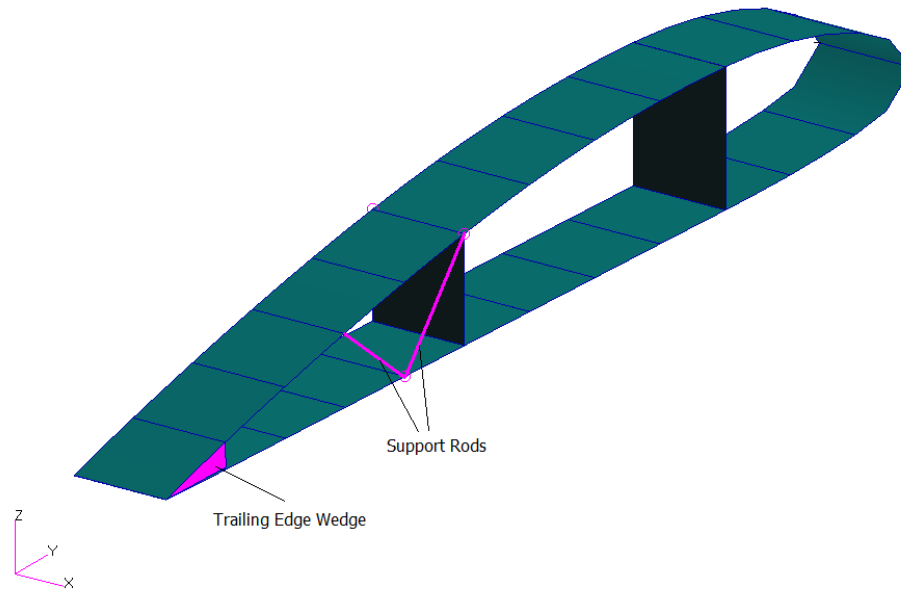


Figure 3.10: Initial Concept Model with Support Elements

Initial setup of these support rods is done by trial and error to avoid excessive curvatures on the skin during camber changes. A more formal approach regarding the placement of support elements is presented in later sections of this dissertation.

Addition of the wedge and support rods to the model enables the control surface to have larger trailing edge deflection within material yield stress limit. Figure 3.11 shows an example shape change of the initial model with support rods and wedge. It can be seen that the morphed section is a more desirable aerodynamic shape compared to that of with no support rods and wedge.

Patran 2007 r1b 08-Sep-08 13:55:54

Fringe: Default, A1:Time = 1., Displacements, Translational, Magnitude, (NON-LAYERED)

Deform: Default, A1:Time = 1., Displacements, Translational.

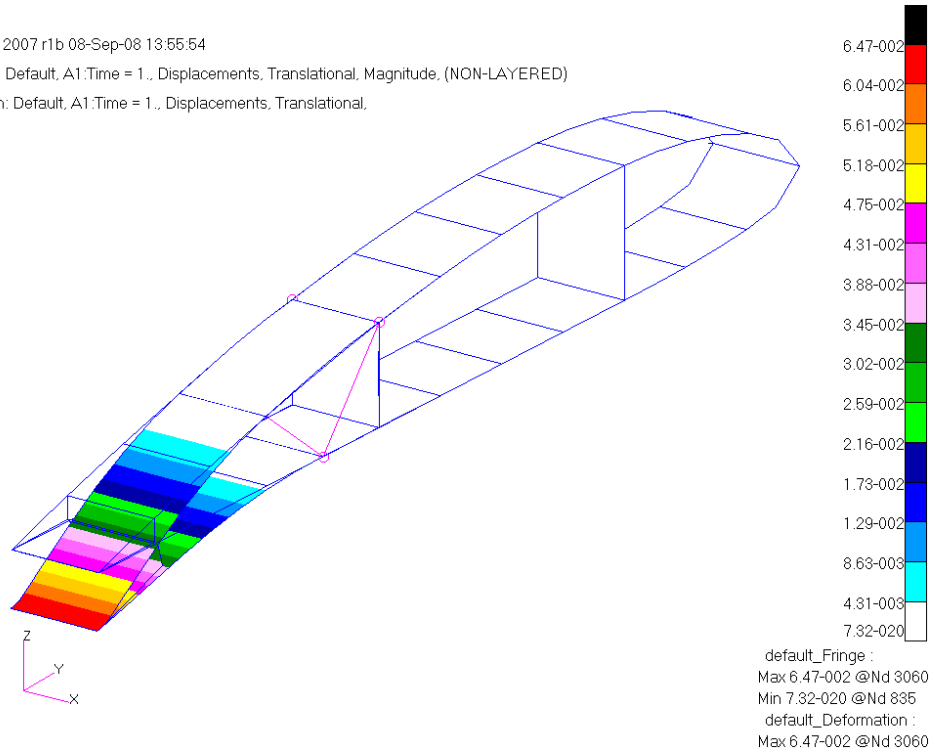


Figure 3.11: Initial Concept Model Example Displacement [m]

This initial model is tested with for positive and negative camber changes with a trailing edge deflection of 2.5cm shown in Figure 3.12. Primary structure is shown as meshed for better visualization.

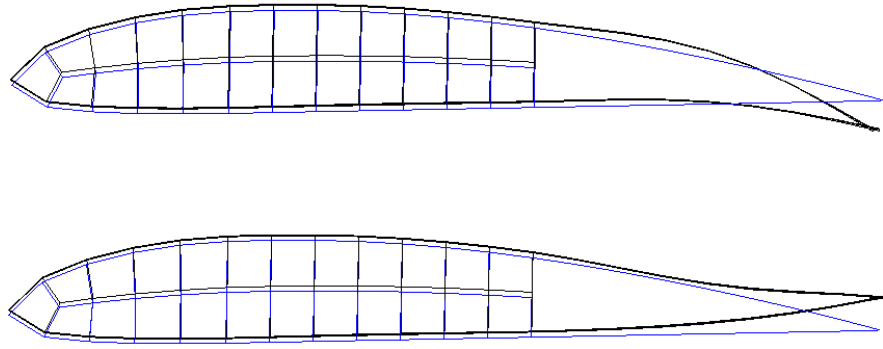


Figure 3.12: Initial Model Example Displacements

### **3.5 Structural Modeling of Camber Morphing: Detailed Model**

Going from the initial model to the detailed one many trial models are considered. Most important observation regarding the trial models is that the wedge must be redesigned as a more compact and lightweight component. After the design process, a simple prototype is manufactured. Figure 3.13 shows the prototype that is made from aluminum with support rods. It also features a control rod which actuates the movement. Trailing edge system is changed from a simple wedge to a railing type mechanism to allow more guided movement. This guided slide allows the actuation forces to be applied more controllably.



Figure 3.13: Hingeless Control Surface Prototype

Example camber increasing and camber decreasing shape changes of the prototype is shown in Figure 3.14 and Figure 3.15. Actuation is done by pushing or pulling the control rod which is attached to the guided slide.



Figure 3.14: Hingeless Control Surface Prototype Camber Increase



Figure 3.15: Hingeless Control Surface Prototype Camber Decrease

Over trials other things that evolved are support rods. In trials with finite element models and also manufactured prototypes, it is seen that usage of rods cannot provide the required support and they have resulted in stress concentrations at their connection points. Thus a more plate like structure called a support web replaces them in detailed structural model as shown in Figure 3.16. This figure shows a representative section of the hingeless control surface that is used in the detailed model. This model features the new structural component, support web

and also guide-slide assembly and cutout rib which control motion of the control surface. Guide-slide assembly also acts as a stiffener attached to lower skin while holding upper and lower skin together, which are not joined at trailing edge.

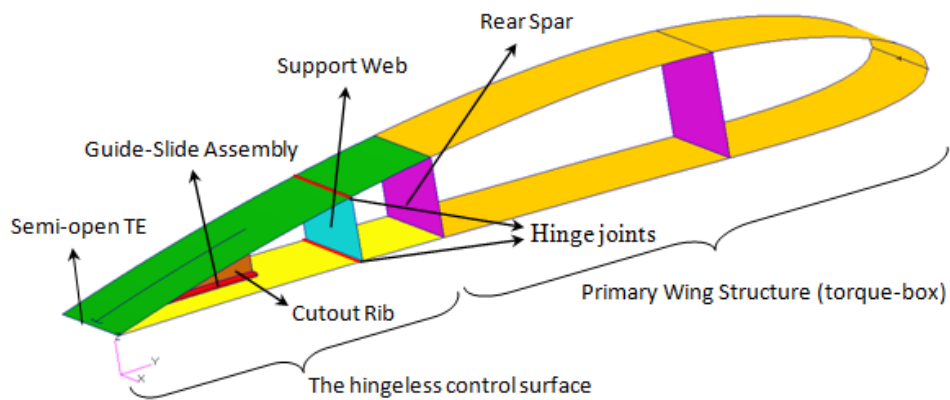


Figure 3.16: Hingeless Control Surface Representative Section

Figure 3.17 shows the components of the guide-slide assembly. Cutout rib is attached to upper skin while track is attached to lower skin. Additionally, it has a flange that is inside the track.

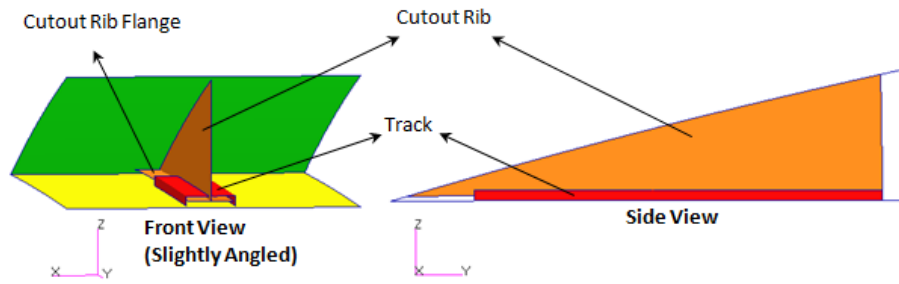


Figure 3.17: Guide-Slide Assembly

Actuation forces are applied to the edges of cutout rib to have relative motion between cutout rib and track. Relative motion initiated at the guide-slide assembly flexes the upper and lower skins located between cutout rib and rear spar. This controlled flexibility provides the control surface camber morphing.

These concerns lead to the main detailed model whose finite element is shown in Figure 3.18. However since the primary wing structure is considered to be much stiffer, only the parts related with hingeless control surface will be used in the preliminary analysis.

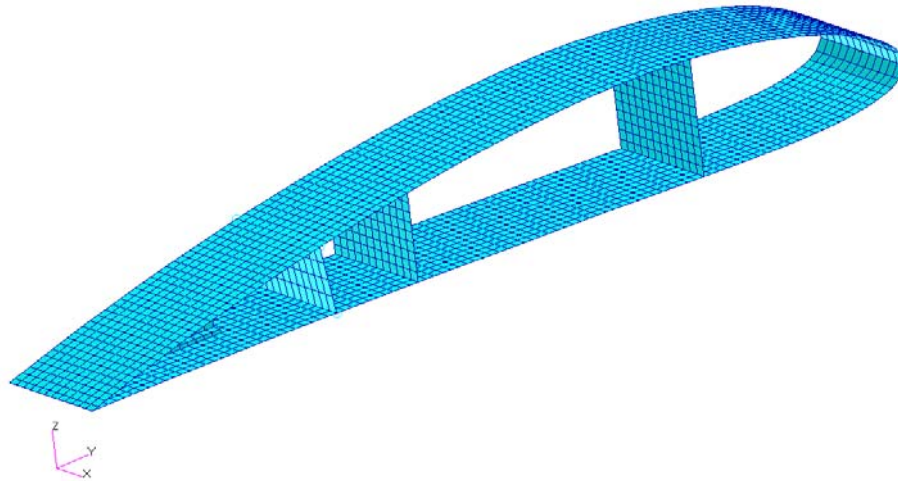


Figure 3.18: Detailed Model Finite Element Mesh

Figure 3.19 shows the finite element model of hingeless control surface with dimension definitions, force application point, boundary conditions, contacting elements and also  $\Delta_{TE}$  direction. For the detailed model, representative width 'w' is chosen as 6cm and hingeless control surface chord length of 'c' comes from global wing design and it is 20cm. Other dimensions; support web location 's' and cutout rib length 'd' is determined in further analysis. Support web is connected to upper and lower skins with the use of MPCs which allow rotation about x-axis while keeping other degrees of freedom same for both support web and skin nodes.

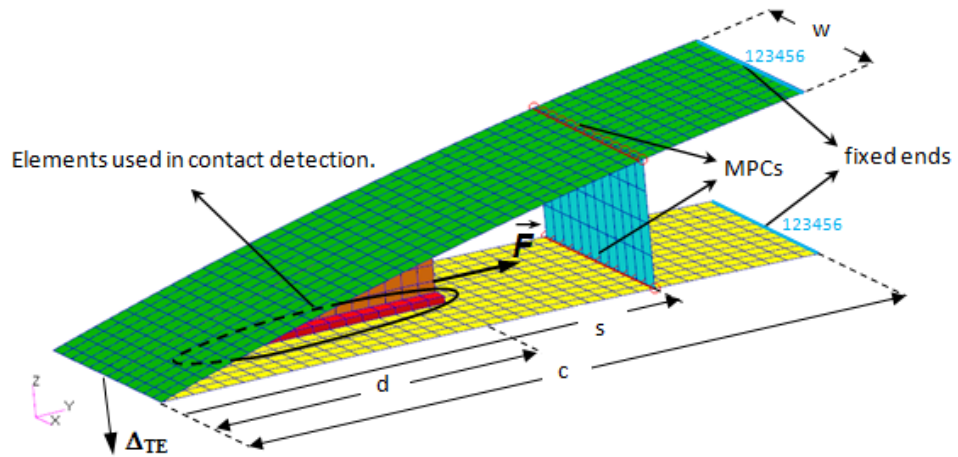


Figure 3.19: Hingeless Control Surface Detailed Model

Another thing to note is the use of contact definitions. Contact is only defined for track and cutout rib to allow contact between each other. Also upper and lower skin is in contact with each other. No other contact definitions are done in order to have faster analysis.

Element types and their numbers are presented in Table 3.2. These numbers represent the global wing section including the primary structure. During the sizing of cutout rib, according to the cutout rib size, model can have a difference up to 10 more QUAD4 Shell elements.

Table 3.2: Element Types and Numbers for Detailed Model

Element Type	Number Used in Model
QUAD4 Shell	2937
RBE2 MPC	27

Materials used in the model and their thickness values according related with structural members are shown in Table 3.3. Composite material used is 7781 E-Glass Fabric with Araldite LY5052 Resin and for metal parts Aluminum 2024-T3 is used. Physical and mechanical properties for these materials are given in Table 3.4 and Table 3.5 [36, 37].

Table 3.3: Materials and Thicknesses Related With Structural Members

<b>Element Property</b>	<b>Material</b>	<b>Thickness</b>
Spar Webs	Aluminum 2024-T3	2.54 mm
Ribs	Aluminum 2024-T3	0.8 mm
Upper & Lower Skins (Primary Structure Part)	4 Layer Laminated Composite	1.08 mm
Cutout Rib	Aluminum 2024-T3	0.635 mm
Track	Aluminum 2024-T3	0.635 mm
Support Web	Aluminum 2024-T3	0.635 mm

Table 3.4: Physical and Mechanical Properties of Aluminum 2024-T3

Density	2780 kg/m <sup>3</sup>
Young's Modulus, E	73.1 GPa
Shear Modulus, G	28.0 GPa
Poisson's Ratio, $\nu$	0.33
Ultimate Strength	483 MPa
Yield Strength	385 MPa
Shear Strength	283 MPa

Table 3.5: Physical and Mechanical Properties of 7781 E-Glass Fabric with Araldite LY5052 Resin

Density	1772 kg/m <sup>3</sup>
Young's Modulus, $E_{11}$	22.1 GPa
Young's Modulus, $E_{22}$	22.4 GPa
Shear Modulus, $G_{12}$	3.79 GPa
Shear Modulus, $G_{23}$	2.96 GPa
Shear Modulus, $G_{13}$	2.96 GPa

### 3.6 Aerodynamic Modeling and CFD Based Solution Methodology

Computational fluid dynamics (CFD) analysis are performed using ANSYS® Fluent for the representative wing section in 2-D settings.

In solutions, structured C-grid aerodynamic meshes are formed using quadrilateral elements. Determination of farfield distances from the airfoil is done according to tutorials provided [38, 39]. Figure 3.20 shows the solution domain dimensions, where ‘c’ is the chord length of the airfoil which is 50cm for our case.

The solution domain is meshed according to the norms provided by tutorials [38, 39]. The aerodynamic meshes are generated using preprocessor tool Gambit of ANSYS® Fluent. Meshed domain is shown in Figure 3.21. Close up views of meshes around airfoil for the standard section and for a morphed section are presented in Figure 3.22 and Figure 3.23. Typical properties of the solution mesh are presented in Table 3.6.

Table 3.6: Aerodynamic Mesh Properties

Number of Cells	12150
Number of Faces	24555
Number of Nodes	12405

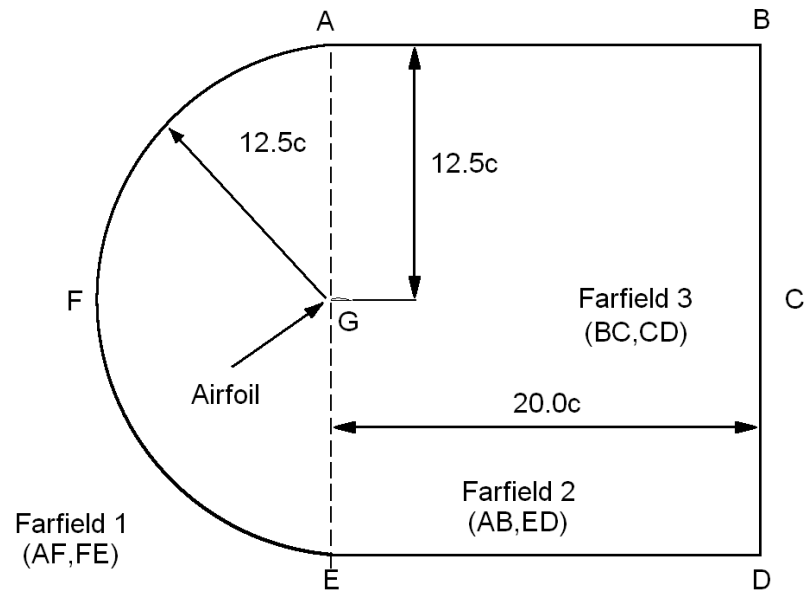


Figure 3.20: Solution Domain for Aerodynamic Analysis

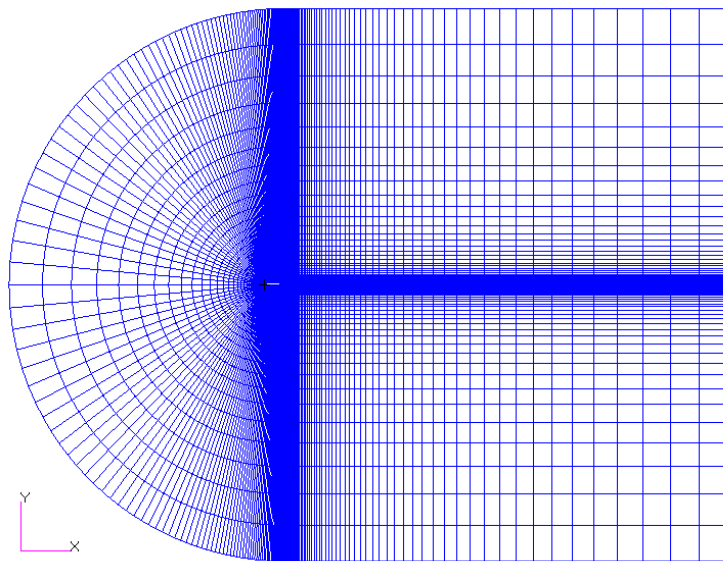


Figure 3.21: C-Grid Aerodynamic Mesh

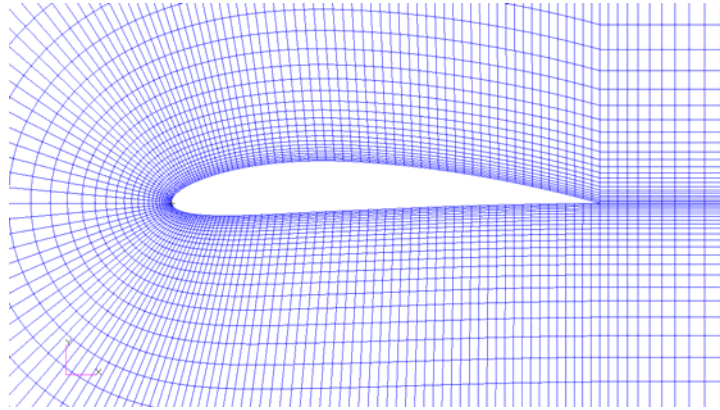


Figure 3.22: Close-up View of Aerodynamic Mesh Around Normal Section

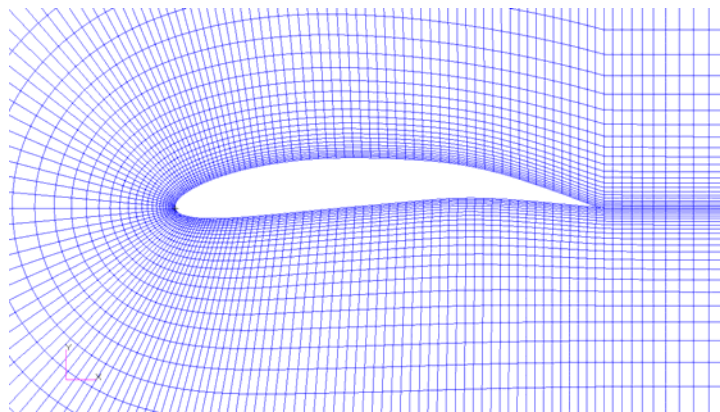


Figure 3.23: Close-up View of Aerodynamic Mesh Around Morphed Section

In order to ensure the consistency of the results corresponding to morphed sections, solution meshes are generated with identical node spacing at the airfoil boundaries. The contours of the morphed sections are determined from solutions of structural finite element model. Spline functions are employed to interpolate between nonconforming aerodynamic and structural node positions.

This node mapping is done via a program written in Python [40]. This program reads the results of structural analysis from the text file output of MSC<sup>®</sup> Nastran

and determines the outer shape of the airfoil section after deformations. Then it maps the deflections to aerodynamic node locations and using automated meshing procedures, runs Gambit to mesh the airfoil and solution domain.

Analyses are performed using two-dimensional incompressible aerodynamics using double precision settings. Viscous effects are taken into account by Spalart-Allmaras turbulence model [41]. Standard sea level atmospheric properties, presented in Table 3.7 are used in solutions and flight speed is selected as 34 m/s. These settings correspond to a Reynolds number of  $Re \cong 950,000$ . Also angle of attack is set to zero.

Table 3.7: Standard Sea Level Atmospheric Properties

Density, $\rho$	$1.225 \text{ kg/m}^3$
Viscosity, $\nu$	$1.7894 \times 10^{-5} \text{ kg/m.s}$
Ambient Pressure, $P$	$101.325 \text{ kPa}$

### 3.7 Assessment of the Concept

In order to assess the hingeless control surface concept, finite element based structural and CFD based aerodynamic analysis are performed on the detailed model. The main objective is to determine the configuration which is well-balanced in terms of actuation force requirements and structural and aerodynamic performances.

### 3.7.1 Actuation Force Placement

The first study involves the application of actuation force at different locations along the edge of the cutout rib. In order to reduce the stress at the force application node, force is applied through a MPC which transfers the force to three adjoint nodes on the cutout rib. This also coincides with the real life application of using a fitting at the force application point. Figure 3.24 shows the RBE2 type MPC used in transmitting actuation force and dimensions of the cutout rib and track.

Force application point is varied in vertical direction for different track and corresponding cutout rib sizes and trailing edge deflection under constant actuation forcing is measured. Horizontal 10N actuation force is used with 6 to 14 cm track lengths.

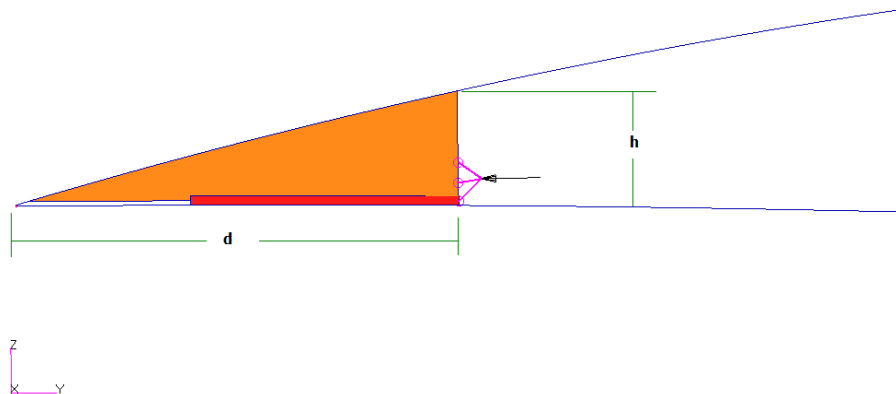


Figure 3.24: Actuation Force Application Point

In Figure 3.25, it can be seen that same amount of actuation force increases trailing edge deflection when applied near the lower skin for all track/cutout rib sizes. It is somewhat an expected behavior since the movement of the hingeless control surface has a pivoting area in the upper skin since the section is a cambered airfoil. Thus force being closer to lower skin creates a bigger moment and eases the control surface movement. In light of this, for further analysis force will be applied parallel to lower skin 5mm above the lower skin to provide some clearance.

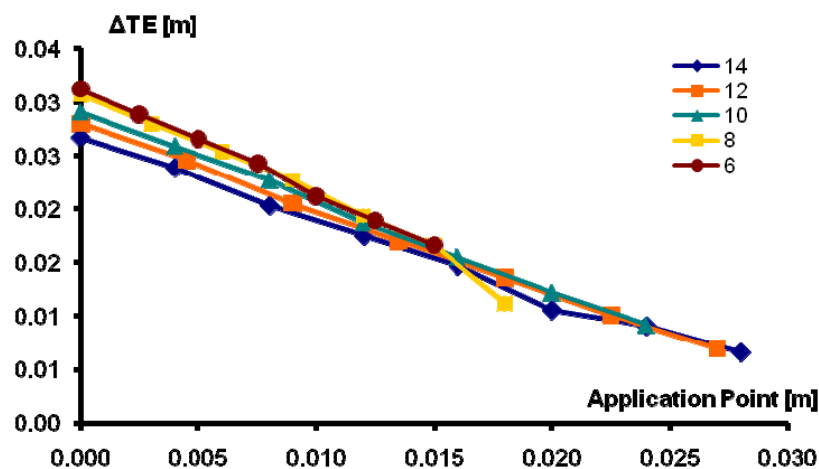


Figure 3.25: Trailing Edge Deflection  $\Delta_{TE}$  vs. Force Application Point as measured wrt Lower Skin for Different Track Sizes

### 3.7.2 Track & Cutout Rib Length

This study focuses on finding the well-balanced track and cutout rib length. Firstly cutout ribs of 6 to 14 cm are morphed using 10N actuation force, then they are actuated by variable force magnitudes and their behavior is investigated. To simplify analysis and to better interpret results, support webs and aerodynamic forces are not included in the analyses. Actuation force is applied to the models

along positive chordwise direction to increase camber and in negative chordwise direction to decrease camber.

Figure 3.26 and Figure 3.27 show the trailing edge deflection  $\Delta_{TE}$  for constant magnitude actuation force applied on different track sized models. Force is applied in both directions to check camber increase and decrease operations. As seen from both figures, trailing edge deflections increase parabolically in magnitude with decreasing track length. In other words, hingeless control surface experiences more camber changes with smaller tracks.

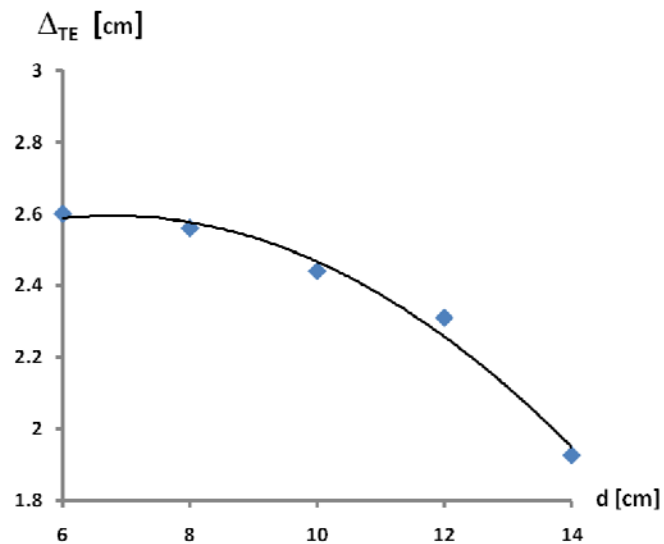


Figure 3.26: Trailing Edge Deflection of Different Track Size Models for Constant Force Applied in Positive Chordwise Direction

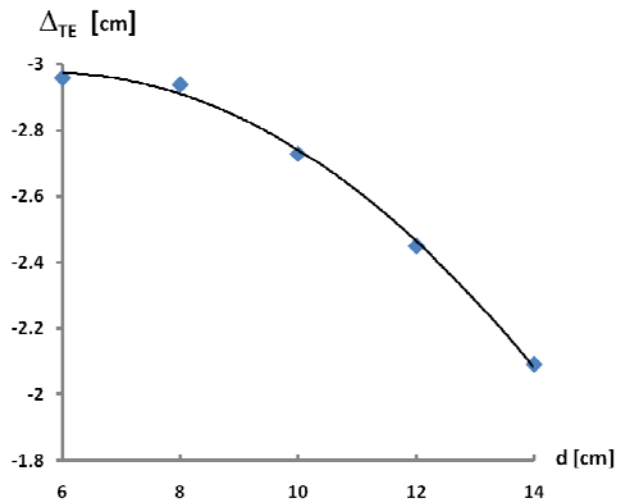


Figure 3.27: Trailing Edge Deflection of Different Track Size Models for Constant Force Applied in Negative Chordwise Direction

There is an adverse effect associated with increased camber change with smaller track sizes; the overall structural stiffness decreases with smaller track and smaller cutout rib that accompany this change. As cutout rib provides inplane stiffness and track acts as a chordwise stiffener, with their decreasing length the sizes of the unsupported skin panel's increase. Therefore although using the smallest track size seems like the best choice for control surface deflection, it is not the best choice for structural integrity. This phenomenon can be observed at the Cauchy stress plots for different track sizes under same actuation forcing. Figure 3.28 shows the stress plot for 6cm track model and Figure 3.29 shows the stress plot for 10cm track model. As can be seen from plots the magnitudes of Cauchy stresses do not vary much but in small sized track bigger parts of skins are under stress. Therefore for better structural stiffness and more deflection values for hingeless control surface a moderate track size is well-suited. For this reason, in further analysis a track size of 10cm will be employed.

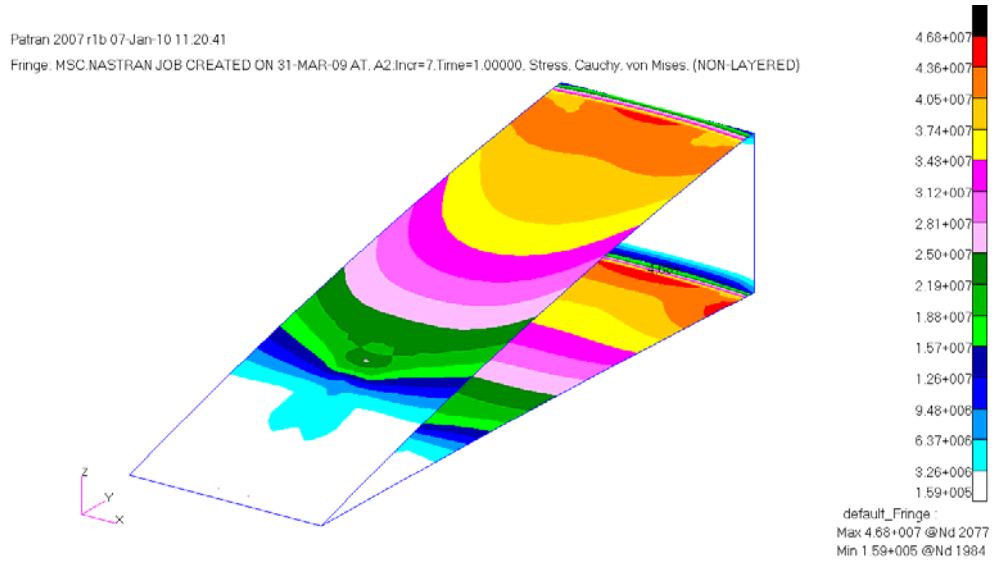


Figure 3.28: Cauchy Stress Distribution for 6cm Track Size with 10N Actuation Force [Pa]

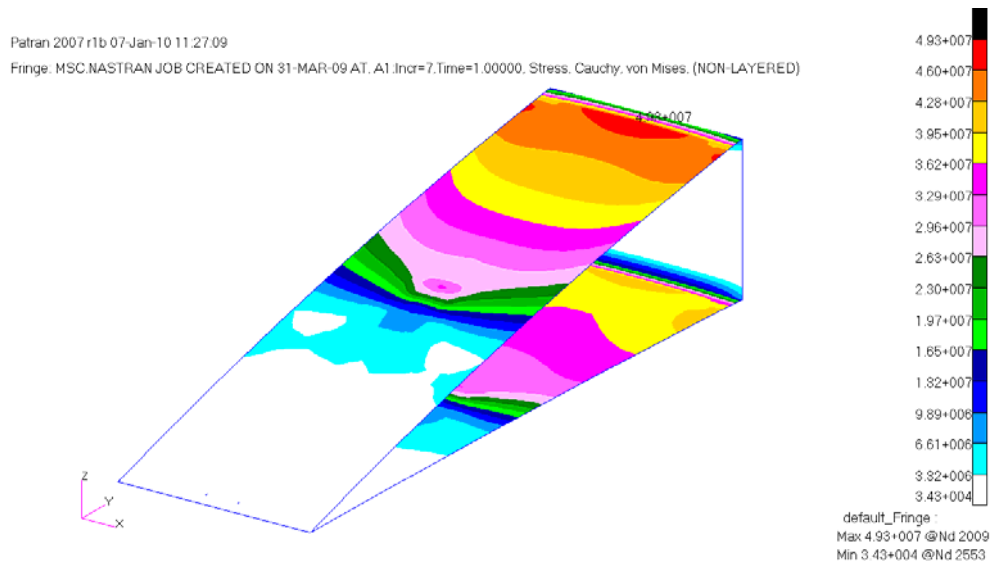


Figure 3.29: Cauchy Stress Distribution for 10cm Track Size with 10N Actuation Force [Pa]

As mentioned earlier, actuation force applied to different track sized model and variation of trailing edge deflection with the magnitude of the applied actuation force is also calculated. Figure 3.30 shows the results of this study. The trailing edge deflections are within the expected operating limit of hingeless control surface up to 10N of actuation force. Also it can be seen that the structural nonlinearities up to these limits are quite weak. Control surface displacements with 10N actuation force for 10cm track size are given in Figure 3.31 for positive camber change and Figure 3.32 for negative camber change.

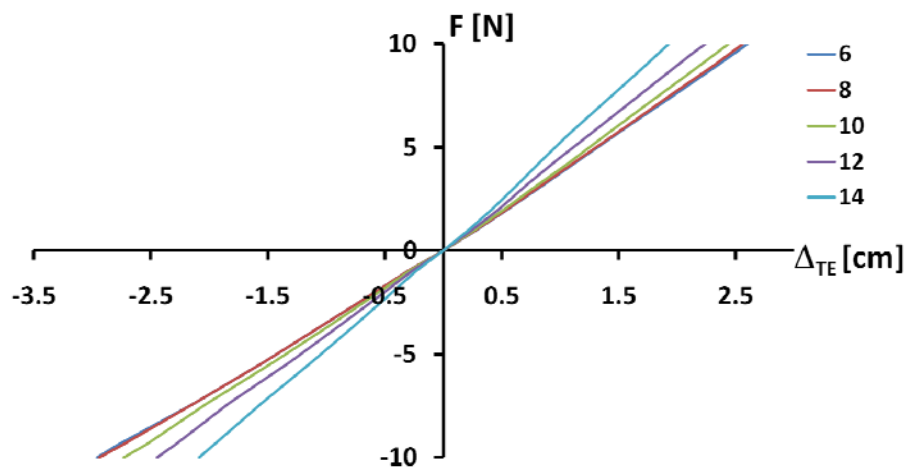


Figure 3.30: Actuation Force (F) vs. Trailing Edge Deflection ( $\Delta_{TE}$ ) for Track Sizes of 6 to 14 cm

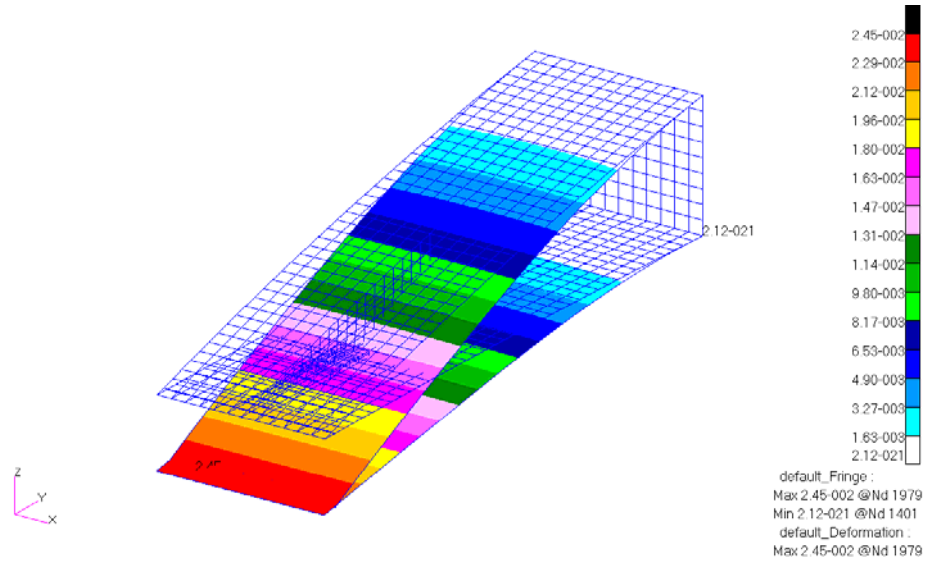


Figure 3.31: Hingeless Control Surface Displacement for Positive Camber with 10N Actuation Force [m]

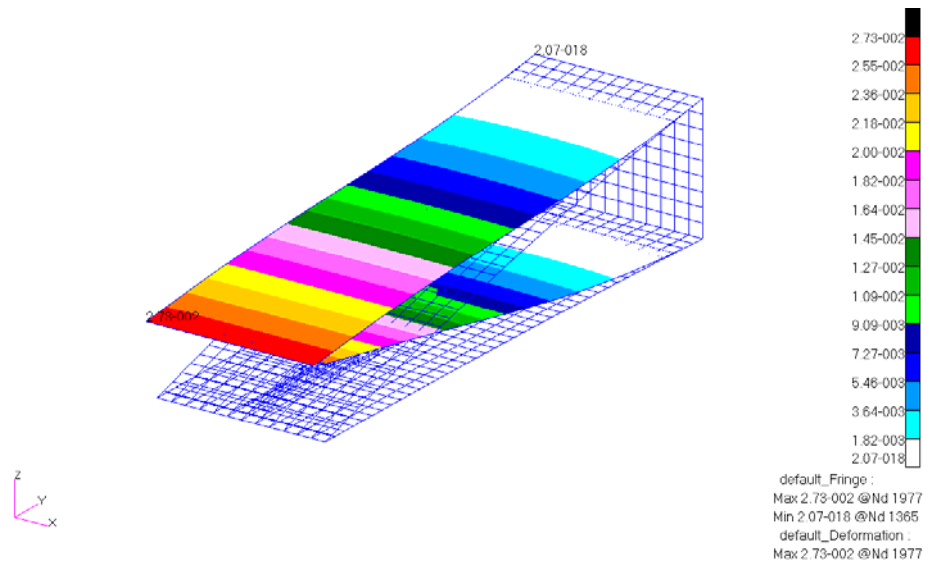


Figure 3.32: Hingeless Control Surface Displacement for Negative Camber with 10N Actuation Force [m]

Actuation forces that generate more trailing edge deflections are also tested to see nonlinear structural effects on the solution. In Figure 3.33 stiffening behavior of the structure can be seen. After 20N of actuation force the system response starts getting lower in terms of trailing edge deflection. Maximum trailing edge deflection can also be observed in the graph to be around 6cm for both positive and negative camber changes. It is the geometric limit which the track and cutout rib are in total contact with skins and cannot move more relative to each other.

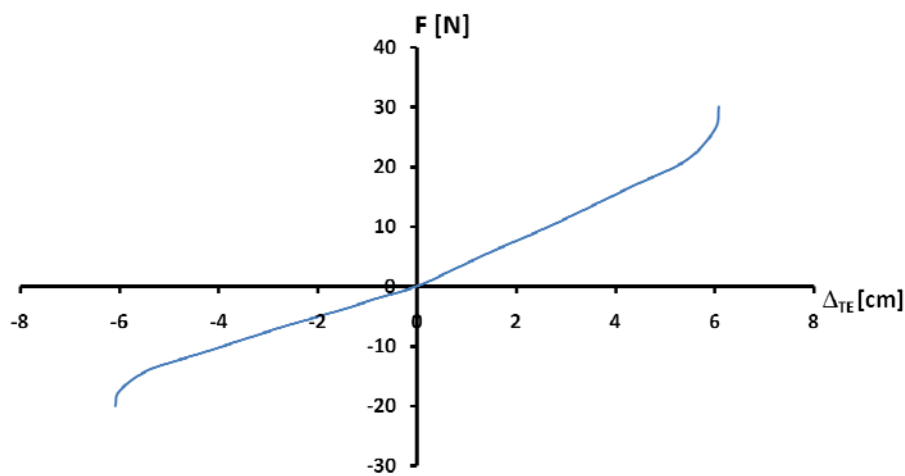


Figure 3.33: Effects of Nonlinearity on Actuation Force

### 3.7.3 Support Web Placement

Another study focuses on support web placement. The orientation of the support web plays an important role as it is the main factor that constraints the movement of the hingeless control surface. Figure 3.34 shows the definitions of support web location 's' and slanting angle 'θ' with respect to vertical axis. In the models used to test the angles and locations; upper edges of the support web is connected to different locations on the upper skin to change angle while lower edges of the web

is connected to the lower skin at a fixed location. This fixed location is determined as the middle point of the free skin part which is not covered by track. A track of 10cm leaves a free skin part of 10 cm, middle of that free skin part on lower skin the support web is placed, which translates to  $s = 15 \text{ cm}$ . As discussed earlier support web is connected to upper and lower skin by MPCs allowing rotations about x-axis. In this study a model with 10cm track is used with 10N actuation force in positive chordwise direction.

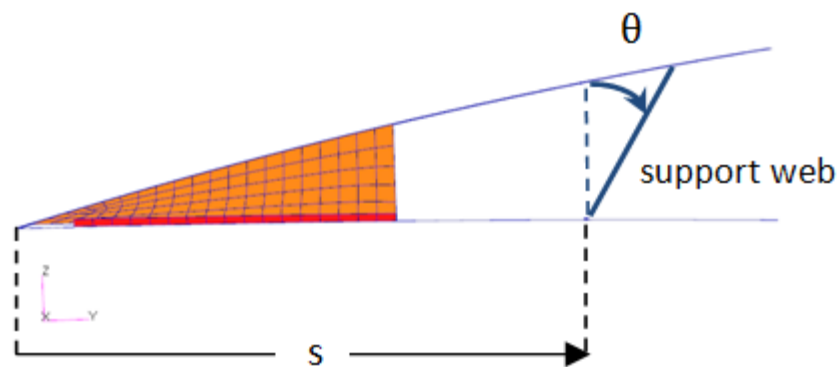


Figure 3.34: Support Web Location and Slanting Angle Definitions

In order to determine the optimum slanting angle for support web, the strain in it is investigated. This is done via checking the distance changes between the nodes it is attached to before and after the camber variations.  $L_{initial}$  is the distance between upper and lower skin location where the support web is connected.  $L_{final}$  is the same distance after deformation of the hingeless control surface. These distances are used to determine slanting angle of the support web which constraints the system. If the percent change in the distance after deformation is small, the support web connected to these nodes does not have significant amount of strain. This lead to having the desired camber change without attenuating useful

actuation energy as the structure becomes unnecessarily strained at the support web. The results of this study for a single support web are shown in Table 3.8 where the highlighted row shows the least amount of percentage change for a specific slanting angle.

This behavior is also checked through trailing edge deflections of models. Figure 3.35 shows the percentage reduction in trailing edge deflection of models with support webs compared to the model with no support web. This result is in perfect correlation with the nodal displacement change of support web connection nodes; less displacement between connection leads to more energy used for the hingeless control surface movement.

Table 3.8: Single Support Web Case ( $s = 15 \text{ cm}$ )

$\theta$ (degrees)	$L_{\text{initial}}$ (cm)	$L_{\text{final}}$ (cm)	$ \Delta L /L_{\text{initial}}$ (%)
-16.3	3.585	3.513	1.999
-8.2	3.562	3.544	0.508
-0.1	3.609	3.640	0.872
7.6	3.723	3.797	2.002
14.72	3.898	4.007	2.813

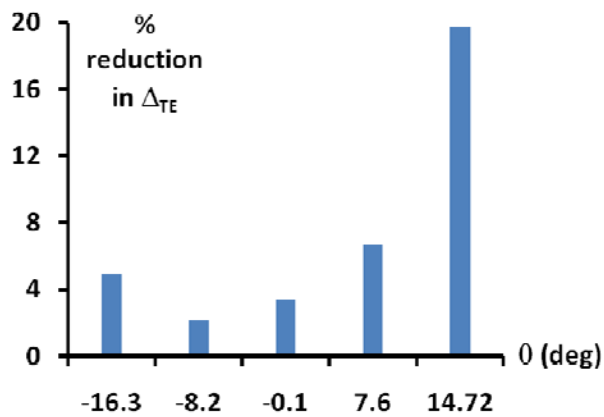


Figure 3.35: Percentage Reduction in Trailing Edge Deflection for Different Support Web Slanting Angles

Displacement plots for 14.72° and -8.2° oriented support web model analysis with 10N actuation force in positive chordwise direction are presented in Figure 3.36 and Figure 3.37 respectively. Same analyses are performed with actuation force in the opposite direction and the results for those cases show movement favors small positive slanting angles but the difference in trailing edge deflection reduction for negative chordwise actuation is less than positive chordwise actuation. Displacement results of the same support web models with negative chordwise actuation are shown in Figure 3.38 and Figure 3.39.

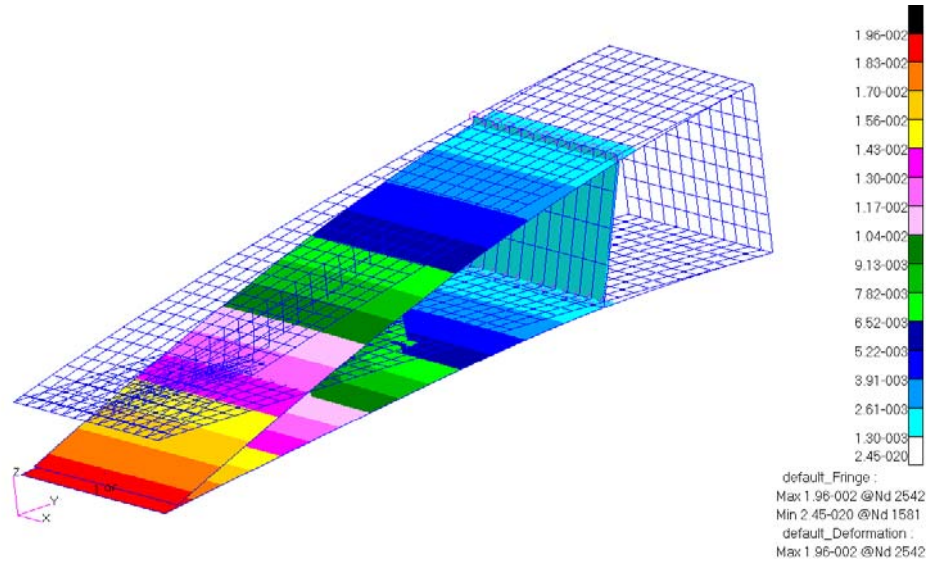


Figure 3.36:  $\theta = 14.72^\circ$  Single Support Web Displacement with 10N Actuation Force in Positive Chordwise Direction [m] (Maximum Displacement = 1.96 cm)

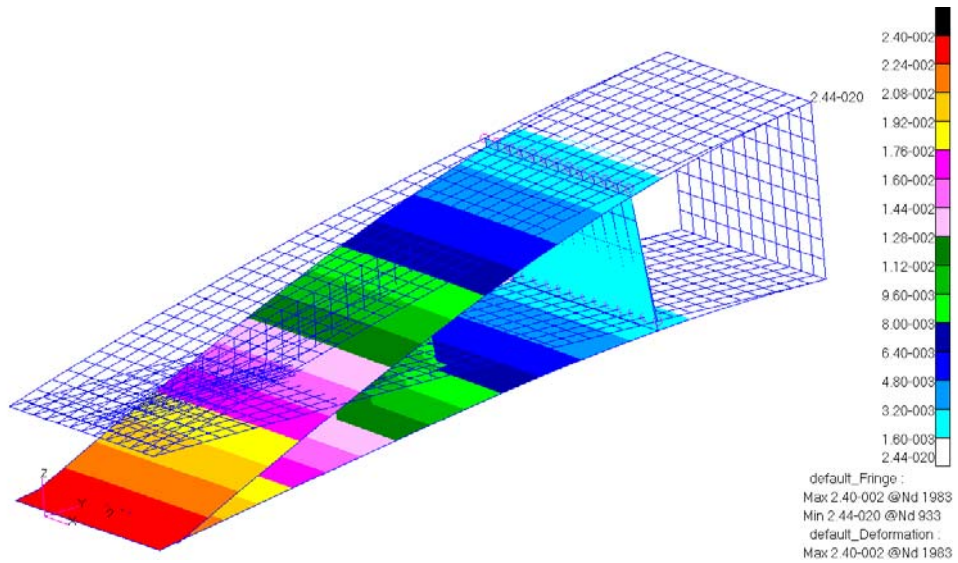


Figure 3.37:  $\theta = -8.2^\circ$  Single Support Web Displacement with 10N Actuation Force in Positive Chordwise Direction [m] (Maximum Displacement = 2.40 cm)

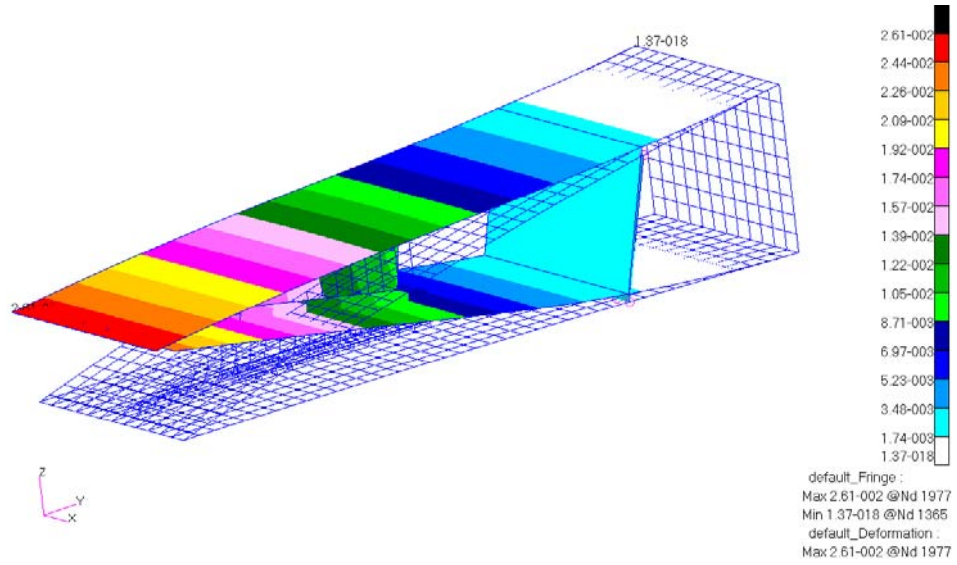


Figure 3.38:  $\theta = 14.72^\circ$  Single Support Web Displacement with 10N Actuation Force in Negative Chordwise Direction [m] (Maximum Displacement = 2.61 cm)

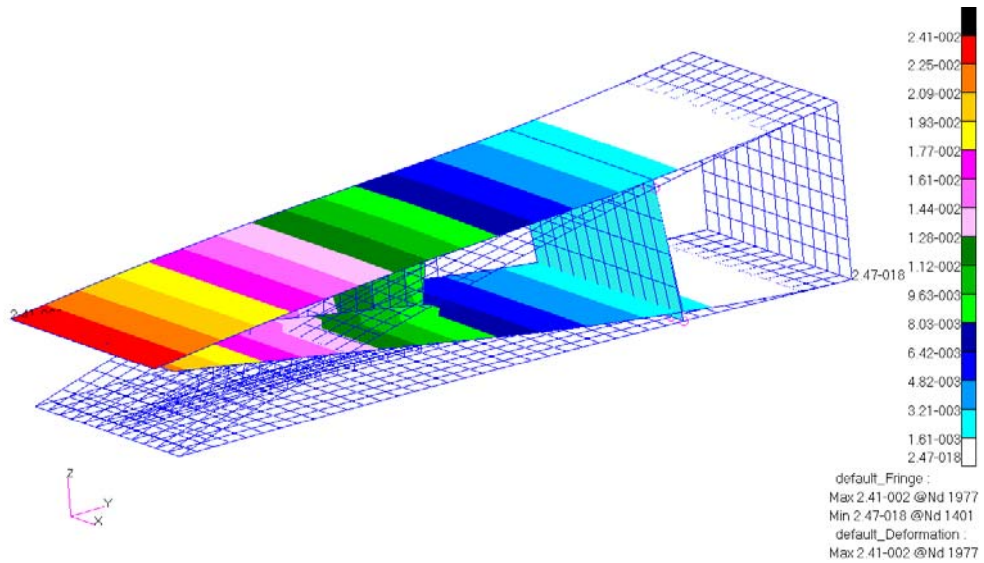


Figure 3.39:  $\theta = -8.2^\circ$  Single Support Web Displacement with 10N Actuation Force in Negative Chordwise Direction [m] (Maximum Displacement = 2.41 cm)

Similar study is conducted with two support webs at  $s_1 = 14$  cm and  $s_2 = 17$  cm with different slanting angles for both support webs. Table 3.9 shows the results of this study. The results are presented in the same manner showing distance changes between nodes where the support webs are connected to the skins, the results that have lowest nodal distance change are highlighted.

Table 3.9: Double Support Web Case ( $s_1 = 14$  cm and  $s_2 = 17$  cm)

	$\theta$ (degrees)	$L_{initial}$ (cm)	$L_{final}$ (cm)	$ \Delta L /L_{initial}$ (%)
Support Web 1	-17.3	3.386	3.301	2.494
	-8.7	3.360	3.340	0.600
	-0.1	3.409	3.449	1.179
	8.0	3.528	3.621	2.639
	15.5	3.712	3.848	3.682
Support Web 2	-14.7	3.969	3.920	1.231
	-7.4	3.949	3.934	0.386
	-0.1	3.992	4.006	0.360
	6.9	4.096	4.135	0.948
	13.5	4.256	4.313	1.350

Two support web model has lower Cauchy stress distribution but also has lower trailing edge deflection compared to the models with one support web. Cauchy stress plots for the best cases of one ( $\theta = -8.2^\circ$ ) and two ( $\theta_1 = -8.7^\circ$ ,  $\theta_2 = -0.1^\circ$ ) support web models are shown in Figure 3.40 and Figure 3.41 for 10N positive chordwise actuation. Also displacement of the model with two support web is presented in Figure 3.42. Trailing edge deflection is 2.32cm when it is 2.40cm for one support web case. The gain in stress is much lower compared to the loss in trailing edge deflection, thus for further analysis models with one support web are used.

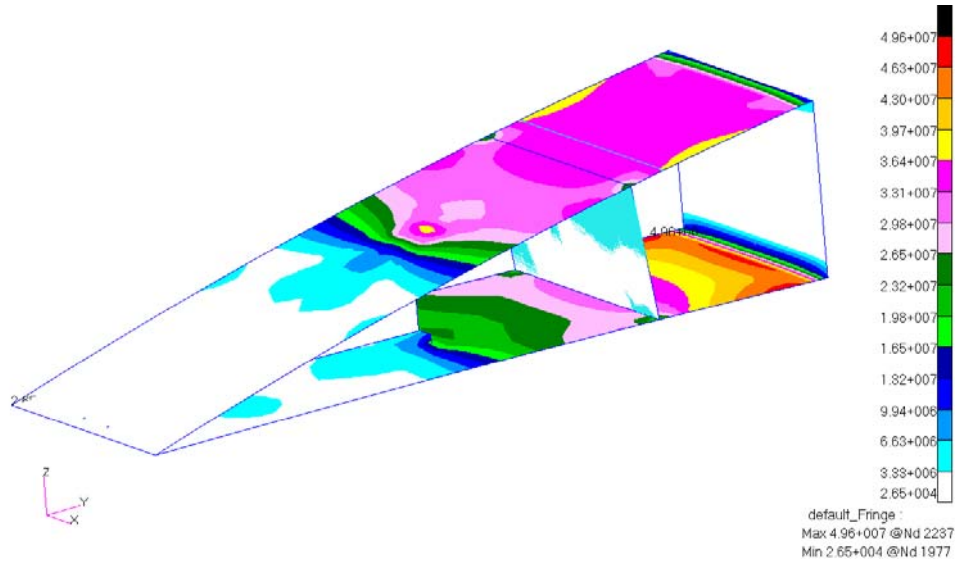


Figure 3.40: Cauchy Stress Distribution of Model with Single Support Web (10N Positive Chordwise Actuation) [Pa]

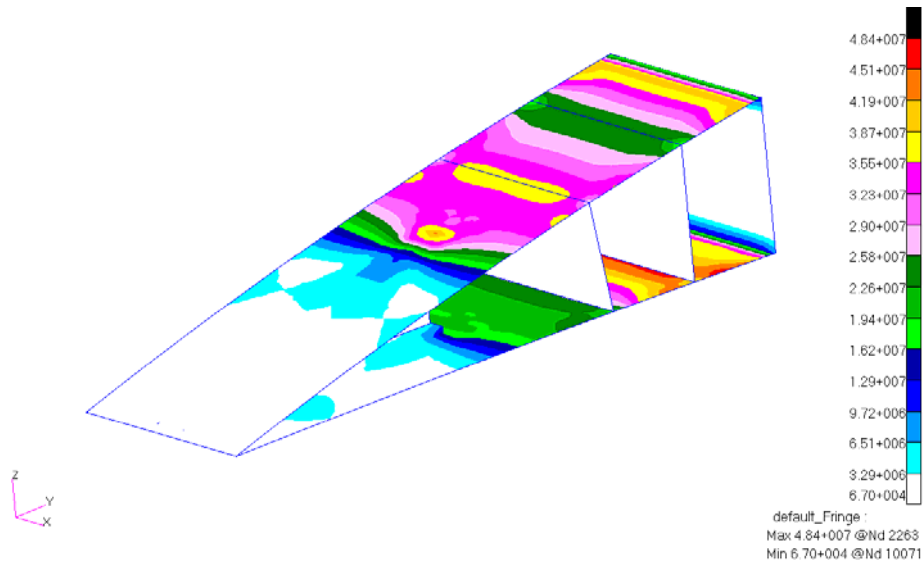


Figure 3.41: Cauchy Stress Distribution of Model with Two Support Webs (10N Positive Chordwise Actuation) [Pa]

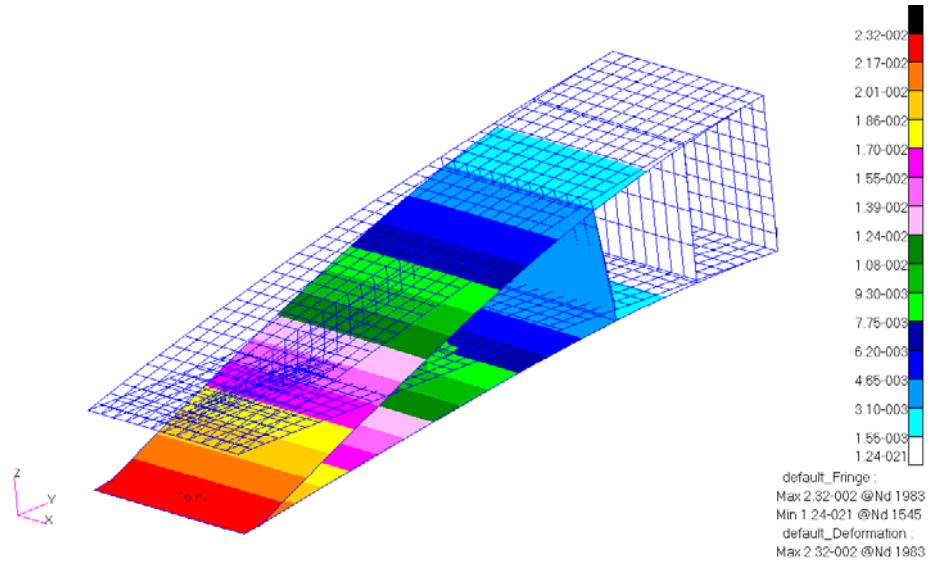


Figure 3.42: Displacement of Model with Two Support Webs (10N Positive Chordwise Actuation) [m]

### 3.7.4 Aerodynamics of the Representative Section

As the final study of the concept assessment, CFD based aerodynamic analyses are performed for models with track lengths of 6 to 14cm having one support web at  $s = 15\text{cm}$  with slanting angle of  $\theta = -8.2^\circ$ . Using different magnitude actuation forces in both directions, structural analyses are performed to find the displacements and from the contour of the new section from the structural deformations aerodynamic analyses are performed to find pressure distribution. These pressure distributions are then used to calculate lift coefficient ( $C_l$ ), drag coefficient ( $C_d$ ) and pitching moment coefficient ( $C_m$ ) with respect to aerodynamic center. Variation of these coefficients with trailing edge deflections are shown in Figure 3.43 - Figure 3.45.

It can be seen that the data points for lift and pitching moment coefficients are distributed in very close proximity of straight lines. In other words the morphing

of the hingeless control surface acts a linear device that changes lift and pitching moment. Since the camber changes induced are small enough not to create significant flow separation the camber change acts as a simple flap or aileron mechanism. Also the deflections are within linear structural deflection limits, thus helping the linear behavior of aerodynamic coefficients. The main result coming from these findings is that the aerodynamic parameters are affected directly by trailing edge deflection because of the fact that this deflection characterizes the camber of the section since other parts of the hingeless control surface follow the movement of the trailing edge smoothly. Therefore aerodynamic coefficients are quite insensitive to the actual shape of the morphed section but highly sensitive to trailing edge deflection.

The drag coefficients related with the sections investigated also show a similar behavior. Lift vs. drag coefficients graph shown in Figure 3.45 resembles the usual drag polar curves [42]. Thus, this also proves that the aerodynamic coefficients depend strongly on trailing edge deflection rather than the actual morphed shape.

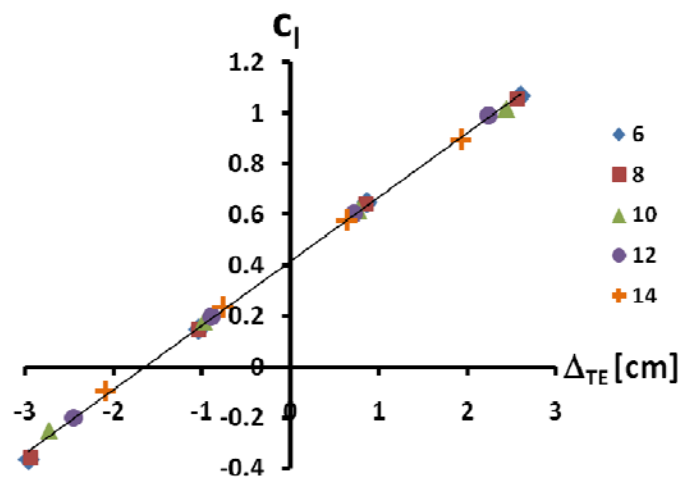


Figure 3.43: Lift Coefficient ( $C_l$ ) vs. Trailing Edge Deflection ( $\Delta_{TE}$ )

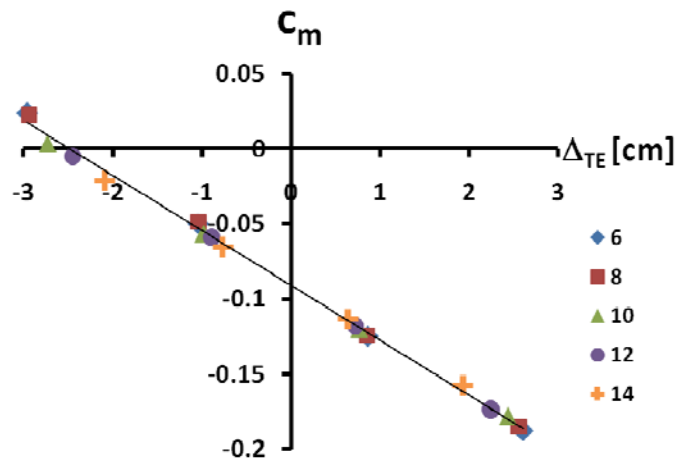


Figure 3.44: Pitching Moment Coefficient ( $C_m$ ) vs. Trailing Edge Deflection ( $\Delta_{TE}$ )

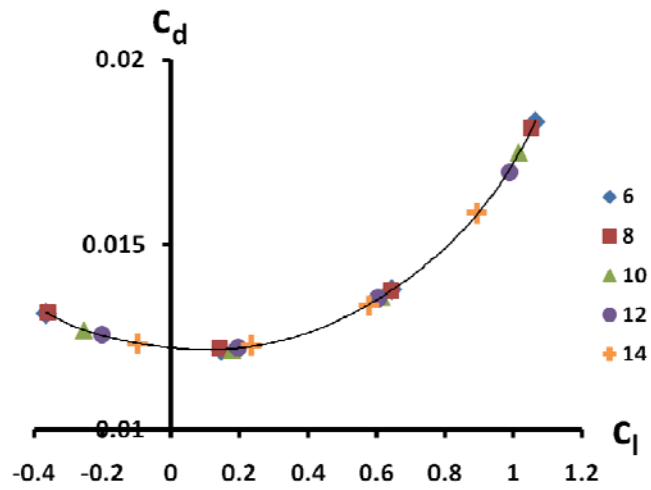


Figure 3.45: Lift vs. Drag Coefficients

### 3.8 Coupled Analysis

In structural analysis including aerodynamic loading, model with 10cm track length and single support web with  $s = 15\text{cm}$  with slanting angle of  $\theta = -8.2^\circ$  will be used, because this model is the most compatible model with the deformation kinematics of the hingeless control surface.

Figure 3.46 - Figure 3.50 show the chordwise static pressure distributions for different morphed states of the hingeless control surface. In these figures 's' is the chordwise coordinate measured from trailing edge and  $P_u$  is the pressure related with upper skin and  $P_l$  is the pressure related with lower skin [26].

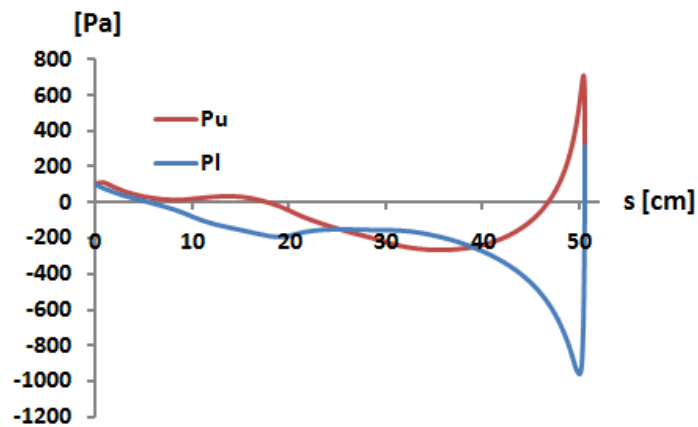


Figure 3.46: Static Pressure Distribution for  $\Delta_{TE} = -2.41\text{ cm}$

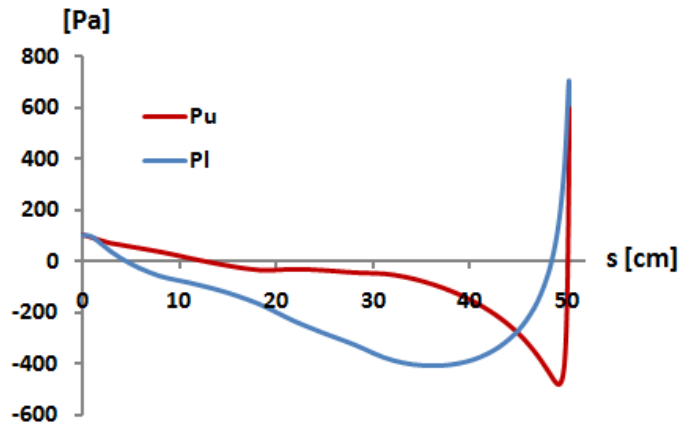


Figure 3.47: Static Pressure Distribution for  $\Delta_{TE} = -0.977$  cm

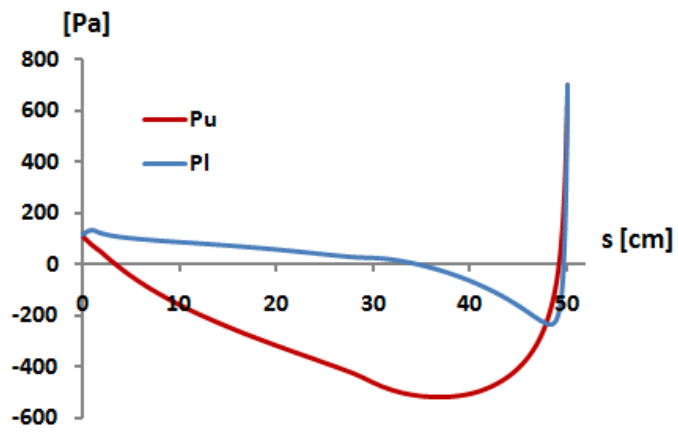


Figure 3.48: Static Pressure Distribution for  $\Delta_{TE} = 0$  (Unmorphed Section)

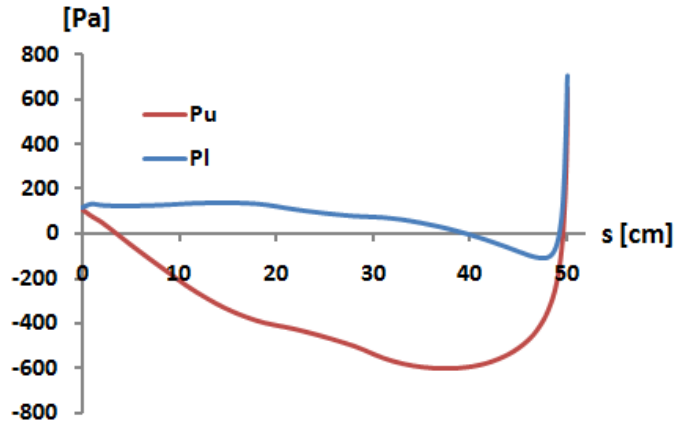


Figure 3.49: Static Pressure Distribution for  $\Delta_{TE} = 0.81$  cm

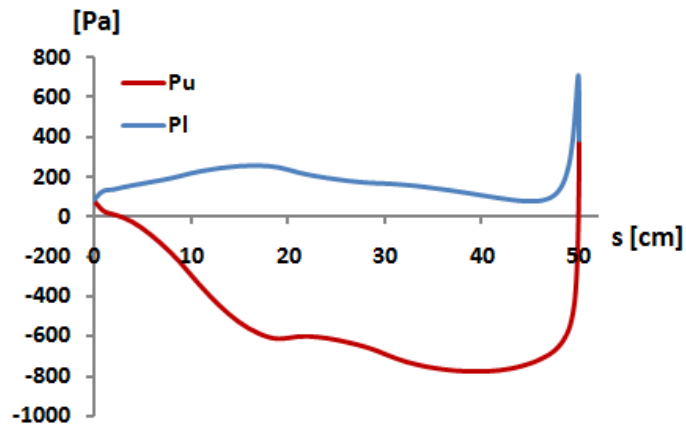


Figure 3.50: Static Pressure Distribution for  $\Delta_{TE} = 2.4$  cm

The aerodynamic pressure distributions calculated are interpolated using polynomial functions between  $s = 0$  and  $s = 20\text{cm}$  then the polynomials are used to define the pressure field for the structural model. First scalar fields with the polynomial data is formed in MSC<sup>®</sup> Patran using PCL then these fields are used to define the pressure field for upper and lower skins [42]. Since the representative

section is small enough in spanwise direction, spanwise variation of pressure is ignored and only chordwise distribution is used.

The most important thing to note is that the calculated pressure distribution is only valid for a specific morphed section and can only be used for that. The coupled analysis is started with mapping the pressures on to the structural model, and then the actuation force is applied in an iterative fashion until desired deformation level is reached. Throughout the analysis trailing edge deflection is checked for convergence. At the end of this step contours from the deformed sections are compared with the initial contours that are used to calculate the aerodynamic loading (pressures). It is seen that after structural analysis using pressures and actuation forces, the section properties match that of the morphed section which is used to calculate pressures. Aerodynamic loads do not create significant local deformations and as was seen in the concept assessment process, the general movement of the hingeless control surface depends on the trailing edge deflection rather than the actual shape of the section. Thus, one aerodynamic solution and one structural solution is enough to determine the system state of coupled solution so aerodynamic calculations are not repeated and structural modifications are not introduced.

Cauchy stress distribution for the hingeless control surface with different trailing edge deflections are presented in Figure 3.51 - Figure 3.53. These include aerodynamic loading and actuation forces, so it is the results of final geometric changes with aerodynamics present. It can be seen that the maximum stress is well below the yield strength of the material used, therefore initial assumption for using linear elastic material properties is also acknowledged. Figure 3.54 shows the superimposed views of the morphed section geometries where trailing edge deflection can be seen clearly.

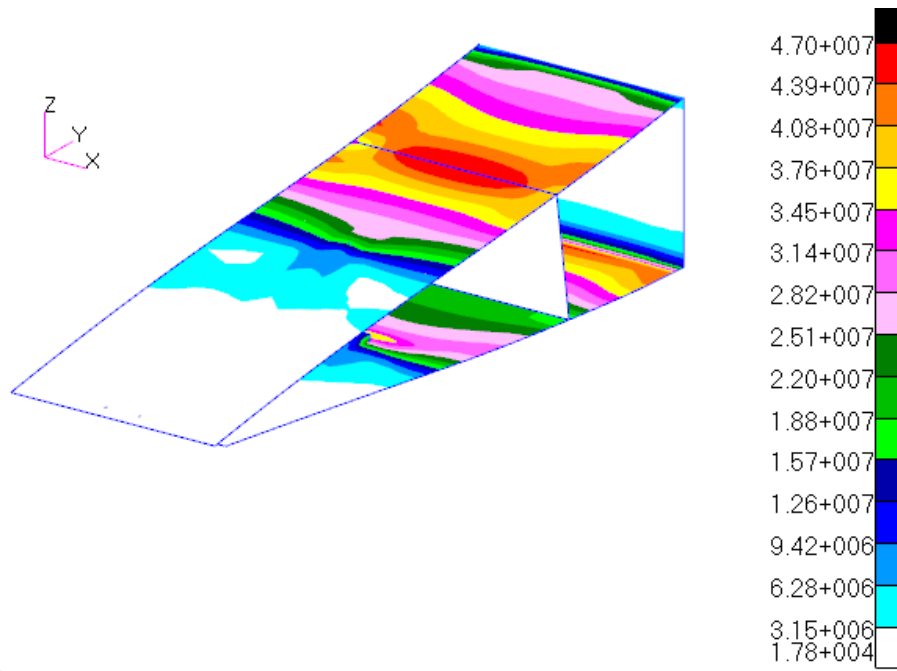


Figure 3.51: Cauchy Stress Distribution for  $\Delta_{TE} = -2.41 \text{ cm [Pa]}$

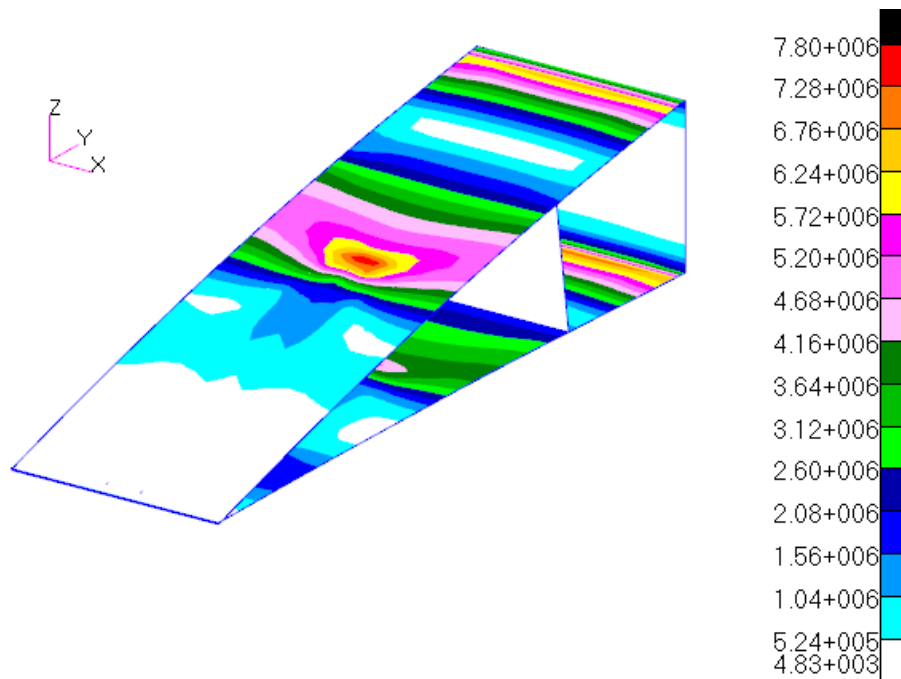


Figure 3.52: Cauchy Stress Distribution for  $\Delta_{TE} = 0 \text{ [Pa]}$

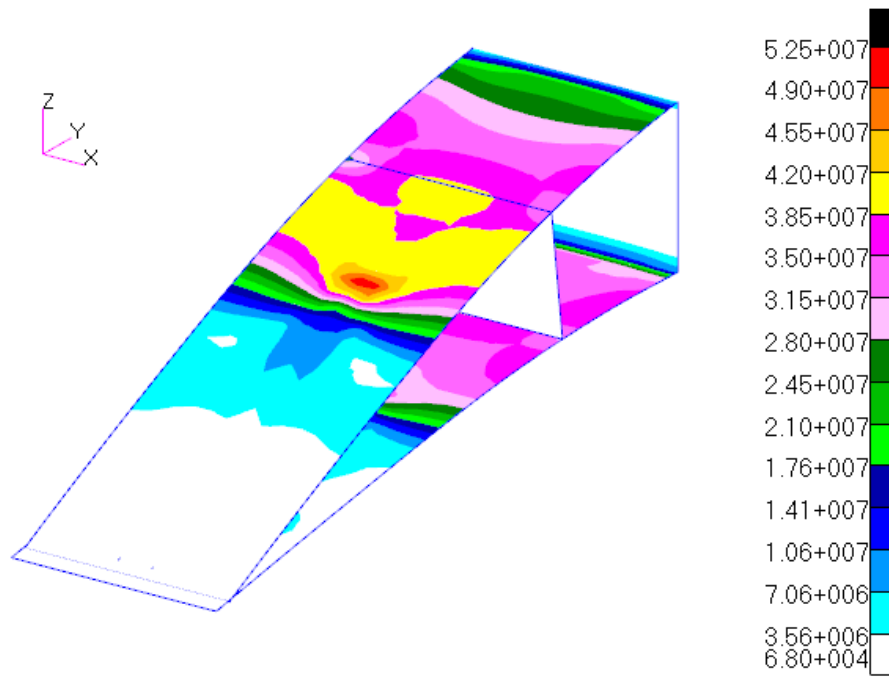


Figure 3.53: Cauchy Stress Distribution for  $\Delta_{TE} = 2.4$  cm [Pa]

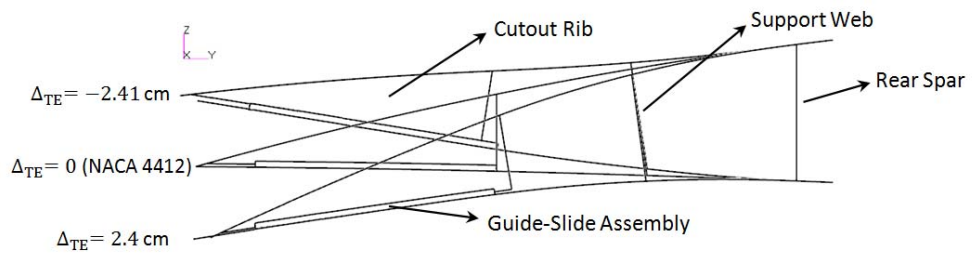


Figure 3.54: Superposed Views of the Hingeless Control Surface for Different Trailing Edge Deflections

Figure 3.55 shows the variation of the actuation force with trailing edge deflection. Actuation force required for a proposed trailing edge deflection with no aerodynamics present and with aerodynamics is calculated. Also the difference the aerodynamics creates for the actuation force to create the same trailing edge deflection is also given in the figure.

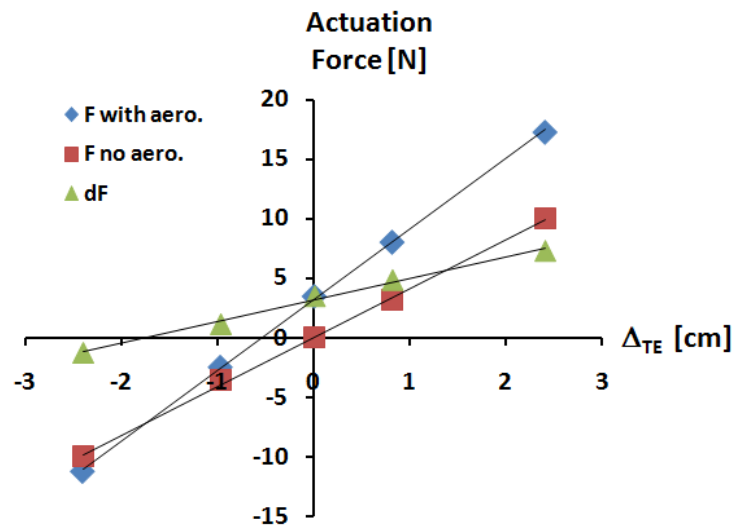


Figure 3.55: Variation of the Actuation Force with Trailing Edge Deflection ( $\Delta_{TE}$ )

It is noted that in the presence of aerodynamic loads actuation force is equal to  $F = 3.3 \text{ N}$  when  $\Delta_{TE} = 0$ . This means that even when the hingeless control surface is undeformed, section is the normal airfoil; some actuation force is required to maintain the shape to counteract the aerodynamic loads.

Another important thing is that when  $\Delta_{TE} \cong -1.7 \text{ cm}$  actuation force is same the case with no aerodynamics loading and with aerodynamic loading. This behaviour is shown in Figure 3.56 where the variation of aerodynamic moment with respect to trailing edge deflection is given. This aerodynamic moment of the hingeless control surface is calculated by considering the effect of aerodynamic pressures

about a spanwise axis located at rear spar. Thus, effectively the aerodynamic moment ‘H’ can be compared to the hinge moment of the control surface as if it is a conventional one. This  $\Delta_{TE} \cong -1.7$  cm corresponds to the trailing edge deflection where there is zero aerodynamic moment, referred to as  $\Delta_{H=0}$ . The same behavior is seen for conventional control surfaces.

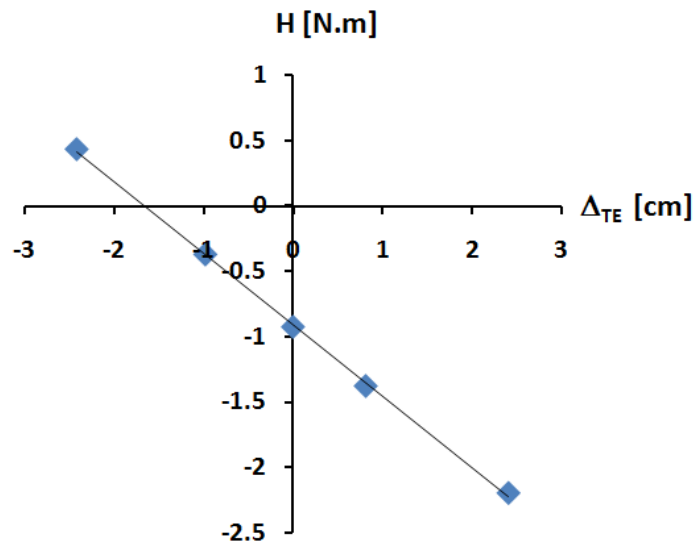


Figure 3.56: Variation of the Aerodynamic Moment ( $H$ ) with Trailing Edge Deflection ( $\Delta_{TE}$ )

### 3.9 Conclusions

In this chapter, the hingeless control surface concept was introduced and models that simulate the morphing of the control surface were presented. Reasons for using a semi-open trailing edge section were justified. Then numerical analyses were performed to assess the structural and aerodynamic aspects of the concept.

The main result of the structural analyses was that even though the finite element models used are based on nonlinear formulations, the results showed a linear behavior for the expected operational range.

Results indicate that the use of shorter track and cutout rib lengths increased the flexibility of the design during camber changes. In other words, for the same amount of actuation force hingeless control surface can have more trailing edge deflection with shorter track lengths. However, use of shorter track and cutout ribs also results in larger unsupported panels, which encounter strength problems that may lead to structural instabilities. To reinforce unsupported panels, slanted support webs were used. Support webs are connected to skins via hinge-type connections in analyses. This connection may be harder to realize in manufacture, since the actual connection point of the webs and their slanting angle plays an important role in the design.

CFD analyses were performed for morphed geometries determined from structural finite element solutions. The results obtained showed that the aerodynamic coefficients have a strong dependence on the camber change, trailing edge deflection, and they are rather insensitive to the actual deformed shape.

As the final study, coupled analyses were performed by using the aerodynamic pressures in structural solution. From the results trailing edge deflection corresponding to zero aerodynamic moment was determined. Also the actuation force required to withstand the aerodynamic loading to keep the section steady with no camber change was calculated.

## **CHAPTER 4**

### **STRUCTURAL DESIGN & ANALYSIS OF THE ADAPTIVE CAMBER WING**

#### **4.1 Introduction**

This chapter presents the implementation of the hingeless control surface concept on full scale control surfaces which are then implemented on the wing. Firstly, control surface models which include the concept of guide-slide assemblies are modeled. Structural analyses for the morphing of control surfaces are performed.

Then, hingeless control surface is manufactured for testing and models are updated with the changes introduced in the manufacturing stage. Updated hingeless control surface models are added to wing geometry. Full wing model is analyzed structurally with hingeless control surfaces.

Finally, modal analysis of the adaptive camber wing having hingeless control surfaces is performed via finite element solutions. Experimental modal analysis of the wing is conducted and comparison of experimental data and finite element solution is presented.

#### **4.2 Theoretical Modeling of the Full Scale Hingeless Control Surface**

Previously, the assessment of the concept for the hingeless control surface is done using a representative section. The representative section is used to determine the

well-balanced geometric properties of the inner structural parts. These inner structural parts are track and cutout rib that form the guide-slide assembly and support webs that reduce the length of unsupported skin panels.

In this section, these elements are implemented on the full scale hingeless control surface which has a span of 50cm. The hingeless control surface is manufactured in later stages for comparison with the finite element models and support web placement in manufacturing is harder due to its connection to skins and its sensitivity to the slanting angle. Also absence of support webs is desired to see the working condition of guide-slide assemblies alone. Thus support webs are left out and will be implemented after analyses if needed.

Finite element model features 4051 nodes and is composed of elements shown in Table 4.1. Mesh seeds are used to create conforming meshes between structural elements and variable element sizes are used. Guide-slide assembly parts and touching skins have fine mesh whereas the skin parts which are in between guide slide assemblies have coarse mesh. This variable mesh size is used to have faster analysis results and to have better accuracy in the regions where contact occurs. Also MPCs are used to model the actuation force application point. Finite element model is shown in Figure 4.1 and in order to see the guide-slide assemblies' upper skin and rear spar is removed from view and shown in Figure 4.2.

Table 4.1: Element Types and Numbers for Hingeless Control Surface Finite Element Model

<b>Element Type</b>	<b>Number Used in Model</b>
QUAD4 Shell	3462
RBE2 MPC	2

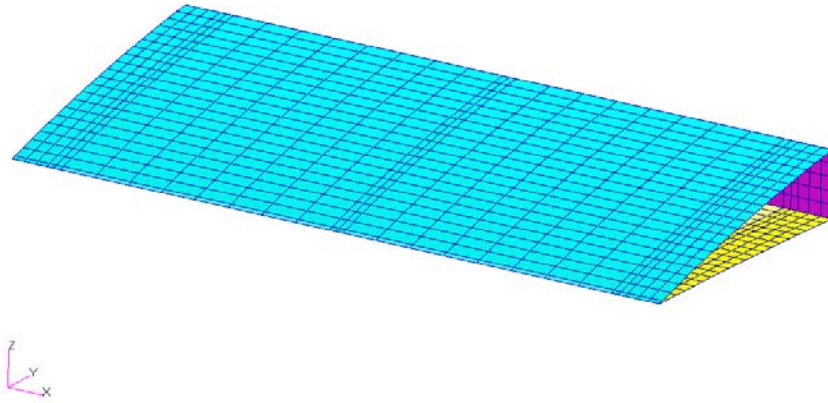


Figure 4.1: Finite Element Model of Hingeless Control Surface

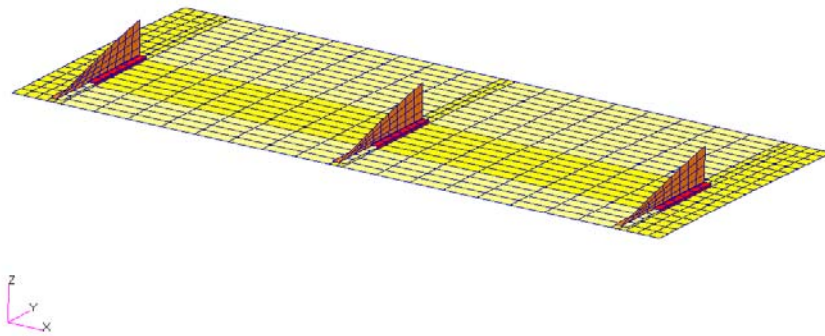


Figure 4.2: Finite Element Model of Hingeless Control Surface (Upper Skin & Rear Spar Removed)

The model features three guide-slide assemblies which have the same geometric and structural properties, it has 10cm track length and material used for every component is 0.635mm thick Aluminum 2024-T3. The guide-slide assembly in the middle is not actuated by a force; it follows the movement of other guide-slide assemblies on which actuation forces are applied. The reason why it is not actuated is that two actuators (servos) for one hingeless control surface should be enough in order to keep up with conventional control surfaces of similar sizes. The guide-slide assemblies on the sides are placed 3cm away from edges in spanwise direction and the other one is in the middle of the span of the hingeless control surface.

Finite element model is analyzed with different actuation forcing. First, two guide-slide assemblies near the edges are actuated with forces of same magnitude and same direction, this forcing is defined as constant actuation. This forcing causes the hingeless control surface to create a positive or negative camber change which is nearly constant throughout the span. However as the guide-slide assembly in the middle is not actuated, it doesn't follow the movement quite enough in some cases, making an uneven camber distribution along the span of the hingeless control surface. This behavior is shown in Figure 4.3 where 20N constant actuation in positive chordwise direction is applied. In order to get more trailing edge deflection, magnitude of the action forces are increased which results in more disparities in the spanwise camber distribution of the hingeless control surface as seen in Figure 4.4 for 50N constant actuation in positive chordwise direction.

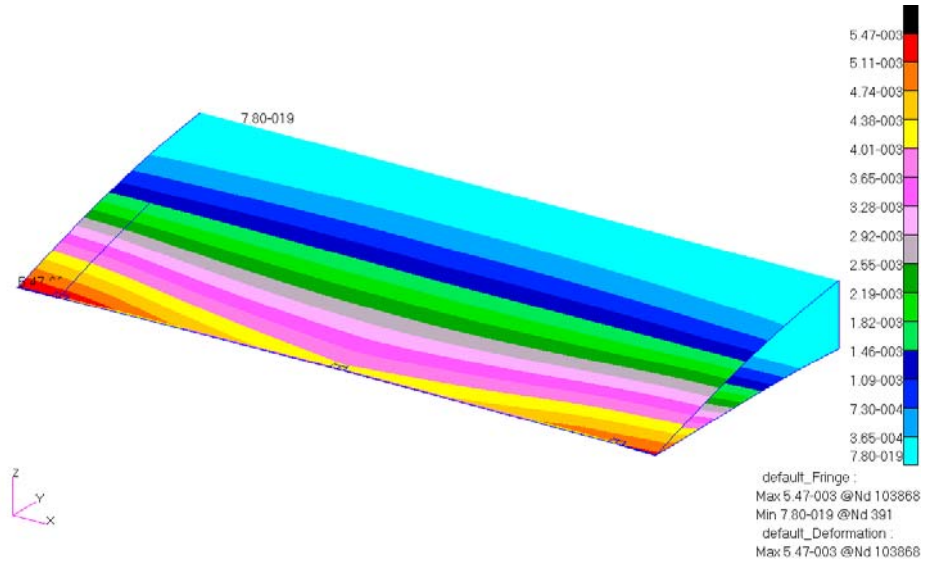


Figure 4.3: Displacement of the Hingeless Control Surface with 20N Constant Actuation in Positive Chordwise Direction [m]

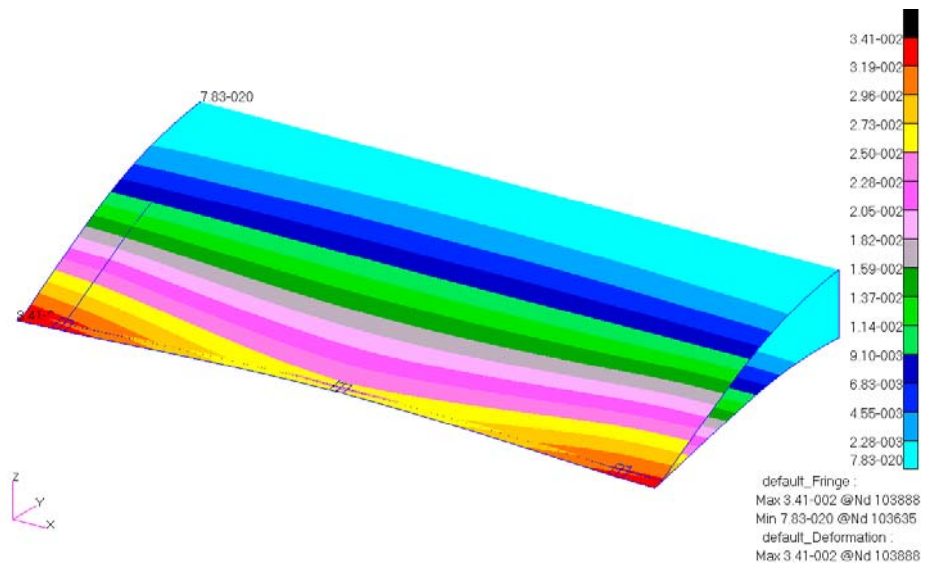


Figure 4.4: Displacement of the Hingeless Control Surface with 50N Constant Actuation in Positive Chordwise Direction [m]

The analyses are done within the operating range of the hingeless control surface, which does not exceed trailing edge deflections about 3.5cm which translates to 10° of conventional control surface movement. Maximum actuation forcing is selected to be 50N per guide-slide assembly to be compatible with this limit.

Stresses developed in the hingeless control surface parts are investigated for the maximum trailing edge deflections with 50N constant actuation. Figure 4.5 and Figure 4.6 show the Cauchy stress distribution of the system for positive and negative camber changes. The maximum stress encountered is below the yield strength of the material used for maximum loading case. Therefore, the material is within linear elastic region, which confirms the material definition assumption.

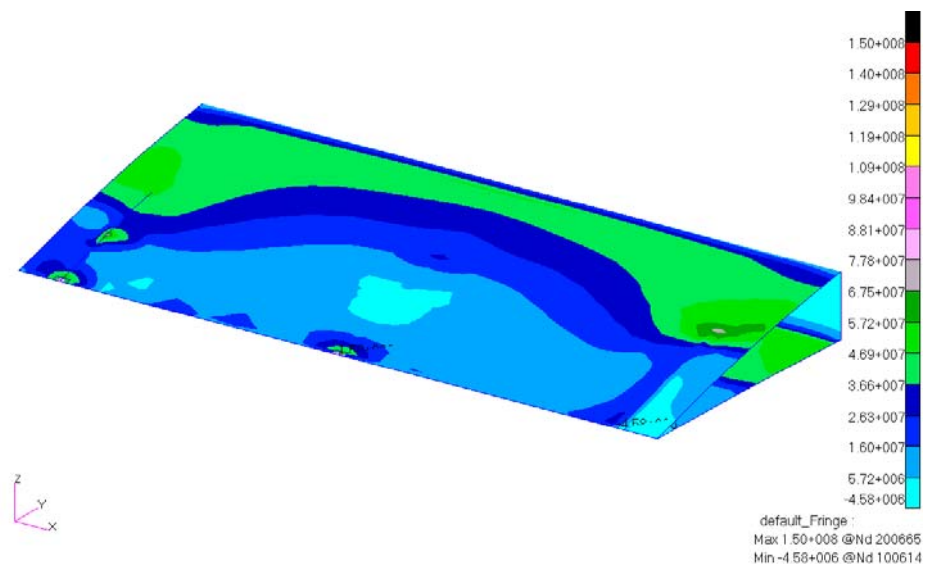


Figure 4.5: Cauchy Stress Distribution for 50N Constant Actuation in Positive Chordwise Direction

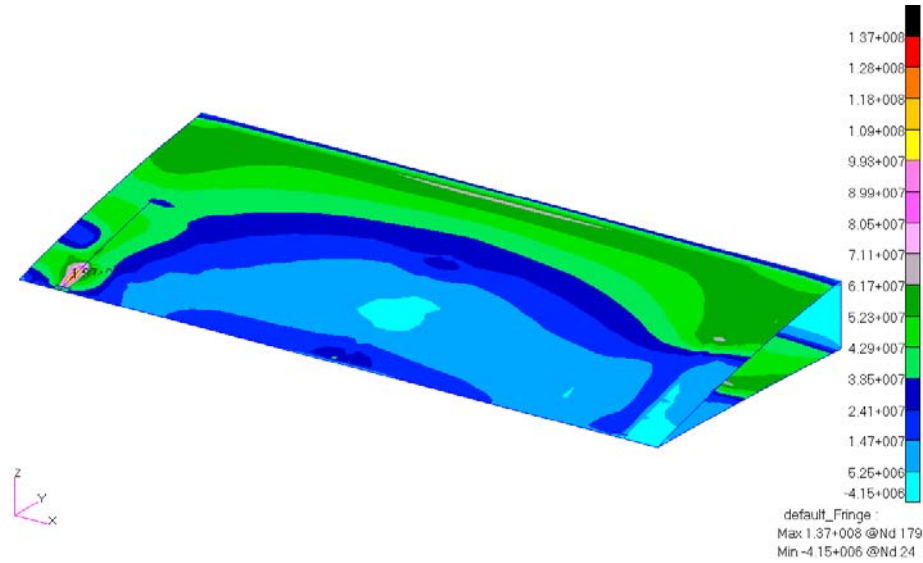


Figure 4.6: Cauchy Stress Distribution for 50N Constant Actuation in Negative Chordwise Direction

One thing to note is that since the solution is nonlinear, even though the loading is same for the two actuated guide-slide assemblies, the solution converges with one of them having more stress values than the other one. This is due to nonlinear solution's nature of having more than one solution for the system. This has minimal effect on the displacements of the system since the solution is displacement based for convergence but has some significant effects on stresses.

Guide-slide assemblies in the hingeless control surface can be actuated with different magnitude forces. This actuation causes a spanwise camber distribution leading to a twisting effect in the control surface. An example application of twisting effects is shown in Figure 4.7 and Figure 4.8 where one guide-slide assembly is actuated with 50N in positive chordwise direction and other guide-slide assembly is actuated with 20N in positive chordwise direction.

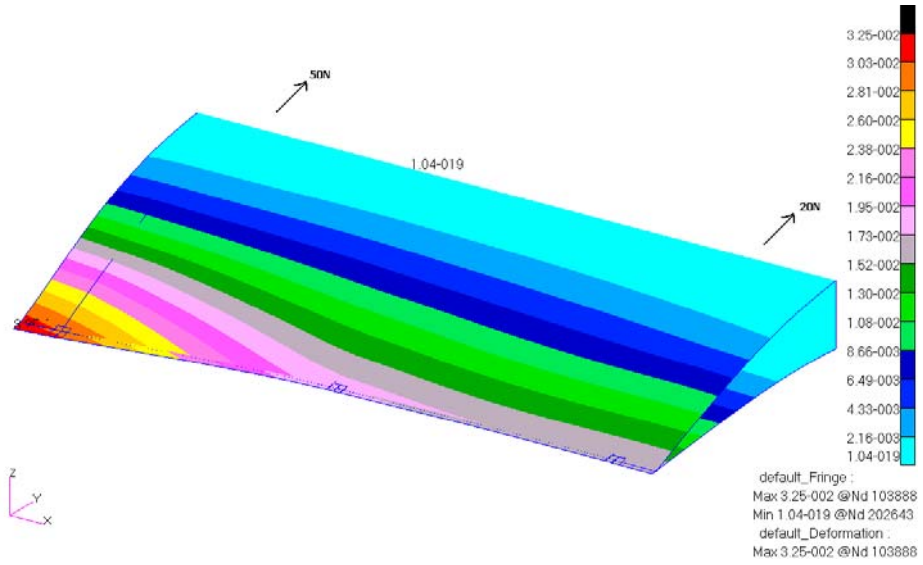


Figure 4.7: Displacement of the Hingeless Control Surface with 50N & 20N Positive Chordwise Actuation [m]

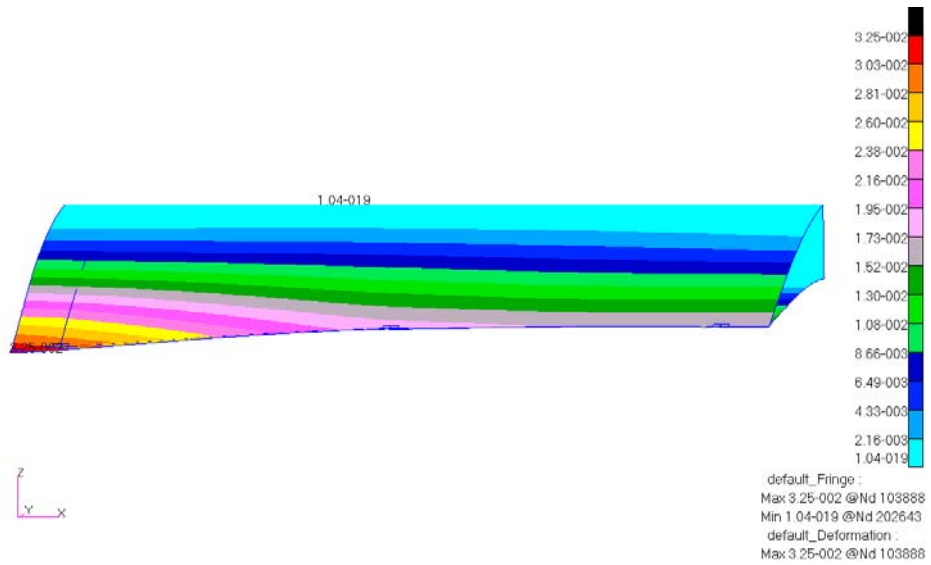


Figure 4.8: Displacement of the Hingeless Control Surface with 50N & 20N Positive Chordwise Actuation [m] (From Trailing Edge)

The twisting effect can also be achieved with actuation forces in different directions for each guide-slide assembly. This actuation is shown in Figure 4.9 for the case one guide-slide assembly is actuated in positive chordwise direction while the other is actuated in negative chordwise direction with 50N actuation forces. While this twisting doesn't create too much stress in the structure, shown in Figure 4.10, the actuation systems namely the servos and push rods that will transmit the load would be in high loading. The critical component in the actuation is the push rods connection to the servos which are mostly hard plastics that have lower strength compared to aluminum used in the structure, so this kind of twisting shape is not a desirable motion for the hingeless control surface.

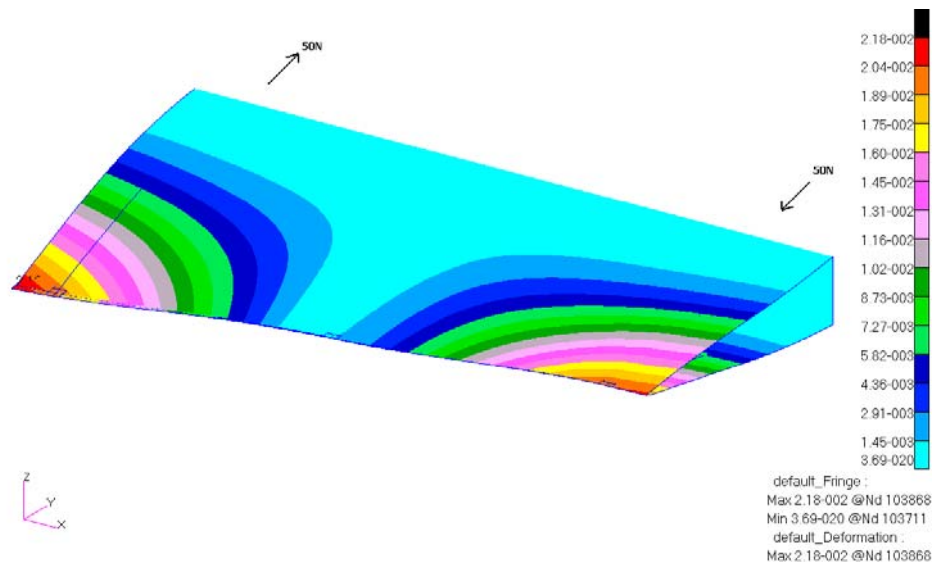


Figure 4.9: Displacement of the Hingeless Control Surface with 50N Positive Chordwise & 50N Negative Chordwise Actuation [m]

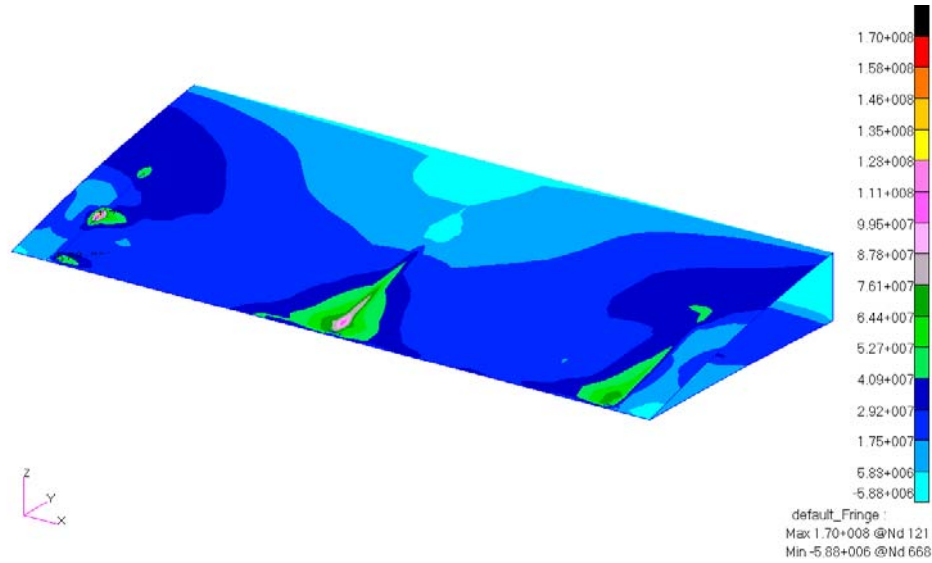


Figure 4.10: Cauchy Stress Distribution of the Hingeless Control Surface with 50N Positive Chordwise & 50N Negative Chordwise Actuation [Pa]

In order to normalize spanwise camber distribution, some changes are done to the model to have same trailing edge deflection throughout the span of the hingeless control surface. The problem having discontinuous camber distribution arises from the middle guide-slide assembly not being actuated so that it may not follow the global motion. Then to have a more controlled distribution a spar-like structure that is connecting the cutout ribs are added to hingeless control surface, which is called as control spar. It allows the middle guide-slide assembly to follow the movement of the outer ones with better precision. Figure 4.11 shows the finite element model including the control spar. Control spar's dimensions are selected to be 42cm x 1cm and it is made of 0.8mm thick Aluminum 2024-T3. It is connected to every cutout rib rigidly.

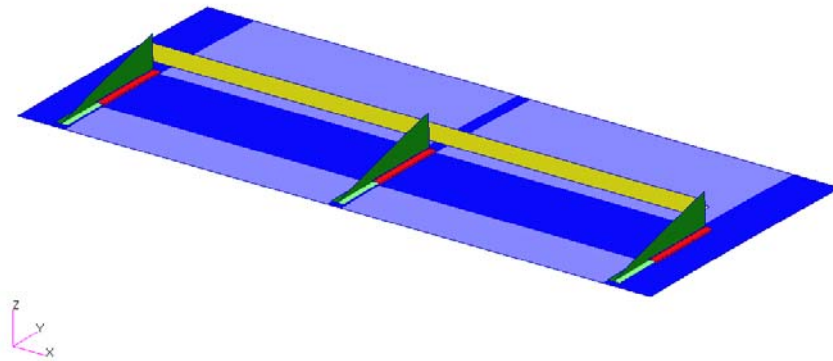


Figure 4.11: Finite Element Model of the Hingeless Control Surface with Control Spar (Upper Skin & Rear Spar Removed)

Deformation of the hingeless control surface with control spar is shown in Figure 4.12 for 50N positive chordwise actuation and in Figure 4.13 for 50N negative chordwise actuation. It is clear that the middle guide-slide assembly follows the movement of the actuated ones and same camber distribution is achieved through the span. Some of the actuation energy is transmitted to middle guide-slide assembly through control spar thus maximum trailing edge deflection with the same loading is lower compared to the model without control spar. Cauchy stress distribution of the system with same loading is shown in Figure 4.14 and it can be seen that stress levels do not change significantly compared with the model without control spar for the same actuation forcing.

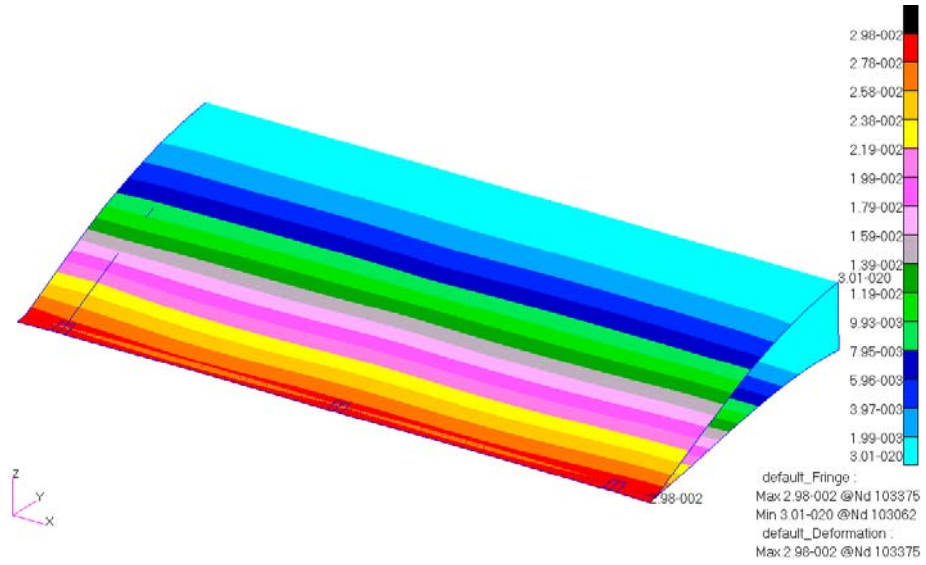


Figure 4.12: Displacement of the Hingeless Control Surface with 50N Positive Chordwise Actuation [m] (Model with Control Spar)

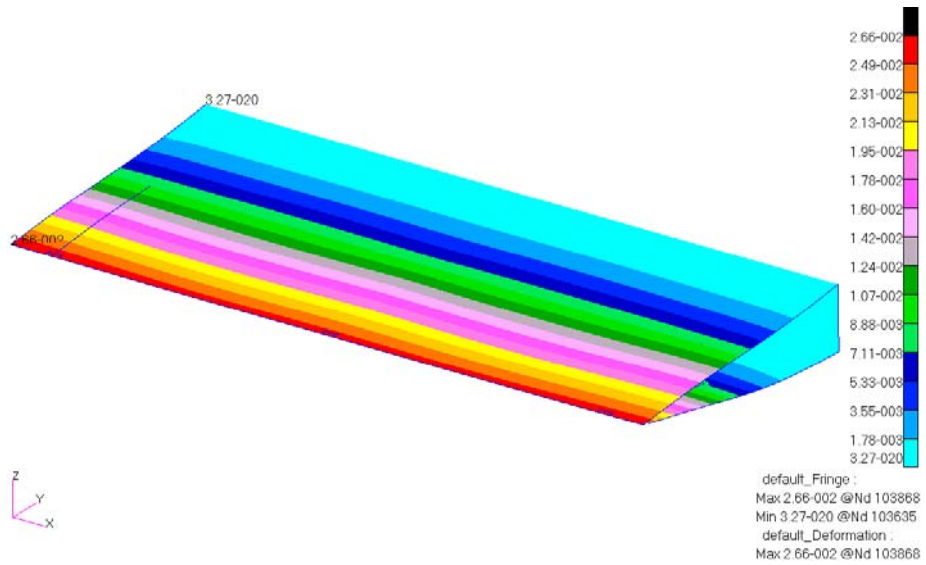


Figure 4.13: Displacement of the Hingeless Control Surface with 50N Negative Chordwise Actuation [m] (Model with Control Spar)

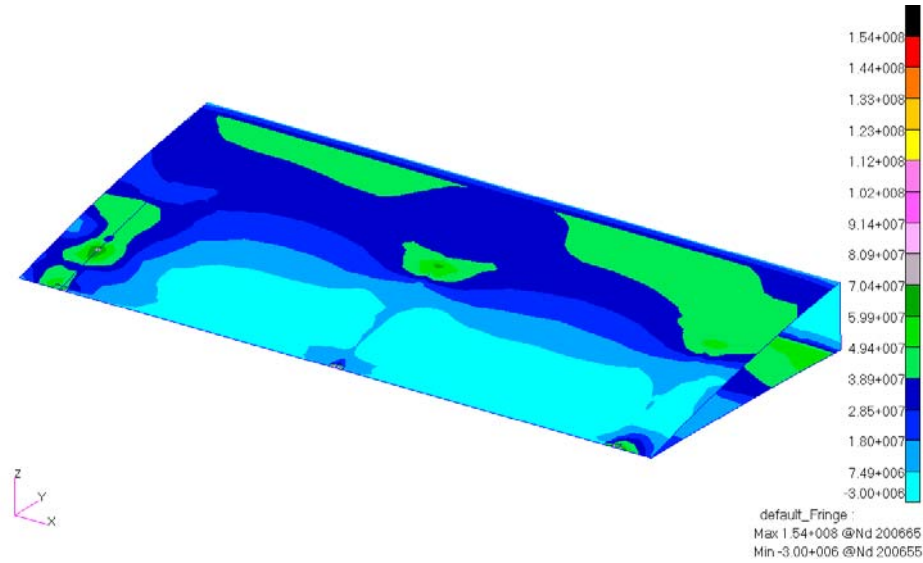


Figure 4.14: Cauchy Stress Distribution of the Hingeless Control Surface with 50N Positive Chordwise Actuation [Pa] (Model with Control Spar)

### 4.3 Manufacture of the Full Scale Hingeless Control Surface

Hingeless control surface and the torque-box portion holding the control surface are manufactured as a prototype test model. Torque box section and the ribs where the servos are connected are designed by Levent Ünlüsoy [1].

In order to have compatibility with the hingeless control surface design introduced in previous parts of the dissertation, structural parts are manufactured from Aluminum 2024-T3 within the allowable thickness limits. Track and cutout rib of the guide-slide assemblies are shown in Figure 4.15 and Figure 4.16, respectively. Track length of 10cm is used and the edge of the track which will be in contact with upper skin is trimmed with a slight angle for smoother contact. Also cutout rib edges are trimmed for the same reason.



Figure 4.15: Track of the Guide-Slide Assembly



Figure 4.16: Cutout Rib of the Guide-Slide Assembly

Figure 4.17 shows the guide-slide assembly connected to lower skin of the hingeless control surface. Flexible push rod that is used for actuation is also shown in the figure connected to cutout rib. Other side of push rod which is connected to servo is shown in Figure 4.18.

There are some design changes in the hingeless control surface model that are enforced by the manufacturing process and the design of torque box. This is mainly due to the rib placement in the torque box section of the wing which limits the servo positions. In order to comply with the torque box design, guide-slide assemblies are placed 10cm away from edges of the control surface in spanwise direction. Also the middle guide-slide assembly is not used in the manufactured model.

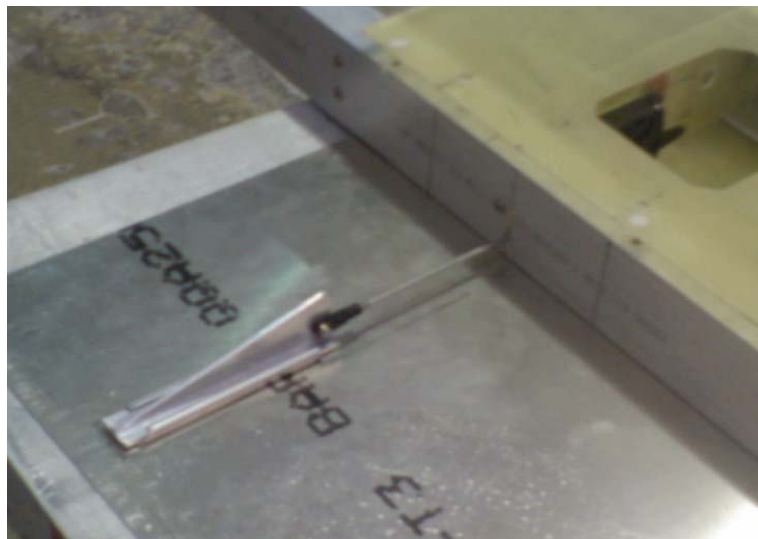


Figure 4.17: Guide-Slide Assembly Attached to Lower Skin, Push Rod Connected to Cutout Rib

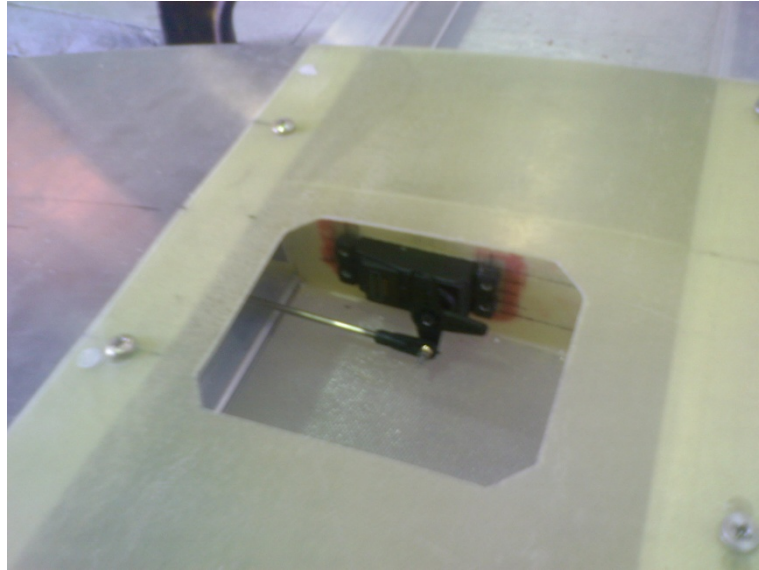


Figure 4.18: Servo Connection

The hingeless control surface is fixed using spar extensions and tested with various servo actions. In constant actuation with positive and negative chordwise directions, trailing edge deflection of 4cm is observed for both directions using full servo power settings. Figure 4.19 shows the hingeless control surface in constant positive chordwise actuation and Figure 4.20 shows the constant negative chordwise actuation. Also twisting loads are applied to the hingeless control surface by applying different magnitude actuation to guide-slide assemblies. Figure 4.21 and Figure 4.22 show an example twisting actuation of the hingeless control surface. In order not to damage servo connections, opposite direction actuation loads are not applied.



Figure 4.19: Hingeless Control Surface with Constant Positive Chordwise Actuation



Figure 4.20: Hingeless Control Surface with Constant Negative Chordwise Actuation

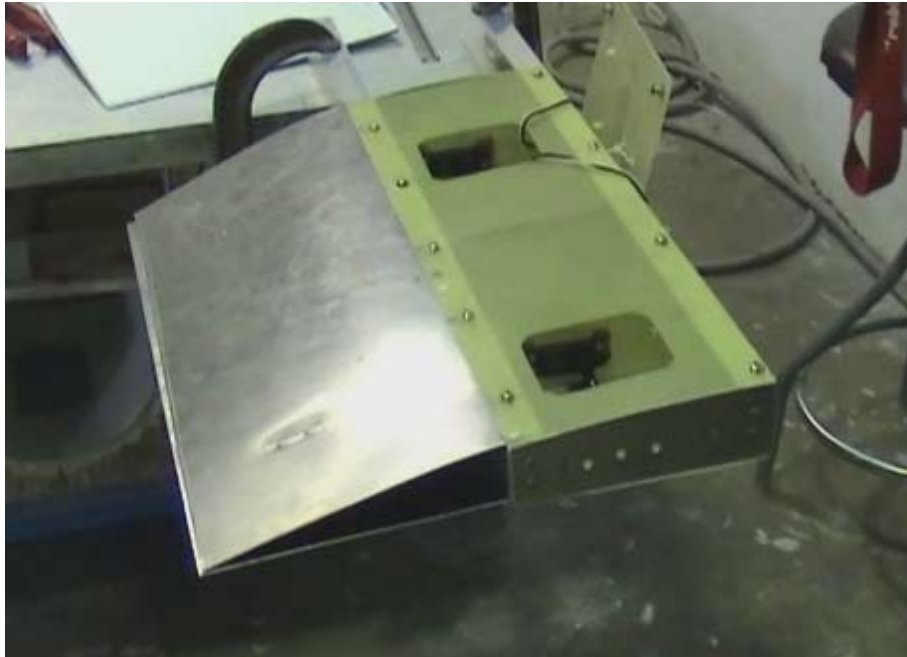


Figure 4.21: Hingeless Control Surface with Twisting Actuation



Figure 4.22: Hingeless Control Surface with Twisting Actuation (From Trailing Edge)

#### 4.4 Analysis of the Adaptive Camber Wing

The changes introduced with the manufacture of hingeless control surface are incorporated into finite element models. Thicknesses of the inner elements like track and cutout rib were updated to match the actual manufactured parts. Also hingeless control surface span is shortened by cutting 0.5cm from both sides so that if any warping occurs contact with the wing can be avoided. Therefore further analyses are based on hingeless control surfaces having 49cm span and 20cm chord lengths. The placement of guide-slide assemblies are based on the manufactured model. Figure 4.23 shows the finite element model of the hingeless control surface with upper skin removed for better visualization of guide-slide assemblies.

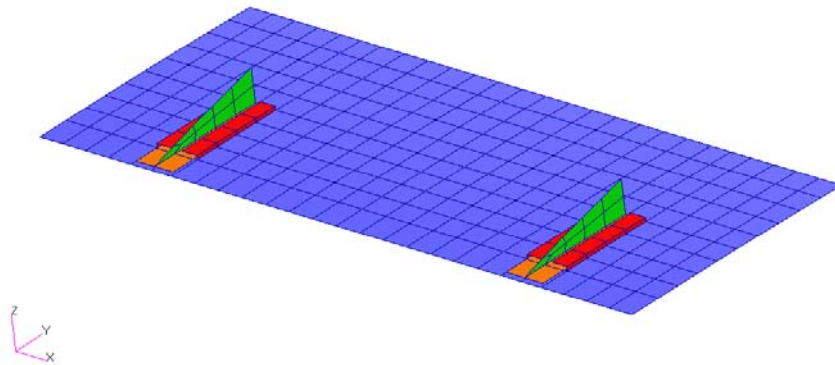


Figure 4.23: Finite Element Model of the Hingeless Control Surface (Upper Skin Removed)

Structural analyses of the hingeless control surfaces are done when they are mounted on the wing. Figure 4.24 shows the adaptive camber finite element model, which features hingeless control surfaces. Properties of the model are

presented in Table 4.2. The wing is fixed in all degrees of freedom through the spar extensions. The inner hingeless control surface works like a flap that changes the overall lift of the wing while the outer one works like an aileron which changes the rolling moment of the wing by changing lift distribution.

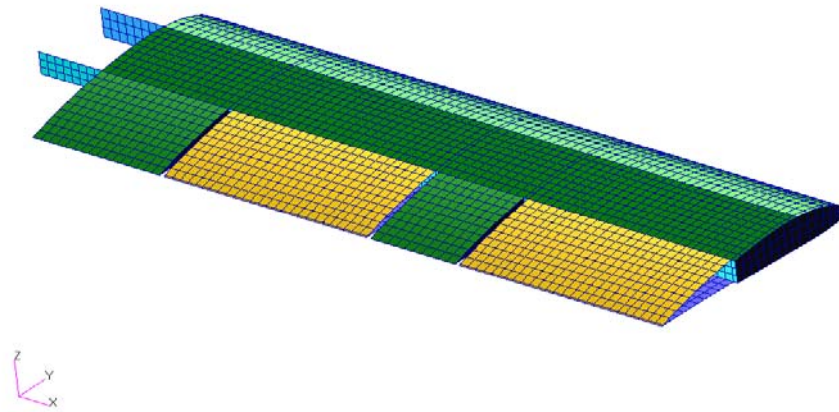


Figure 4.24: Finite Element Model of the Adaptive Camber Wing

Table 4.2: Element Types and Numbers Used in the Adaptive Camber Wing Finite Element Model

Element Type	Number Used in Model
QUAD4 Shell	5489
RBE2 MPC	8

In order to prevent the net moment effect of actuation forces in the wing, the actuation reactions are also modeled as forces having the same magnitude but opposite directions. These reactions are placed on the rear spar having the same line of action of actuation forces. These reaction forces represent the forces that are required to hold the servo stationary during actuation.

The main advantage of having two separate hingeless control surfaces is that they can morph independent of each other. This behavior is presented in Figure 4.25 where the outer hingeless control surface is actuated with different forces while the inner one is kept still. Also the stress distribution of this case, shown in Figure 4.27, dictates that the morphing of the hingeless control surface doesn't impose any forces in the torque box of the wing and other control surface.

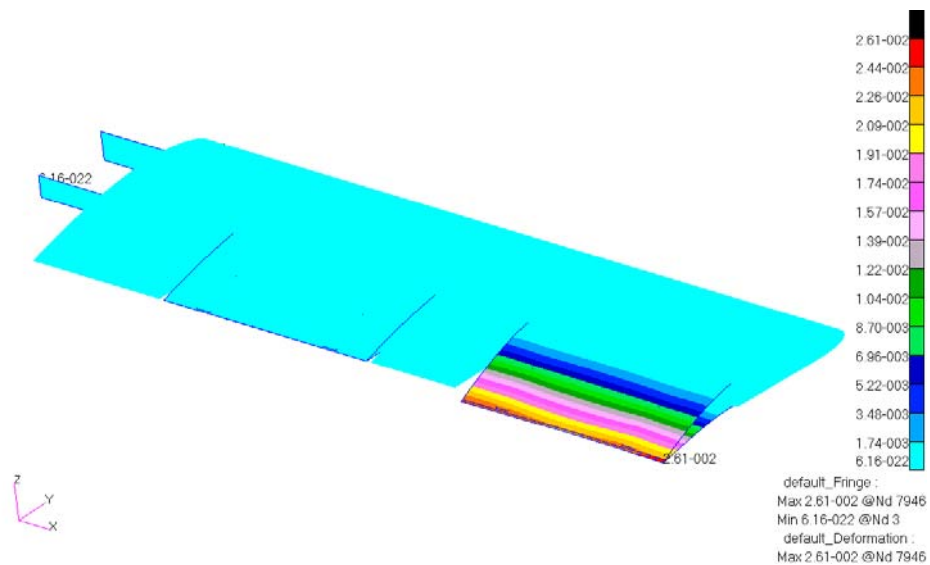


Figure 4.25: Displacement of the Adaptive Camber Wing, Only Outer Hingeless Control Surface Actuated in Positive Chordwise Direction [m]

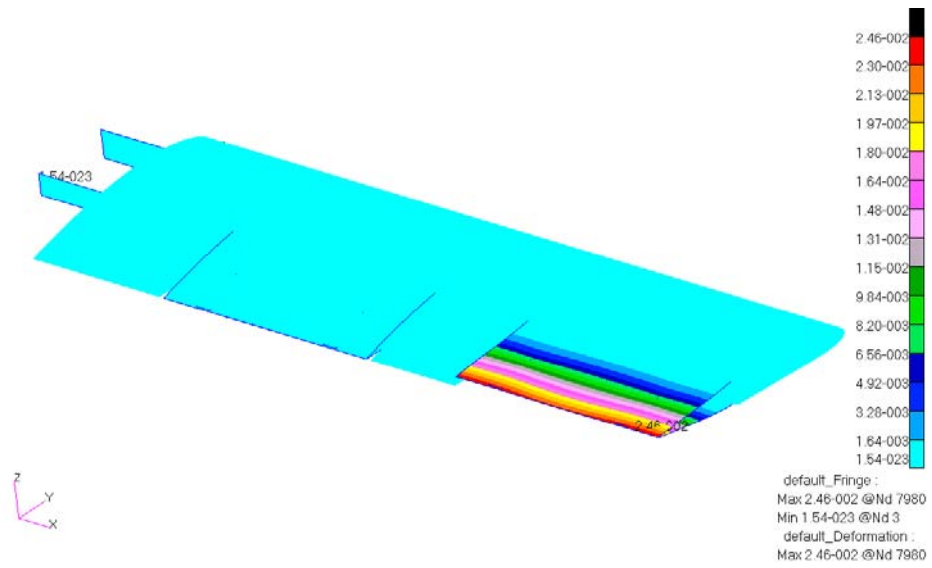


Figure 4.26: Displacement of the Adaptive Camber Wing, Only Outer Hingeless Control Surface Actuated in Negative Chordwise Direction [m]

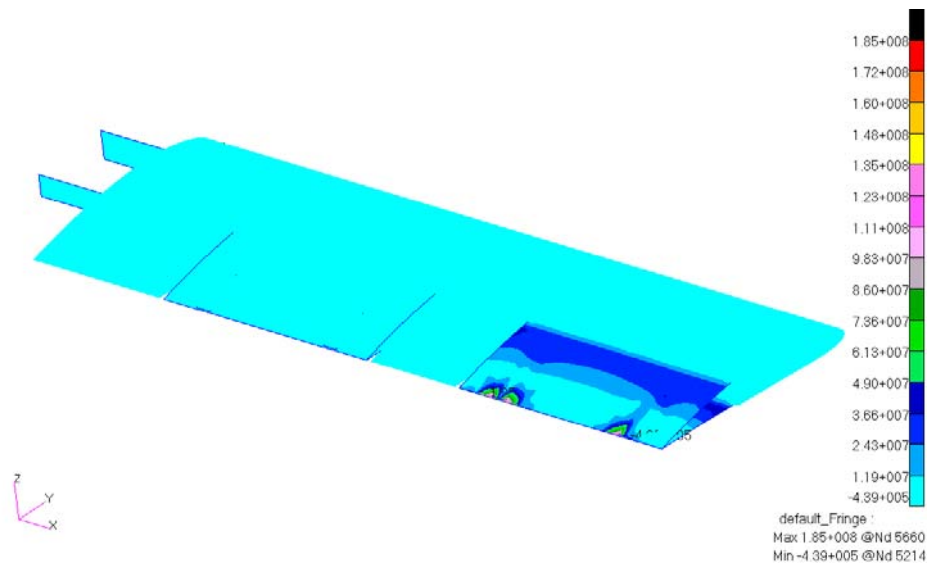


Figure 4.27: Cauchy Stress Distribution of the Adaptive Camber Wing, Only Outer Hingeless Control Surface Actuated in Positive Chordwise Direction [Pa]

As control surfaces can be actuated without imposing any stress on each other and other parts of the wing; any morphed shape of the hingeless control surfaces to suit the maneuver can be achieved within the operating limit. Figure 4.28 shows an example where all guide-slide assemblies are actuated with same magnitude same directional forces. Having opposite directional actuation for hingeless control surfaces one can increase camber while other is decreasing camber, where an example is shown in Figure 4.29.

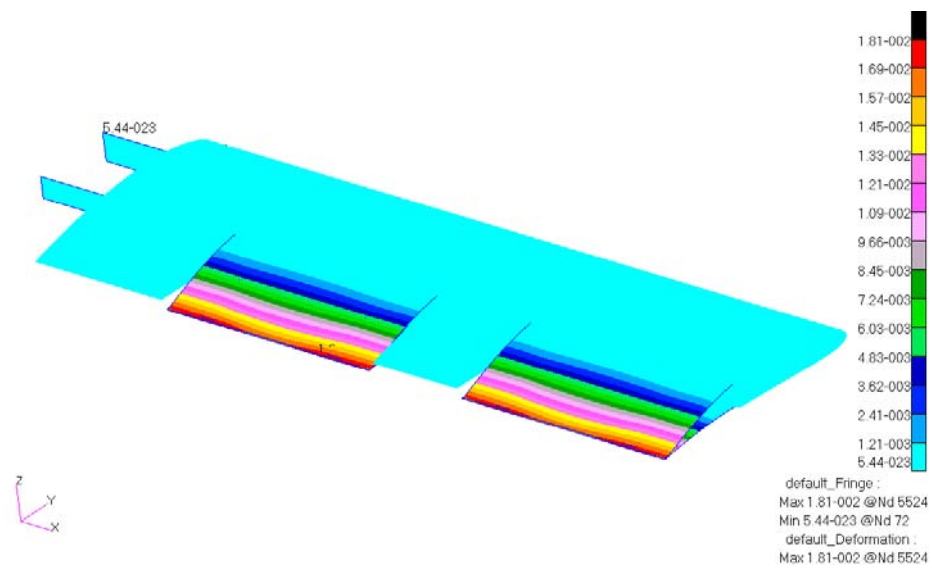


Figure 4.28: Displacement of the Adaptive Camber Wing, All Hingeless Control Surfaces Actuated in Positive Chordwise Direction [m]

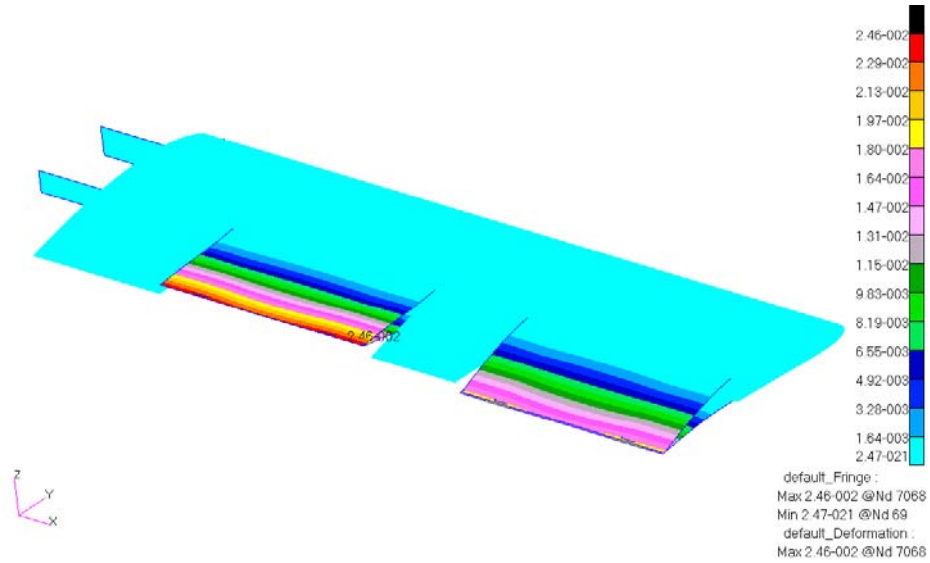


Figure 4.29: Displacement of the Adaptive Camber Wing, Inner Hingeless Control Surface Actuated in Negative Chordwise Direction, Outer Hingeless Control Surface Actuated in Positive Chordwise Direction [m]

It is also possible to apply different magnitude actuation to guide-slide assemblies of a hingeless control surface to create a twist. The outer control surface having 20N and 50N actuation in guide-slide assemblies is shown in Figure 4.30; related Cauchy stress distribution is presented in Figure 4.31. If needed the hingeless control surfaces can be actuated with twisting loads. However the effect of having a twisting actuation on the servos should be checked for the real life application.

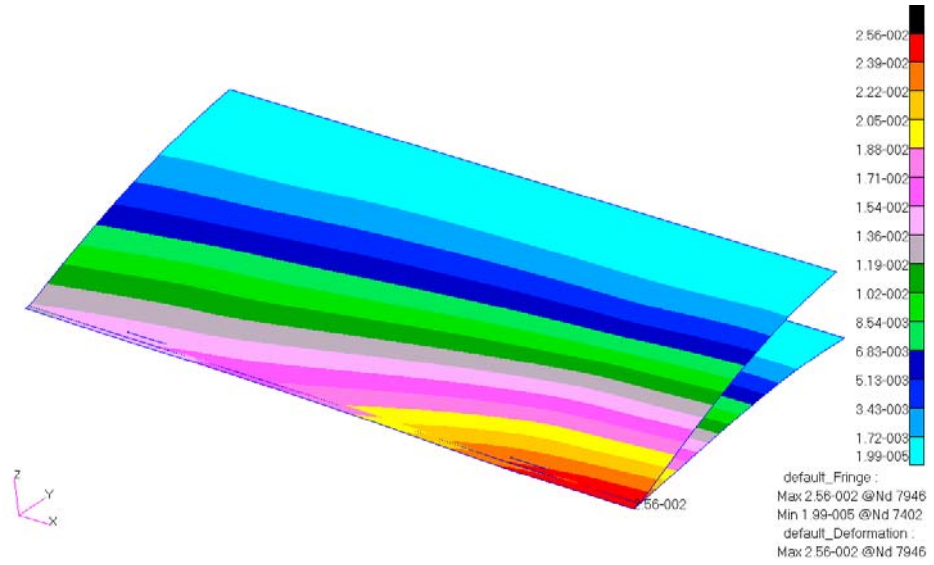


Figure 4.30: Displacement of the Outer Hingeless Control Surface Actuated with Twisting Actuation of 20N & 50N [m]

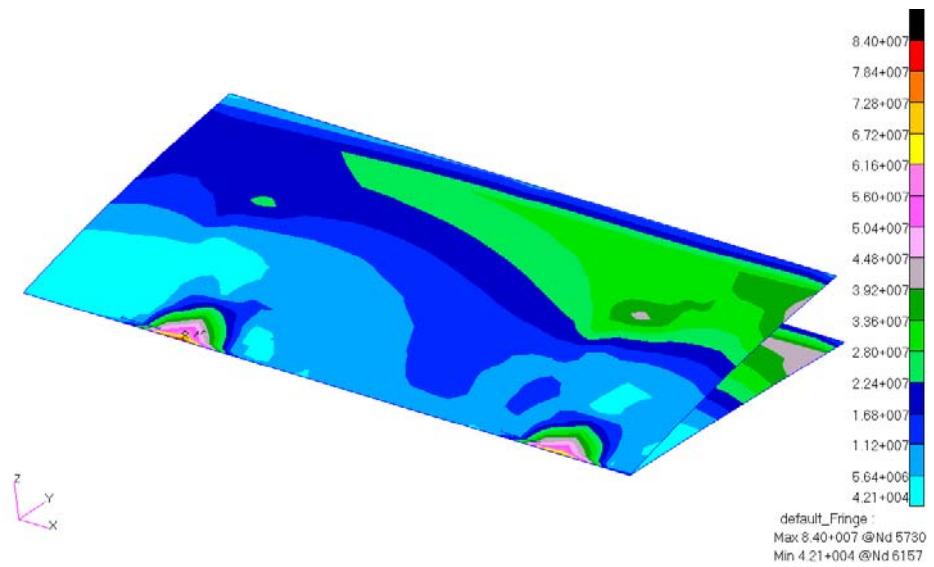


Figure 4.31: Cauchy Stress Distribution of the Outer Hingeless Control Surface Actuated with Twisting Actuation of 20N & 50N [Pa]

## **4.5 Modal Analysis of Adaptive Camber Wing**

This section presents the modal analysis of the adaptive camber wing. Theoretical analyses are done with finite element solutions. Experimental modal analysis of the wing is performed and compared with finite element analysis results. Global modes of the adaptive camber wing will be emphasized in the study. Local modes associated with hingeless control surfaces and other parts are not presented in detail. Also in-plane motion of the wing is not analyzed within the scope of study.

### **4.5.1 Finite Element Method Results**

Finite element model of the adaptive camber wing is updated to match the manufacturing stage [1]. The updated model includes servo access seals and tip fairing as well as detailed modeling of corner connection parts and rivets to match the total weight, which is 8148gr. Geometry of the adaptive wing is shown in Figure 4.32. Meshed finite element model is presented in Figure 4.33 and properties of the mesh are given in Table 4.3. In order to be able to model the connection parts, the model has finer mesh compared to models used to analyze hingeless control surface motion.

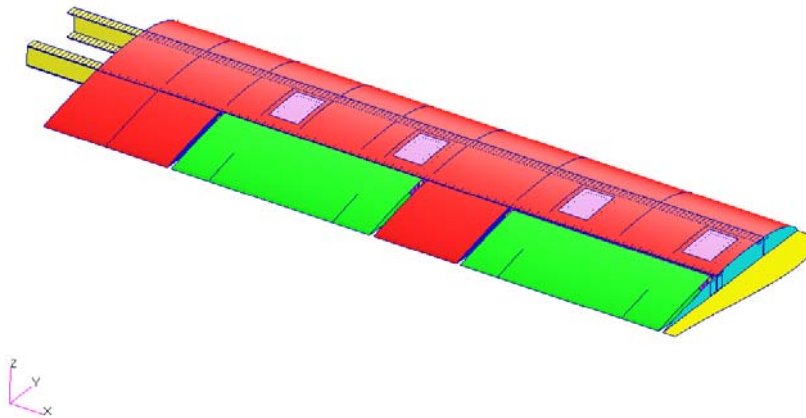


Figure 4.32: Geometry of the Adaptive Camber Wing

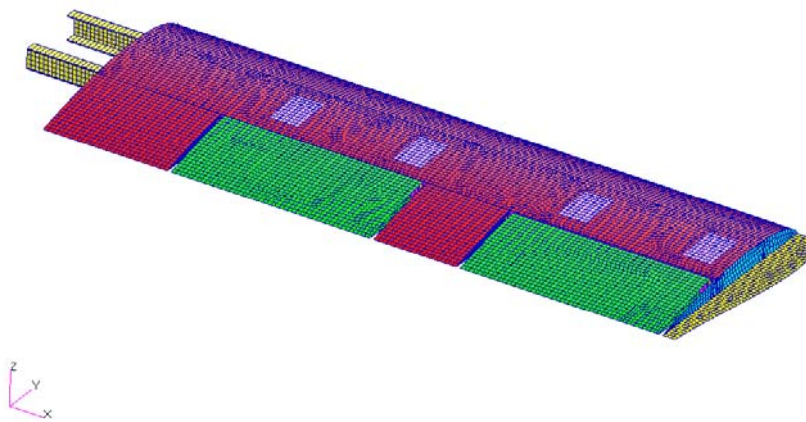


Figure 4.33: Detailed Finite Element Model of the Adaptive Camber Wing

Table 4.3: Element Types and Numbers Used in Adaptive Camber Wing Modal Analysis Model

<b>Element Type</b>	<b>Number Used in Model</b>
QUAD4 Shell	21370
RBE2 MPC	1090

Modal analysis of the adaptive camber wing is done with Normal Mode Analysis (Solution 103) of MSC<sup>®</sup> NASTRAN. Global bending and torsion modes of the adaptive camber wing are presented in Figure 4.34- Figure 4.37. First out-of-plane bending mode shape is shown with and without hingeless control surfaces and tip fairing, for graphical presentation only, as these components mostly have high eigenvectors compared to other parts of the wing and when they are not shown the global mode is easily recognizable. Other mode shapes are only shown with these components hidden. The results are summarized in Table 4.4.

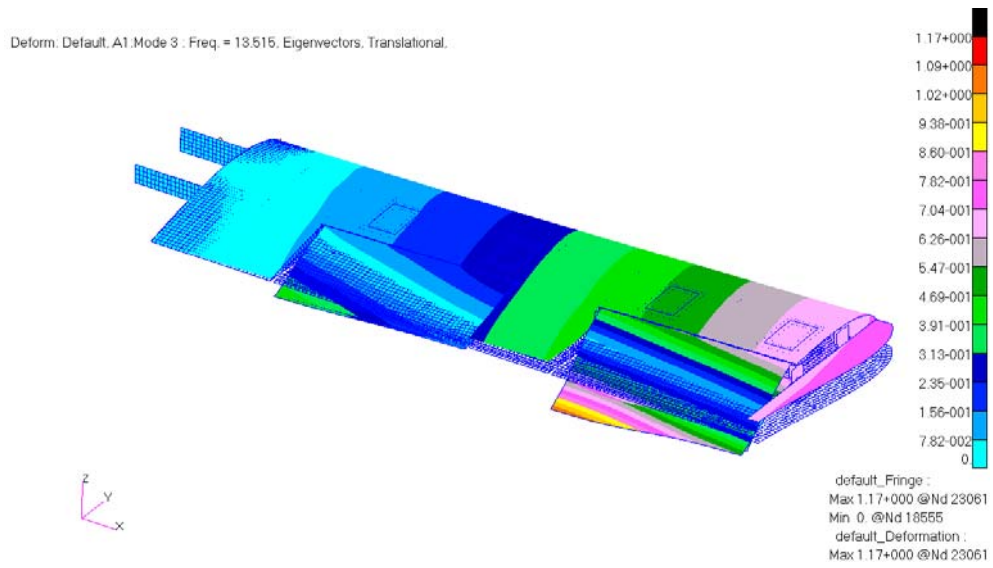


Figure 4.34: Mode Shape of the Adaptive Camber Wing at 13.52 Hz (First Out-of-plane Bending Natural Frequency, Hingeless Control Surfaces and Tip Fairing Shown)

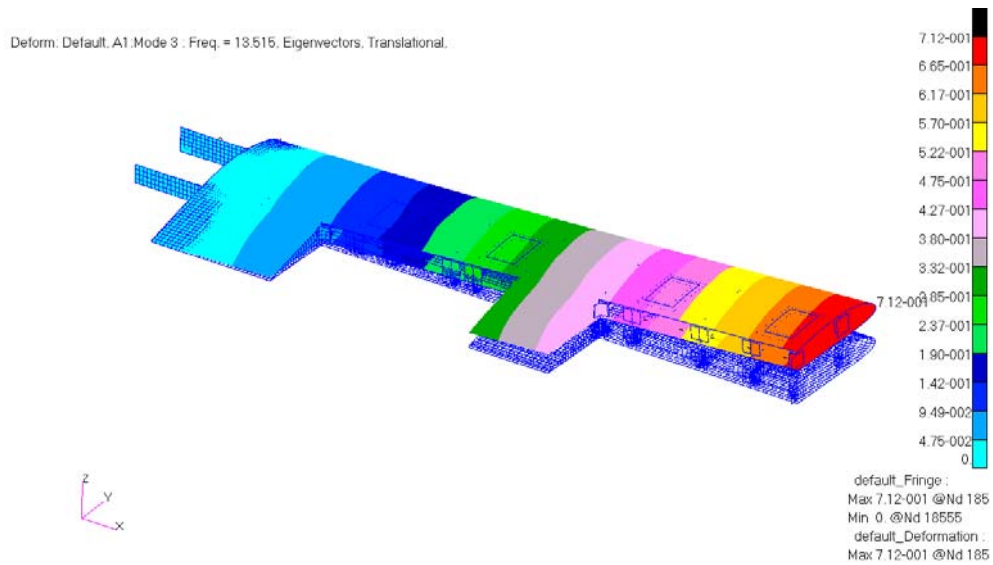


Figure 4.35: Mode Shape of the Adaptive Camber Wing at 13.52 Hz (First Out-of-plane Bending Natural Frequency)

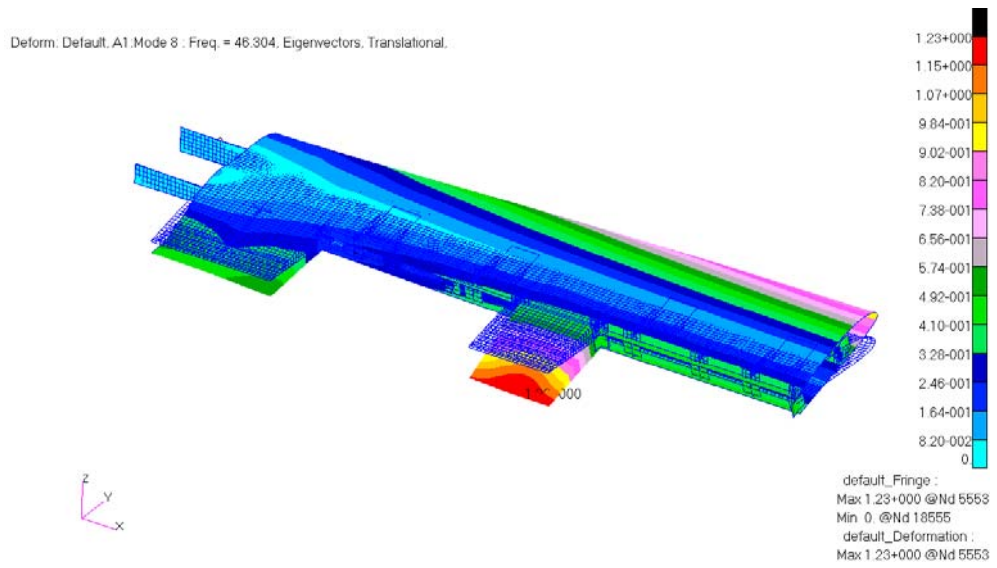


Figure 4.36: Mode Shape of the Adaptive Camber Wing at 46.30 Hz (First Torsional Natural Frequency)

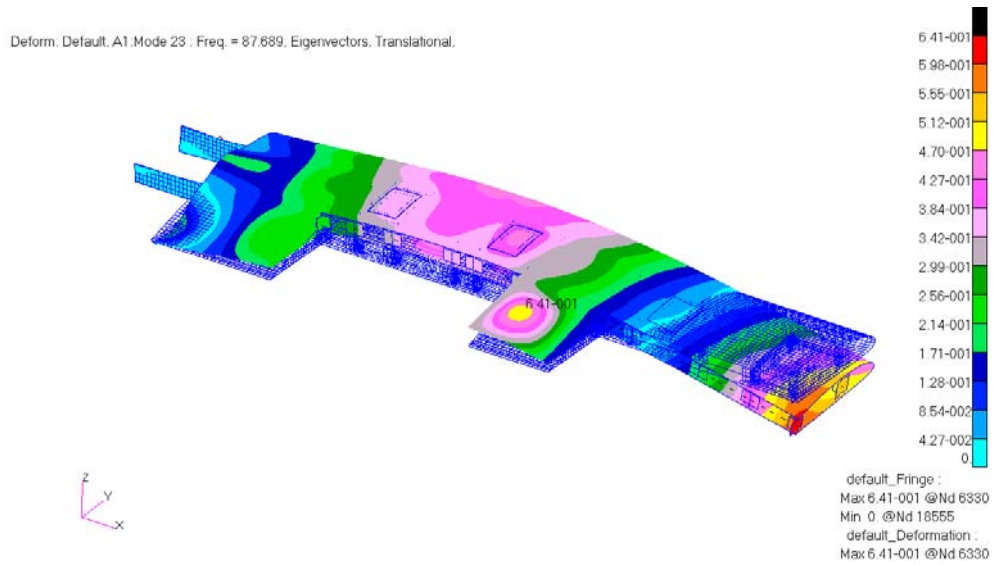


Figure 4.37: Mode Shape of the Adaptive Camber Wing at 87.69 Hz (Second Out-of-plane Bending Natural Frequency)

Table 4.4: Natural Modes and Associated Frequencies (Finite Element Analysis)

<b>Mode Shape</b>	<b>Frequency [Hz]</b>
1. Out-of-plane Bending	13.52
1. Torsion	46.30
2. Out-of-plane Bending	87.69

#### **4.5.2 Experimental Results**

Experimental setup user end is shown in Figure 4.38 and the adaptive camber wing attached to fixture with modal shaker is shown in Figure 4.39. One axis accelerometers are used to measure the acceleration of the wing and modal shaker and impact hammer are used to excite the wing. Figure 4.40 shows the wing torque box geometry definition for the experiments. Nodes 64-67 are used to define boundary conditions and nodes 1-63 are used as excitation points of roving impact hammer. Stationary one axis accelerometers are placed in nodes 10, 29 and 54 in order to get comparative data. Modal shaker is placed under node 5. Measurements on the hingeless control surfaces are done by accelerometers placed on each of them; no excitation is applied on the control surfaces. For the reasons discussed in the finite element results section, mode shapes will be presented only for the torque-box geometry.



Figure 4.38: Analysis Equipment Used in the Experimental Modal Analysis



Figure 4.39: Adaptive Camber Wing Attached to Fixture, Modal Shaker and Accelerometers Attached to the Wing

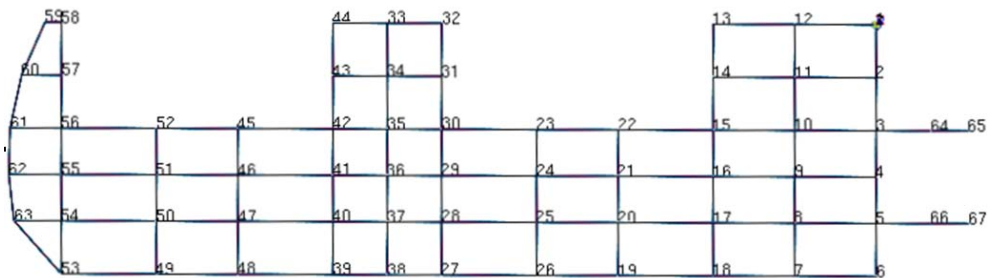


Figure 4.40: Experimental Grid of the Wing Torque-Box

Experimental analysis is done in stages, first the system is excited with white noise and sine sweep to get the general locations of resonant frequencies. These excitations are done by modal shaker with the help of signal generator. The frequency response functions generated by these tests are presented in Figure 4.41 for white noise excitation, Figure 4.42 for sine sweep excitation respectively. These response functions are generated by using the accelerometer in node 54.

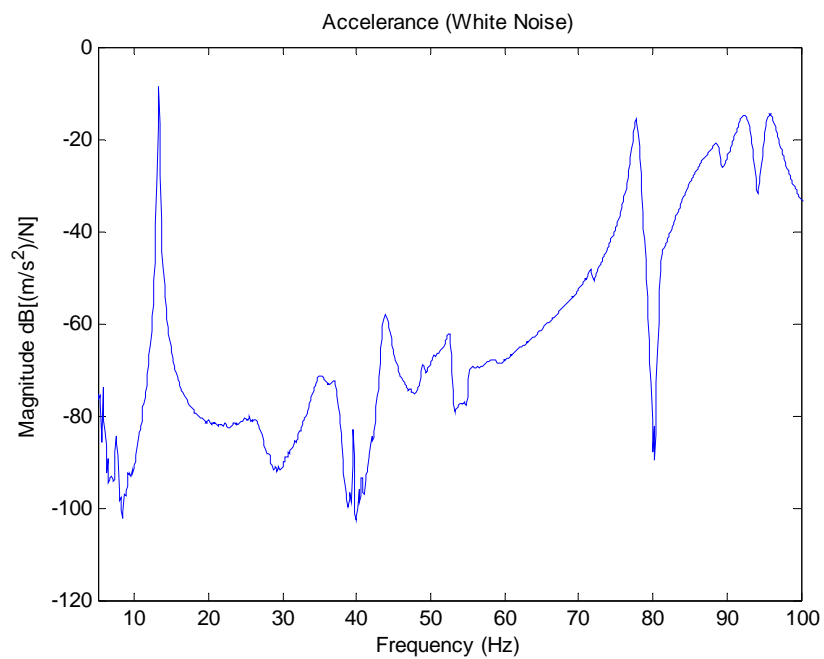


Figure 4.41: Frequency Response Function Between Accelerometer in Node 54 and White Noise Excitation from Node 5

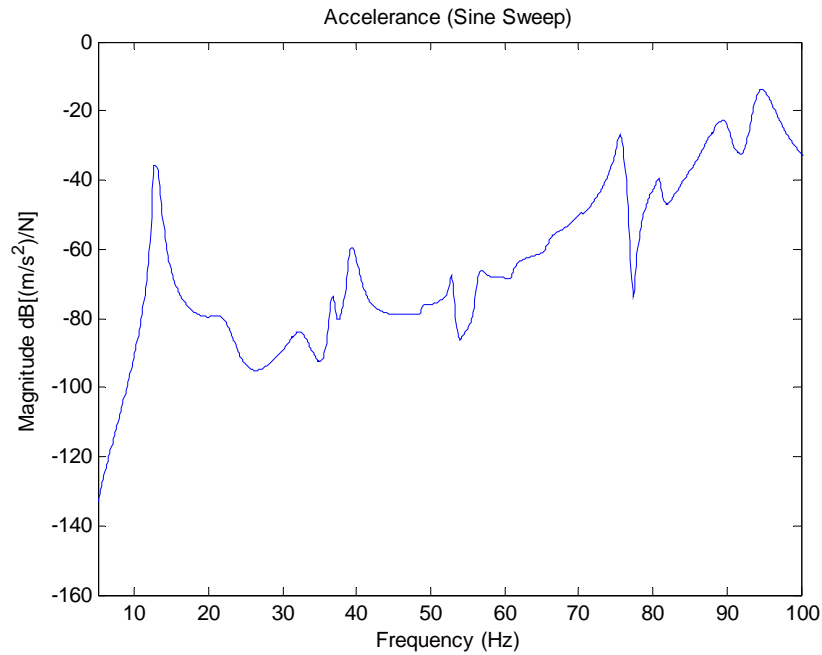


Figure 4.42: Frequency Response Function Between Accelerometer in Node 54 and Sine Sweep Excitation from Node 5

In order to identify the modes, roving impact hammer experiment is conducted. The experimental grid on the torque-box is actuated by impact hammer and frequency response function for each point on the grid is obtained. Frequency response functions obtained from three accelerometers, each having 63 measurements, are shown in Figure 4.43 and their average is shown in Figure 4.44. The mode shapes associated with the resonant frequencies found are plotted by the use of imaginary part of the frequency response data and global modes are identified. Mode shapes for out-of-plane bending modes and torsional modes are presented in Figure 4.45 - Figure 4.47. Other resonant peaks are local modes involving hingeless control surfaces. In the figures horizontal axes are in cm and the vertical axis is normalized for visualization.

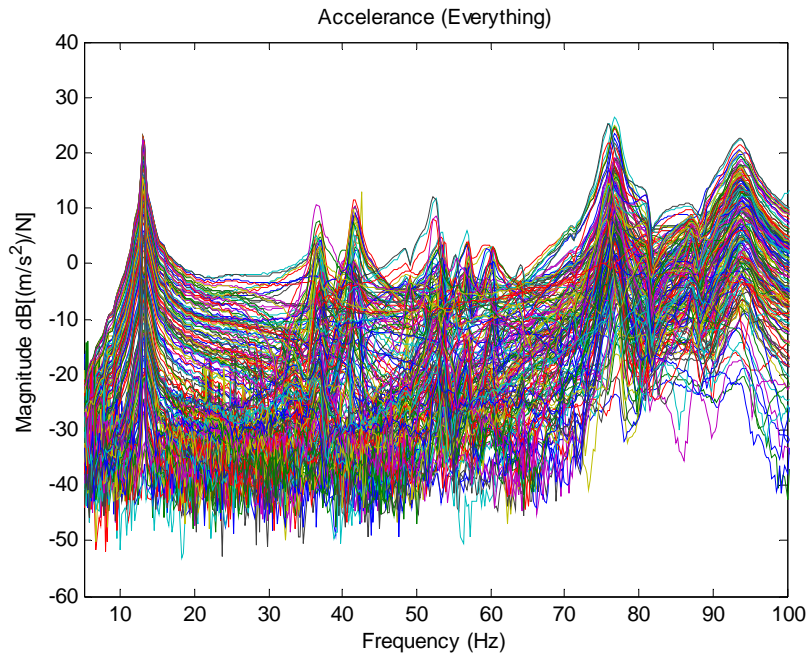


Figure 4.43: Frequency Response Functions of Roving Hammer Measurements

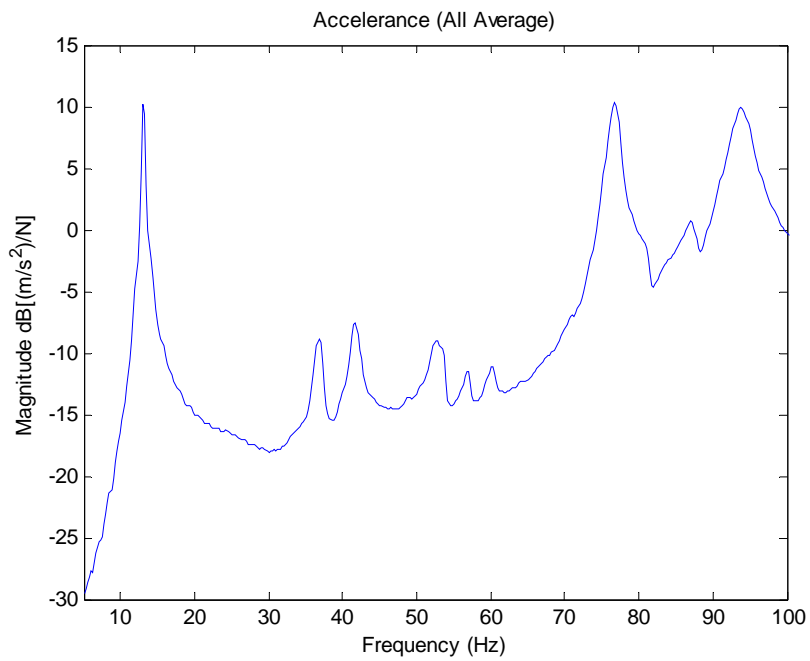


Figure 4.44: Average Frequency Response Function (Roving Hammer)

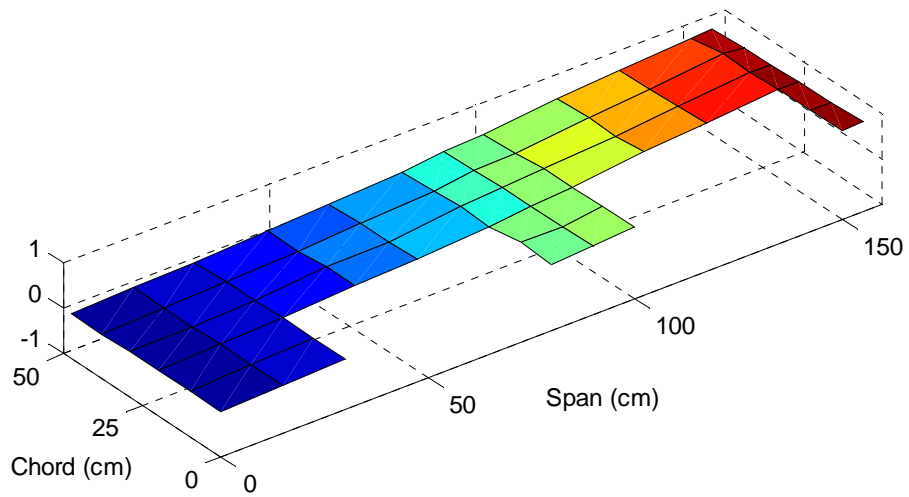


Figure 4.45: Experimental Mode Shape of the Adaptive Camber Wing at 13.00 Hz  
(First Out-of-plane Bending Natural Frequency)

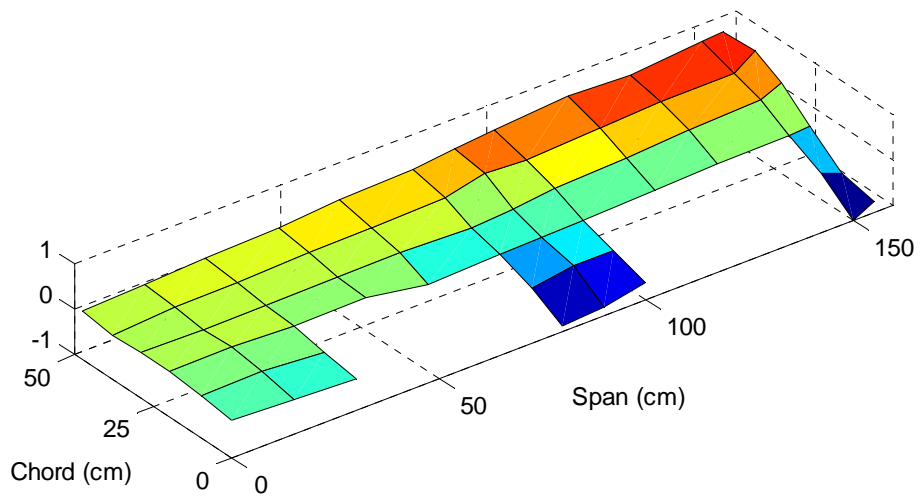


Figure 4.46: Experimental Mode Shape of the Adaptive Camber Wing at 49.00 Hz  
(First Torsional Natural Frequency)

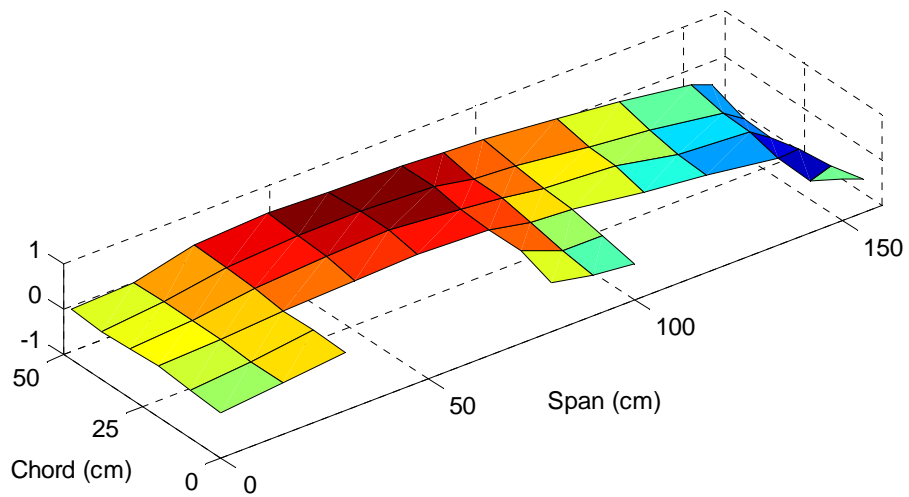


Figure 4.47: Experimental Mode Shape of the Adaptive Camber Wing at 88.75 Hz  
(Second Out-of-plane Bending Natural Frequency)

Table 4.5 shows the comparison of experimental mode shape frequency results for the global modes. Comparison of the experimental results with the finite element model results is presented in Table 4.6. It can be seen that the results are in close agreement.

Table 4.5: Comparison of Experimental Frequencies from Different Types of Excitations for Global Modes of the Adaptive Camber Wing

<b>Mode Shape</b>	<b>White Noise Excitation [Hz]</b>	<b>Sine Sweep Excitation [Hz]</b>	<b>Impact Hammer Excitation [Hz]</b>
1. Out-of-plane Bending	13.25	13.00	13.00
1. Torsional	48.88	49.13	49.00
2. Out-of-plane Bending	88.38	89.13	88.75

Table 4.6: Comparison of Experimental Frequencies with Finite Element Analysis for Global Modes of the Adaptive Camber Wing

<b>Mode Shape</b>	<b>Experimental Impact Hammer Excitation [Hz]</b>	<b>Finite Element Analysis [Hz]</b>	<b>Percentage Difference wrt Experiments</b>
1. Out-of-plane Bending	13.00	13.52	+ 3.84 %
1. Torsional	49.00	46.30	- 5.83 %
2. Out-of-plane Bending	88.75	87.69	- 1.21 %

## **4.6 Conclusions**

In this chapter, the camber morphing concept was implemented on hingeless control surface. Hingeless control surface was analyzed structurally for different camber variations using finite element analysis. The possible use of control spars to control the spanwise camber variation was presented. Different camber morphing capabilities of the hingeless control surface was shown along with the stress values it causes during morphing.

The hingeless control surface was manufactured and it was tested with positive and negative camber changes having constant spanwise camber variation. The manufactured model was also tested with twisting loads.

The hingeless control surface model was updated to match the manufacture changes and tested on the adaptive camber wing with finite element analysis. The model was tested with various actuation loads and displacement and stress results for those cases were presented.

Finally, the modal testing of the adaptive camber wing was done with finite element analysis and compared with experimental results. Global modes of the wing were identified both with finite element results and experimental data.

## **CHAPTER 5**

### **CONCLUSION**

#### **5.1 General Conclusions**

This thesis study aims to present the development of the hingeless control surface to be used in adaptive camber wing. The adaptive camber wing having hingeless control surfaces has been designed, analyzed using finite element analysis and then manufactured for experimental testing.

The first part of the thesis was dedicated to the development of the camber morphing concept and assessment of the concept. The use of semi-open trailing edge which enables skins to flex and have a relative motion that creates the camber change in the section was explained. Inner parts of the hingeless control surface, namely the guide-slide assemblies, were sized. Actuation of the system was modeled and actuation force placement was determined. Support webs which are used to shorten the length of unsupported panels were modeled and their placement and the effects of their slanting angle were analyzed. The camber morphing concept was tested with aerodynamic analyses. Aerodynamic analyses were done using the section contours of the morphed sections of structural analyses. Aerodynamic coefficients were calculated for different models of various morphed geometries. It was determined that the aerodynamic characteristics of the hingeless control surface depend on the trailing edge deflection rather than the actual shape of the morphed section.

The second part of the thesis focused on the implementation of the camber morphing concept to the hingeless control surface and adaptive camber wing. The hingeless control surface was structurally analyzed for different configurations. Then the manufactured hingeless control surface prototype model was introduced and how its camber changes were shown. The model was tested with constant loading at each guide-slide assembly to create a constant spanwise camber distribution and with different loading at guide-slide assemblies to create a twisting motion. The experience gathered from the manufactured model was incorporated into finite element models. Adaptive camber wing was analyzed structurally for different control surface actions. It was shown that the hingeless control surfaces can morph independent of each other and the torque-box. Dynamic analyses of the wing was done with finite element method and compared with the experimental analyses of the wing.

Hingeless control surface concept introduced in the thesis was analyzed for both structural and aerodynamic aspects and it was shown that for different configurations, hingeless control surfaces can be used to create the adaptive camber wing.

## **5.2 Recommendations for Future Work**

Coupled analyses of the concept were only done for the representative section. The wing can be analyzed with coupled structural and aerodynamic analyses. This requires the use of 3-D aerodynamics to model the finite span of the wing. Thus more complicated aerodynamic modeling is required.

Static aeroelastic analysis can be employed to see the effect of aerodynamics on the magnitude of actuation forces. Also dynamic aeroelastic analysis can be performed to get the effects of hingeless control surfaces on the flutter speed of the wing.

Manufactured hingeless control surfaces do not have support webs. This condition does not affect the integrity of the structure in structural analyses, but the absence of support webs may cause issues in flight conditions. Models can be updated after a flight test if needed.

## REFERENCES

1. Ünlüsoy, L., Structural Design and Analysis of a Mission Adaptive, Unmanned Aerial Vehicle Wing, M.S. Thesis, Middle East Technical University, February 2010.
2. İnsuyu, E. T., Aero-Structural Design and Analysis of an Unmanned Aerial Vehicle and its Mission Adaptive Wing, M.S. Thesis, Middle East Technical University, February 2010.
3. Stanewsky, E., Aerodynamic Benefits of Adaptive Wing Technology, *Aerospace Science and Technology*, 4, 439–452, 2000.
4. Monner, H. S., Realization of an Optimized Wing Camber by Using Formvariable Flap Structures, *Aerospace Science and Technology*, 5, 445–455, 2001.
5. Gilbert, W. W., ‘Mission adaptive wing system for tactical aircraft’, *Journal of Aircraft* (18), 597–602, 1981.
6. Pendleton, E., Lee, M. and Wasserman. L., ‘Application of active flexible wing technology to the agile falcon’, *Journal of Aircraft* (29), 444–57, 1992.
7. Perry, B. III, Cole, S. R. and Miller, G. D., ‘Summary of an active flexible wing program’, *Journal of Aircraft* (32), 10–31, 1995.
8. Pendelton, E., Bessette, D., Field, P. B., Miller, G. D., Griffin K. E., ‘The Active Aeroelastic Wing (AAW) Flight Research Program,’ AIAA Paper 98-1972, Proc. AIAA/ASME/ASCE/AHS/ASC 39<sup>th</sup> SDM Conf., Long Beach, CA, April 20-23, 1998.
9. Wilson, J.R., ‘Active Aeroelastic Wing: A New/Old Twist on Flight’, *Aerospace America*, 40(9), 34–37, 2002.
10. Sanders, B., Eastep, F.E. and Foster, E., ‘Aerodynamic and Aeroelastic Characteristics of Wings with Conformal Control Surfaces for Morphing Aircraft’, *Journal of Aircraft*, 40(1), 94–99, 2003.

11. Gern, F.H., Inman, D.J. and Kapania, R.K., 'Structural and Aeroelastic Modeling of General Planform Wings with Morphing Airfoils', *AIAA Journal*, 40(4), 628–637, 2002.
12. Andersen, G. R., Cowan, D. L., Piatak, D. J., 'Aeroelastic Modeling, Analysis and Testing of a Morphing Wing Structure', 48th AIAA/ASME/ASCE/AHS/ASC Structures, Structural Dynamics, and Materials Conference, 1734, 2007.
13. Bowman, J., Sanders, B., Cannon, B., Kudva, J., Joshi, S., Weisshaar, T., Development of Next Generation Morphing Aircraft Structures, 48th AIAA/ASME/ASCE/AHS/ASC Structures, Structural Dynamics, and Materials Conference, 2007.
14. Bye, D.R., McClure, P.D., Design of a Morphing Vehicle, 48th AIAA/ASME/ASCE/AHS/ASC Structures, Structural Dynamics, and Materials Conference, 2007.
15. Inoyama, D., Sanders, B. P., Joo, J.J., Computational Design of Morphing Wing Structures through Multiple-Stage Optimization Process, 48th AIAA/ASME/ASCE/AHS/ASC Structures, Structural Dynamics, and Materials Conference, 2007.
16. Cesnik, C., Last, H. R., Martin, C. A., A Framework for Morphing Capability Assessment, 45th AIAA/ASME/ASCE/AHS/ASC Structures, Structural Dynamics and Materials Conference, 2004.
17. McGowan, A. R., Vicroy, D. D., Busan, R. C., Hahn, A. S., Perspectives on Highly Adaptive or Morphing Aircraft, NATO-RTO Applied Vehicle Technology Panel (AVT) Symposium, 2009.
18. Cavagna, L., Ricci, S., Riccobene, L., Application of Adaptive Camber Mechanism to Morphing Wings, NATO-RTO Applied Vehicle Technology Panel (AVT) Symposium, 2009.
19. Stanewsky, E., Adaptive Wing and Flow Control Technology, *Progress in Aerospace Sciences*, 37, 583–667, 2001.
20. Monner, H. S., Realization of an Optimized Wing Camber by Using Formvariable Flap Structures, *Aerospace Science and Technology*, 5, 445–455, 2001.
21. Ricci, S., Scotti, A., Terraneo, M., Design, Manufacturing and Preliminary Test Results of an Adaptive Wing Camber Model, 47th

- AIAA/ASME/ASCE/AHS/ASC Structures, Structural Dynamics and Materials Conference, 2006.
22. Masarati, M., Quaranta, G., Ricci, S. and Scotti, A., Aeroservoelastic Analysis of Morphing Controlled Surfaces, International Forum on Aeroelasticity and Structural Dynamics, 2007.
  23. Phillips, W. F., Lifting-Line Analysis for Twisted Wings and washout-Optimized Wings, *Journal of Aircraft*, 41(1), 128-136, 2004.
  24. Phillips, W. F., Minimizing Induced Drag with Wing Twist, Computational-Fluid-Dynamics Validation, *Journal of Aircraft*, 43(2), 437-444, 2006.
  25. Campanile, L.F. and Anders, S., Aerodynamic and Aeroelastic Amplification in Adaptive Belt-rib Airfoils, *Aerospace Science and Technology*, 9(1), 55–63, 2005.
  26. Seber, G., Sakarya, E., Insuyu, T. E., Sahin, M., Özgen, S., Yaman, Y., Evaluation of a Camber Morphing Concept Based on Controlled Flexibility, International Forum on Aeroelasticity and Structural Dynamics, 2009.
  27. Hetrick, J. A., Osborn, R. F., Kota, S., Flick, P. M., Paul, D. B., Flight Testing of Mission Adaptive Compliant Wing, 48th AIAA/ASME/ASCE/AHS/ASC Structures, Structural Dynamics, and Materials Conference, 2007.
  28. Vos, R., De Breuker, R., Morphing Wing Flight Control Via Postbuckled Precompressed Piezoelectric Actuators, *Journal of Aircraft*, 44(4), 1060-1068, 2007.
  29. Diaconu, C. G., Weaver, P. M., and Mattioni, Concepts for Morphing Airfoil Sections Using Bi-stable Laminated Composite Structures, *Thin-Walled Structures*, 46, 689–701, 2008.
  30. Kheong, B. L. W., Jacob, J., In Flight Aspect Ratio Morphing Using Inflatable Wings, 46th AIAA Aerospace Sciences Meeting and Exhibit, Reno, Nevada, AIAA Paper 2008-425, 2008.
  31. Vos, R., Gurdal, Z., Abdalla, M., A Novel Mechanism for Active Wing Warping, 49th AIAA/ASME/ASCE/AHS/ASC Structures, Structural Dynamics, and Materials Conference, Schaumburg, IL, AIAA Paper 2008-1879, 2008.

32. Abbott, I. H., Von Doenhoff, A.E., Theory of Wing Sections, Dover Publications, 1959.
33. Abbott, I. H., Von Doenhoff, A. E., Stivers, L. Jr, Summary of Airfoil Data, NACA Report No: 824, 1945.
34. MD NASTRAN Implicit Nonlinear (SOL 600) User's Guide, MSC Corporation, 2006.
35. MD NASTRAN Quick Reference Guide, MSC Corporation, 2006.
36. Aluminum 2024-T3 Material Data Sheet, last visited on March 2008.
37. 7781 E-Glass Fabric with Araldite LY5052 Resin Material Data Sheet, last visited on March 2008.
38. Bhaskaran, R., Fluent Tutorials: Flow over an Airfoil, Cornell University, <http://courses.cit.cornell.edu/fluent/airfoil/index.htm>, last visited on March 2008.
39. Fluent Inc. 'Tutorials: Modeling Compressible Flow over an Airfoil', 2007.
40. Dayley, B., Python Phrasebook: Essential Code and Commands, Sams Pub., 2007.
41. Spalart, P. R., Allmaras, S. R., 'A One-Equation Turbulence Model for Aerodynamic Flows', AIAA Paper 92-0439, 1992.
42. Anderson, J. D. Jr., Fundamentals of Aerodynamics, Mc-Graw-Hill Higher Education, 2001.
43. Patran PCL Reference Manual, MSC Corporation, 2006.